TU/e EINDHOVEN UNIVERSITY OF TECHNOLOGY

Accuracy evaluation of absolute calibration in thick-target PIXE

Citation for published version (APA):
Munnik, F. (1994). *Accuracy evaluation of absolute calibration in thick-target PIXE*. [Phd Thesis 1 (Research TU/e / Graduation TU/e), Applied Physics and Science Education]. Technische Universiteit Eindhoven. https://doi.org/10.6100/IR419251

DOI:
10.6100/IR419251

Document status and date:
Published: 01/01/1994

Document Version:
Publisher's PDF, also known as Version of Record (includes final page, issue and volume numbers)

Please check the document version of this publication:

• A submitted manuscript is the version of the article upon submission and before peer-review. There can be important differences between the submitted version and the official published version of record. People interested in the research are advised to contact the author for the final version of the publication, or visit the DOI to the publisher's website.
• The final author version and the galley proof are versions of the publication after peer review.
• The final published version features the final layout of the paper including the volume, issue and page numbers.

Link to publication

General rights
Copyright and moral rights for the publications made accessible in the public portal are retained by the authors and/or other copyright owners and it is a condition of accessing publications that users recognise and abide by the legal requirements associated with these rights.

• Users may download and print one copy of any publication from the public portal for the purpose of private study or research.
• You may not further distribute the material or use it for any profit-making activity or commercial gain
• You may freely distribute the URL identifying the publication in the public portal.

If the publication is distributed under the terms of Article 25fa of the Dutch Copyright Act, indicated by the "Taverne" license above, please follow below link for the End User Agreement:

www.tue.nl/taverne

Take down policy
If you believe that this document breaches copyright please contact us at:

openaccess@tue.nl

providing details and we will investigate your claim.

Download date: 04. Oct. 2023

Accuracy Evaluation of Absolute Calibration in Thick-Target PIXE

F. Munnik

Accuracy Evaluation of
Absolute Calibration in Thick-Target PIXE

Accuracy Evaluation of Absolute Calibration in Thick-Target PIXE

PROEFSCHRIFT

ter verkrijging van de graad van doctor
aan de Technische Universiteit Eindhoven,
op gezag van de Rector Magnificus, prof.dr. J.H. van Lint,
voor een commissie aangewezen door het College van
Dekanen in het openbaar te verdedigen op
dinsdag 28 juni om 16.00 uur

door

FRANS MUNNIK

Geboren te Groningen

Dit proefschrift is goedgekeurd
door de promotoren
prof.dr. M.J.A. de Voigt
en
prof.dr.ir. J.J.M. de Goeij

Contents

1 Introduction **3**

2 Theory **11**

2.1 Thick Target Yield 11

2.1.1 Derivation of the general Thick Target PIXE formula . . . 11

2.1.2 Applications of the general PIXE formula 19

2.2 Secondary Fluorescence Yield 22

2.3 The Data Base 30

2.3.1 Introduction 30

2.3.2 Stopping Power 31

2.3.3 Ionization Cross Section 33

2.3.4 Branching ratio 35

2.3.5 Fluorescence Yield 36

2.3.6 X-ray Attenuation Coefficient 36

2.3.7 Scattering Cross Section 38

3 Error propagation of the uncertainty in various quantities to the uncertainty in the primary PIXE yield and Secondary Fluorescence yield. **40**

3.1 Introduction 40

3.2 Uncertainty Calculation 41

3.3 The Uncertainty in the Primary Yield 42

3.3.1 Introduction 42

3.3.2 Propagation Factor for the Cross Section 43

3.3.3 Propagation Factor for the Stopping Power and the X-ray Attenuation Coefficient 44

3.3.4 Propagation Factor for the Matrix Composition 46

3.3.5 Influence of the Ionization Depth on the Propagation Factor 49

3.3.6 Propagation Factor for the Proton Beam Energy 50

3.3.7 Conclusion 51

3.4 The Uncertainty in the Secondary Fluorescence Yield 52

3.4.1 Introduction 52

3.4.2 Energy Dependence of the SF Yield 54

3.4.3 Depth Dependence of the SF Yield 57

3.4.4 Concentration Dependence of the SF Yield 59

3.4.5 Atomic Number Dependence of the SF Yield 61

3.4.6 Propagation Factor for the Stopping Power and the X-ray Attenuation Coefficient . . . 63
3.4.7 Conclusion . . . 64
3.5 Conclusions . . . 65

4 Experimental Setup **66**
4.1 General description . . . 66
4.2 Beam energy calibration . . . 69
4.2.1 Introduction . . . 69
4.2.2 Measurements using elastic and inelastic scattering of protons 69
4.2.3 Measurements using (p,α) reactions . . . 73
4.2.4 Discussion and conclusions . . . 74
4.3 Measurement of the number of bombarding particles . . . 75
4.4 The Beam-On-Demand System . . . 78
4.5 The Use and Calibration of Absorbers . . . 80
4.6 Detector Calibration . . . 83
4.7 Data Analysis . . . 87
4.8 Conclusions . . . 91

5 Evaluation of the absolute calibration method in TT-PIXE **94**
5.1 Introduction . . . 94
5.2 Models and uncertainties . . . 94
5.3 Measurements of thin targets . . . 98
5.4 Measurements of thick mono-elemental foils . . . 100
5.5 NIST reference materials . . . 107
5.6 Double metal foils . . . 110
5.7 Biological reference materials . . . 113
5.8 Discussion and general conclusions . . . 122

References **128**

A L-lines **134**

B Calculations for the SF yield **139**

C Derivation of Propagation Factors for the Primary Yield **142**

Table of Symbols **146**

Summary **149**

Samenvatting **151**

Dankwoord **153**

Levensloop **154**

1 Introduction

After a general description of the PIXE technique, a brief comparison with other analytical techniques is presented. Different calibration methods for PIXE are then discussed, with the emphasis on the analysis of thick targets. Finally an outline of this thesis is given.

Introduction to PIXE

Nowadays, there are many analytical techniques based on the use of particle accelerators. One of these techniques is Particle Induced X-ray Emission (PIXE). With this technique, particles from the accelerator (usually protons of a few MeV) are used to ionize atoms of the sample. The created vacancies in the inner electron shells are filled by electrons from the outer shells. During this process, energy is released that is used for the emission of characteristic X-rays, Auger electrons or both. The energy of the X-ray is characteristic for the energy difference between two electron states and this in turn identifies the atom ionized. Each allowed transition results in X-rays with a specific energy; this is called an X-ray line. There are many X-ray lines per element possible and the number of X-ray lines per element increases with increasing atomic number. The emphasis in the analysis is almost exclusively on ionization of the K- and L-shell.

There are two methods to measure the energy of the X-rays. One method uses a wavelength dispersive (WD) system, the other an energy dispersive (ED) system. In a WD system the X-rays emitted from the sample are selected by reflected on a Bragg crystal and then detected with a detector, usually a proportional counter. The angle of the scattering on the Bragg crystal determines the energy of the X-rays. This system has a superior energy resolution (2-40 eV) for X-ray energies below 20 keV, but only one X-ray line can be measured at the time. The energy resolution is improved when the X-rays are better collimated. Therefore, the detection efficiency of a WD system is not very high due to limitations in the solid angle. In an ED system the energy of the X-rays is measured directly, usually with a Si(Li) detector. This has the advantage that many X-ray lines can be measured simultaneously. The solid angle can also be made large and the detection efficiency is high (except for low energy X-rays, see Section 4.6). The energy resolution is not so good as for a WD system (about 160 eV for the Fe Kα line). However, the advantages outweigh the disadvantages and the ED system is widely used in PIXE.

From the measured X-ray intensities the amounts or concentrations of the elements in the sample under investigation can be determined. The analysis of thick targets is complicated by the occurrence of two so-called thick target effects:

(1) The particles are slowed down in the sample because of the Coulomb interaction with, mainly, the electrons of the atoms in the sample. The ionization cross section becomes a function of depth in the sample because it is a function of particle energy, which decreases with increasing depth. (2) The X-rays produced at a certain depth in the sample have a probability of being absorbed in the sample instead of reaching the detector. Both effects are mainly determined by the elements in the sample with the largest concentrations, the so-called matrix elements. For thin targets, the X-ray yield is a simple product of several quantities. For thick targets, this changes into an integration over the depth of the product of the ionization cross-section and the X-ray transmission through the sample. Because of this complication, PIXE on thick targets is often considered as a separate category of PIXE called TT-PIXE (thick-target PIXE). Calibration methods to obtain quantitative results are described below.

An advantage of PIXE is the high sensitivity, which means a high X-ray yield for a given amount of material and a given number of bombarding particles. This can be translated into short measuring times (2-10 min.), in (relatively) low detection limits (0.1-1 ppm [Joh 92]), or in a very small amount of material needed for the analysis (0.01-1 mg). Other advantages are that little sample preparation is needed and that for many applications PIXE is a nondestructive analysis technique, enabling the analysis of such diverse samples as aerosols and valuable paintings in situ. In combination with a microbeam, a particle beam focussed to a spot of a few μm diameter, PIXE becomes a really powerful analytical technique, making it possible to obtain two-dimensional concentration maps of the sample. The current state-of-the-art microbeam is a microbeam with a diameter of 0.3 μm FWHM and a beam current of 100 pA [Gri 93]. In micro-PIXE amounts as low as 10^{-15}g or 10^7 atoms of an element can still be detected in in-situ samples which makes this an unique analytical technique. The fundamentals of PIXE and its application to many fields of interest are covered extensively in a book by Johansson and Campbell [Cam 88].

Comparison of PIXE with other analytical techniques

As described above, PIXE can be classified as an accelerator based technique. It can also be classified as an X-ray detection technique. Other analytical techniques in this category are Electron Probe Micro Analysis (EPMA) and X-ray Fluorescence spectroscopy (XRF). These methods are all based on the same detection principles, only the ionization mechanism is different. In EPMA, the sample atoms are ionized by electrons. This has the advantage that the production of an electron beam is widespread as it is used in electron microscopes and this makes it a much cheaper and more readily available technique than PIXE. Furthermore, the electron beam can be focussed to a spot of a diameter of about 50 Å. A disadvantage of EPMA is a high background in the spectrum caused by a high level of primary electron Bremsstrahlung, resulting in high detection limits. Furthermore, the range of

electrons is very short making EPMA only suitable for very thin samples (of a few hundred nm). The beam dimensions also quickly increase with increasing sample depth due to scattering of the electrons. The main detection-system in EPMA is the ED system.

In XRF the ionization is caused by a beam of X-rays. The simplest way to produce an X-ray beam is to use a radionuclide emitting X-rays or low-energy gamma-rays. This is also very cheap but the intensity of a source is not very high, resulting in high detection limits. Another X-ray source is an X-ray tube. With an X-ray tube much higher intensities can be obtained and it can be used in several configurations. In one configuration, the exciting X-rays have many different energies, resulting in a good sensitivity for many elements. This so-called broadband excitation is obtained by using the X-rays produced in the tube directly. Disadvantages of this method are a high background and an increased complexity of the theoretical calculations of the X-ray intensities emitted from the sample.

This can be remedied by using a mono-chromatic X-ray source. The X-ray spectrum of the tube can be modified in this way by placing a filter between the X-ray tube and the sample. Another method to obtain mono-chromatic X-rays is the method of secondary fluorescence. The X-rays of the tube are impinged on a mono-elemental sample. The resulting characteristic X-rays are used to excite the sample. Note, that also a proton beam can be used to produce a mono-chromatic X-ray source in this way. A disadvantage of this technique is that good sensitivity can only be obtained for a few elements. The reason for this is that the cross section of the ionization by X-rays decreases rapidly with increasing difference between the ionization energy and the X-ray energy. Generally, the detection limits for XRF are about the same or slightly worse than the detection limits for PIXE. Both PIXE and XRF can be used for in-situ measurements but the radiation damage caused by XRF is much less than that caused by PIXE. However, XRF is much less suited for obtaining two-dimensional concentration maps because an X-ray beam is much more difficult to focus than a proton beam. There has been progress in this field making it possible to produce X-ray beams with a diameter of about 10 μm [Rin 93].

A state-of-the-art application of XRF is total reflection XRF (TRXRF). With this technique the angle between the X-ray beam and the sample surface is only a few mrad so that the X-ray beam is almost completely reflected. This improves the detection limits because the background from scattered X-rays is reduced. The technique is most useful for solutions, but it imposes strict demands on the surface quality substrate on which the solution is deposited. With a synchrotron ring, very high intensities of the primary X-rays can be achieved. This is very useful for the X-ray microbeams but it can also be used for TRXRF and other applications. A disadvantage of the synchrotron ring is the cost of using such a source. Most XRF systems use the WD detection system. A more detailed comparison of PIXE and XRF is given in [Wil 88].

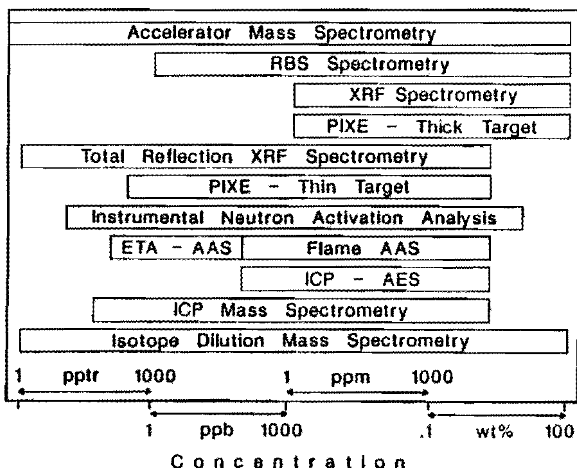

Fig. 1.1: Comparison of the detection range of several analytical techniques. The techniques in this comparison are: AMS = accelerator mass spectrometry, RBS = Rutherford backscattering spectroscopy, XRF = X-ray fluorescence, PIXE = particle induced X-ray emission, TRXRF = total reflection X-ray fluorescence, INAA = instrumental neutron activation analysis, ETA = electrothermal atomizer, AAS = atomic absorption spectrometry, ICP = inductively coupled plasma, AES = Auger electron spectrometry, IDMS = isotope dilution mass spectrometry. Reproduced from Ref [Mai 90] by permission of North-Holland Physics Publishing.

Next to the two categories of analytical techniques already described (accelerator based techniques and X-ray detection techniques), there are also many other analytical techniques. A comparison of the detection ranges of a number of techniques is given in Fig. 1.1. This comparison is expressed in concentrations. Detection limits in mass, however, are much more favourable for PIXE because PIXE requires only very little amounts of material, especially micro-PIXE. This comparison is of course only very global. The detection limit can vary from element to element and for the same element it can vary from sample to sample. For single elements, the measurement conditions can be further optimized and e.g. preconcentration techniques can be used to decrease the detection limit. Another question along with this comparison is the accuracy and precision of the analytical techniques. Generally, IDMS and NAA are considered the most accurate techniques. The question of the accuracy of PIXE is also the question to be further investigated in this thesis.

The detection limits are not the only important aspect of an analysis. It often is also important to obtain information about the 2D-spatial distribution of the elements in the sample. This makes demands not only on the abilities of the analytical technique, but also on the preparation of the sample, because the

structure of the sample should remain intact. Micro-PIXE is particularly suited for this type of measurement. The proton microbeam can also be used in combination with other ion beam techniques such RBS. Only a few other techniques have comparable abilities. One of them is EPMA, which has smaller spot sizes but higher detection limits. A comparison of several microprobes is given in [Bir 89, Chapter 10]. Of these microprobe techniques, micro-PIXE (or micro-RBS) has the best prospects for quantitative results.

Quantitative analysis using TT-PIXE

To answer the question on the accuracy of PIXE, first the calibration methods for obtaining quantitative results have to be studied. There is a range of calibration methods for quantitative analysis using PIXE [Joh 88, chapters 4&6]. In general, obtaining quantitative results is much easier for thin targets because the thick target effects can be neglected.

At one end of the range is the use of external standards. This method is especially useful for thin targets because no information about the matrix composition is needed. Both target and standards have to be thin and the standards have to contain the elements of interest. Straightforward comparison of the normalized X-ray yields for the same element directly gives the the mass thickness of the element of interest. Combined with the target thickness, this gives the concentration in the target. For thick targets there are however some complications. First, the matrix composition has to match closely the matrix composition of the sample of interest. If this is not true, the thick-target effects have different influences. Secondly, it is very difficult to correct for secondary processes when using standards. Ideally, it would require a set of standards with different matrix compositions and concentrations for the elements of interest. Then an interpolation in a multidimensional graph would be needed to obtain the correct value of the concentration of the elements of interest in the sample. This method of using external standards relies on precise charge measurement for the comparison of the X-ray yields of standard and target. The method depends completely on the standard, its availability and the accuracy with which the concentrations of the elements in the standard are known. These conditions are more difficult to fulfill for thick targets then for thin targets.

At the other end of the range of calibration methods is the absolute calibration procedure (or absolute calculation). This method uses no standards but it uses a physical model of the PIXE process. The concentration is then calculated from the measured X-ray yield using equations derived from the model. For the calculation, values of all quantities in the equations are necessary. These quantities include both physical quantities, such as the ionization cross-section and experimental quantities, such as the detector efficiency. Once a set of values is collected, this is a very flexible method since there are no restrictions on sample composition and thickness. A disadvantage is that for thick targets, the concentrations of all matrix

elements are also needed for the calculation. Some of the work on this subject is reported in [Cla 81, Cam 83, Smi 84, Coh 87].

At an intermediate position of the range is the use of an internal standard, for both thin and thick samples. This is a combination of the use of standards and absolute calculations. The internal standard is a well-known amount of an element added to the sample. Of course, the element should be present in the sample only in negligible concentrations and it cannot be determined due to the addition of the internal standard. The concentration is then calculated relative to the concentration of the internal standard. Using this method beam charge and detector solid angle are not needed for the calculation of the X-ray yield but knowledge of production cross-section, detector efficiency and (for thick samples) self absorption of X-rays in the sample is necessary. The values for the sample of the above quantities are only needed relative to the values for the internal standard, thus reducing the influence of errors. The addition of the internal standard has to be done so that its distribution in the sample is homogeneous. However, it is not always possible to put extra material uniformly into the sample and it may introduce additional impurities in the sample.

There are several other intermediate methods relying on combinations of the above described methods. For example, thick single-element standards, consisting of the element of interest, can be used in combination with thick samples. This is a combination of the use of external standards and absolute calculations. The values for the quantities in the equations still have to be used but only in a relative way since the outcome of the calculation for the sample is divided by the results of the calculation for the standard. Experimental quantities such as detector efficiency and detector solid angle are no longer needed.

In view of its flexibility and versatility the absolute calibration procedure is an attractive method. This method can be assisted by the measurement of thin standards for checking the reproducibility of the experimental setup. The absolute calibration method is particularly suited for micro-PIXE because it often deals with inhomogeneous targets and very little amounts of material. This makes it very difficult to obtain and use external standards.

As stated above, the matrix composition has to be known when using the absolute calibration method for thick targets. However, PIXE is not very suitable for the detection of (matrix) elements with $Z \leq 10$. This has two reasons. First, there is the fundamental reason that the fraction of vacancies in the K-shell filled under emission of X-rays, the so-called fluorescence yield, becomes very small. Secondly, there is a more practical reason that the low-energy X-rays (< 1 keV) emitted by these elements are difficult to detect with suitable efficiency. Nowadays, it is possible to detect elements down to nitrogen but this is with low efficiency [Wil 91]. To obtain information about the light elements, other analytical techniques have to be used. We have chosen to use Nuclear Backscattering Spectroscopy (NBS) for this purpose. The advantage of this technique is that it can often be done

simultaneously with PIXE. Like PIXE, NBS is also an accelerator based technique but in this case the particles scattered on the sample nuclei are detected. In the classical situation, the collision can be described by solid bodies and the scattering cross-section can be calculated using classical mechanics. This process is called Rutherford Backscattering Spectroscopy (RBS). When the energy of the bombarding particles increases, nuclear thresholds can be exceeded and resonances in the scattering cross section can occur, resulting in the so-called non-Rutherford scattering cross sections. We have therefore used the term NBS instead of RBS. The energy loss caused by the collision depends on the scattering angle and the nuclei involved in the collision. By measuring the energy of the scattered particles at a fixed angle, the atomic mass of the target atoms can be determined. Energy loss is also caused by the interactions of the particles with the sample electrons. This makes the measured energy of the scattered particles a function both of the scattering depth and of the atomic mass of the target atom. This duality can be useful in some cases in that it allows the determination of the thickness of the sample. In other cases, it can obstruct the detection of light elements in the presence of heavier elements. This technique is especially suited for light elements because the mass resolution is best for light elements. However, the sensitivity of NBS is not so high as that of PIXE. RBS (or NBS) is an analytical technique in its own right that is widely used for many applications. In our case, however, we only use it as a supplemental technique for the determination of the light matrix elements ($Z < 10$) and for the determination of the sample thickness, if needed.

Outline of this thesis

Because of the strict conditions placed on standards for thick targets, the absolute calibration is especially attractive for TT-PIXE and this was the main reason for starting the present studies. The aim of the study is the evaluation of the achievable accuracy and of the underlying sources of inaccuracy for the absolute calibration method, especially for thick targets. To accomplish this aim, several subjects have to be treated.

The first subject is the theoretical description. In Chapter 2, the equations are derived that are necessary for the calculation of the elemental concentrations in thick targets from the X-ray yield. In contrast to literature, these equations are derived starting from an infinitesimal volume element with no a-priori conditions on the target. This approach is indispensible for micro-PIXE on targets with a non-uniform matrix composition. From this starting point, a general formula can be derived that can easily be adapted to different types of target, target orientations, etc. Formulas for thin and intermediate-thick targets as well as homogeneous targets are then derived from the general formula. X-rays absorbed in the sample can also ionize sample atoms that in turn can emit new (secondary) X-rays. This is the main secondary effect and it is called Secondary Fluorescence (SF). The equations needed to calculate this effect are also derived in Chapter 2. Special

attention is given to the physical interpretation of these equations. As for the Thick-Targets (TT) calculations, the values of all quantities have to be known for the absolute calibration. For the accuracy evaluation, the uncertainties in these values for both TT and SF calculations have also to be known. The quantities can be divided in two groups: experimental quantities and theoretical quantities. Experimental quantities are variables determined by the experimental setup and they can be changed according to need; examples are the particle beam energy and the detector solid angle. Theoretical quantities are fundamental variables determined by physical properties; examples are the ionization cross section and the stopping power. The current knowledge about the physical quantities and their accuracy is analyzed in the third section of Chapter 2.

The next chapter (Chapter 3) presents the total uncertainty in the X-ray yield or the calculated concentration derived from uncertainties in all the quantities in the TT-PIXE and SF formulas. Sofar, such a systematic treatment for PIXE has not been presented in literature. A new quantity, the error propagation factor is introduced to quantify the influence of the uncertainty in one quantity on the uncertainty in the X-ray yield or the calculated concentration. In Chapter 3, the error propagation factors for the non-trivial cases are calculated. Examples are given for various sample compositions to obtain insight in the physical processes involved. This is done for both the TT and the SF calculations.

In the next chapter (Chapter 4), the experimental setup is discussed. The PIXE setup has been renovated to allow the measurement of thick targets. For this purpose, several new systems have been added, which are described in Chapter 4. It should be noted that the aim of the renovation has not been to improve the detection limits. The main subject of Chapter 4 is the determination of the experimental quantities as well as the uncertainties in these quantities. The execution of the complete analysis is described in this chapter as well as the software needed for this analysis.

In Chapter 5, the absolute calibration method is evaluated. Part of the evaluation is done by a discussion of the models and the underlying conditions and assumptions. Another part is done by performing some experiments. Several types of reference materials are analyzed to obtain a general impression of the validity of the absolute calibration method. These materials include targets in which no SF can occur and targets in which SF plays a relatively strong role. Finally, Section 5.8 discusses the results of the comparison of the theoretical description and experimental data, the contribution to the total uncertainty of various error sources, as well as an outlook on prospects for the absolute calibration method.

2 Theory

The theoretical description for the primary PIXE yield is presented. A new aspect is that this treatment starts from first principles and that the conditions and assumptions are clearly stated. This allows greater flexibility in that the equations for different applications can all be derived from one central formula. Next, the theoretical description for the secondary fluorescence yield is presented. A new aspect is that the theory is presented in such a way that the physical interpretation of the formulas is transparant. Finally, a data base is presented for calculations based on this theory.

2.1 Thick Target Yield

In this section, the formula for the PIXE yield of a thick target is derived from the yield of a small volume $dAdx$ of the sample. In the first subsection, the derivation is as general as possible even allowing for inhomogeneous targets. In the next subsection, some applications under extra conditions are given and only here is the condition of homogeneity first introduced. Particular attention is paid to the conditions and assumptions under which the formulas are valid. A distinction is made between conditions and assumptions: A condition has to be satisfied before using the formula, whereas an assumption states that a condition is satisfied without hard proof or that a real effect can be neglected. However, no distinction between the two is made for the numbering. The reader can skip the first subsection if only interested in formulas that are directly applicable.

2.1.1 Derivation of the general Thick Target PIXE formula

First, let us consider a volume $dAdx$ of a sample under nuclear particle bombardment. The orientation of this volume is chosen in such a way that the depth x is in the same direction as the particle movement (see Fig. 2.1). The subdivision of the volume in an area dA and a depth dx is made because different effects occur for both variables. The most widely used particles are protons, but deuterons, α-particles and heavier particles can be used as well. The atoms in this volume can emit characteristic X-rays under particle bombardment, often several lines for one element Z. The number of X-rays of one line of an element Z, produced under particle bombardment, is called the yield Y_0 and is given by the following formula:

$$Y_0(X_Z, A, x) = n_P(A, x)dA\, n_Z(A, x)dAdx \frac{\sigma_{Z,X}^{prod}(E_P(x))}{dA} \tag{2.1}$$

with

X_Z	X-ray line of element Z, e. g. $K_{\alpha 1}$ or $L_{\beta 3}$,
$n_P(A,x)$	number of bombarding particles per unit area (cm^{-2}),
$n_Z(A,x)$	number of atoms of element Z per unit volume (cm^{-3}),
$\sigma^{prod}_{Z,X}(E_P(x))$	cross section for the production of an X-ray (cm^2), it is a function of the energy E_P of the bombarding particle, which is in itself a function of the depth x (to be explained later).

The particle beam is called inhomogeneous, if n_P is a function of area A. The dependence of the number of projectiles on x is a physical process, since part of the projectiles is scattered when going through the sample.

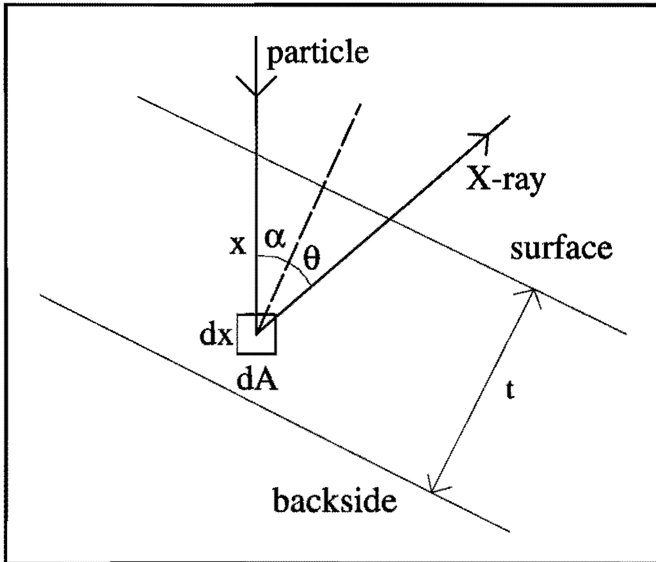

Fig. 2.1: Schematic drawing of the production of X-rays in the volume $dx\ dA$ of the sample with thickness t.

From n_Z, the concentration of element Z in the volume at position (A,x) can be extracted,

$$n_Z(A,x) = \frac{N_{Av}}{M_Z}\rho_S(A,x)c_Z(A,x) \tag{2.2}$$

with

N_{Av}	Avogadro constant (mol^{-1}),
M_Z	atomic mass of element Z (g/mol),
$\rho_S(A,x)$	total density of the sample (g/cm^3),
$c_Z(A,x)$	mass fraction of element Z in the volume $dAdx$ (g/g).

The production cross section consists of a number of terms, for the K-shell it is

$$\sigma^{prod}_{Z,X(K)}(E_P) = \sigma^{ion}_{Z,K}(E_P)\omega_{Z,K}b_{Z,X(K)} \tag{2.3}$$

with

$\sigma^{ion}_{Z,K}(E_P)$ cross section for ionization of the K-shell of element Z, it is dependent on the projectile energy E_P (cm^2),

$\omega_{Z,K}$ fluorescence yield for the K-shell, this is the probability of a vacancy being filled by an electron from a higher shell under emission of an X-ray,

$b_{Z,X(K)}$ branching ratio, which is the fraction of the total K-shell X-rays in the line $X_Z(K)$ (e.g. $K_{\alpha 2}$ or $K_{\beta 1}$). Each line X_Z stands for a transition of an electron from a sub-shell to the K-shell under emission of an X-ray.

The quantities $\sigma^{ion}_{Z,K}(E_P)$, $\omega_{Z,K}$ and $b_{Z,X(K)}$ are needed for for the calculation of the concentration from the measured yield. Their values can be taken from literature. A discussion on the available data is given in Section 2.3. Equations for the production cross-section for L-shells can be found in Appendix A.

As mentioned previously, the cross section is dependent upon the projectile energy. Unfortunately, this energy is in its turn dependent upon the depth x in the sample, because the projectile (an ion) loses energy through Coulomb interaction with the surrounding atoms (nuclei and electrons). This is one of the two so called thick target effects, the other is discussed below. The measure for the energy loss of the ion is called the stopping power and it is defined as

$$S_t(E_P(x), A) = \frac{1}{\rho_S(A, x)} \frac{dE_P(x)}{dx} \tag{2.4}$$

with $dE_P(x)/dx$ the energy loss of the projectiles along their path in the sample. The dimension of S_t is (keV cm^2 /g). It is because of this equation that the orientation of the volume element is chosen (see Fig. 2.1). The relation between depth x in the sample and particle energy E_P now is as follows

$$x = \int_{E_{P,0}}^{E_P} \frac{1}{\rho_S(A, E'_P) S_t(E'_P, A)} dE'_P \tag{2.5}$$

with $E_{P,0}$ the initial particle beam energy. The depth in the sample perpendicular to the sample surface is found by multiplying x with $\cos\alpha$. This relation implies that there is an unambiguous relationship between the depth x and the particle energy E_P. There are a number of objections against the unambiguity of this relationship. The main objection is the energy straggling. Energy straggling is caused by the fact that the energy loss is a statistical process. Even if the projectiles entering the sample all have the same energy, the ions have a semi-Gaussian energy distribution at depth x. This is a fundamental problem that cannot be solved.

Assumption 1 *The influence of the energy straggling on the relation between E_P and the depth x in the sample can be ignored.*

The other objections against the unambiguity are experimental problems that can be minimized to satisfy the following conditions:

Condition 2 *The ion beam energy $E_{P,0}$ is mono-energetic.*

In a practical situation, there always is a certain energy spread in an ion beam. However, for thick samples, the energy straggling is much larger than the beam energy spread. Therefore, the error made by not satisfying Condition 2 is for thick samples much smaller than the error caused by energy straggling in the sample.

Condition 3 *The projectiles in the beam move in parallel direction.*

Assumption 4 *The effect of small angle ion scattering or multiple scattering on $\cos\alpha$ can be neglected.*

The cross section for small angle scattering of a few degrees, however, is not negligible. This results in a spread in the angle α. If the ion beam is not parallel, this also results in a spread in α. The influence of the spread in α on $\cos\alpha$ is minimal if α is small [Cam 84]. As long as the processes, threatening the validity of the above conditions, result in a symmetrical distribution around an average value and the standard deviation of this distribution is not very large, the effects of these processes averages out.

Eq. 2.1 describes the total number of X-rays produced in a volume $dAdx$ of the sample. This yield is distributed evenly over all directions. In practice, not all the X-rays are detected because of limitations in the detector solid angle and the detection efficiency and because of absorption of the X-rays in the sample. This last reason is the second thick target effect. Thus, the number of X-rays detected is :

$$Y(X_Z, A, x) = Y_0(X_Z, A, x) T_S(E_{X_Z}, A, x) T_{abs}(E_{X_Z}) \varepsilon(E_{X_Z}) \frac{\Omega}{4\pi} \tag{2.6}$$

with

$$T_S(E_{X_Z}, A, x) = \exp\left\{ -\frac{\mu_t(E_{X_Z}, A, x)}{\rho_S} \frac{\cos\alpha}{\cos\theta} \rho_S(A, x) x \right\} \tag{2.7}$$

and with

E_{X_Z} energy of an X-ray in line X_Z (keV),

$T_S(E_{X_Z}, A, x)$ transmission probability of X-rays with energy E_{X_Z} through the sample from depth x in the direction of the detector.

$T_{abs}(E_{X_Z})$	transmission probability of X-rays with energy E_{X_Z} through an absorber; this probability is dependent on the X-ray energy and is calculated with Eq. 2.7 without the A and x dependence and with $\cos\alpha/\cos\theta = 1$,
$\varepsilon(E_{X_Z})$	detector efficiency, this is the probability, that the energy of an X-ray is completely absorbed in the detector crystal; this is also dependent on the X-ray energy,
$\Omega/4\pi$	relative detector solid angle,
$\mu_t(E_{X_Z}, A)$	total linear X-ray absorption coefficient of the sample (cm^{-1}),
θ	angle between the sample normal and the direction of the detector,
$x\frac{\cos\alpha}{\cos\theta}$	distance travelled by the X-ray through the sample in the direction of the detector (cm).

The absolute detector efficiency ε_{abs} is introduced to shorten the notation:

$$\varepsilon_{abs}(E_{X_Z}) = T_{abs}(E_{X_Z})\varepsilon(E_{X_Z})\frac{\Omega}{4\pi} \tag{2.8}$$

Usually the X-ray absorption coefficient is given in literature as μ/ρ, the mass absorption coefficient, hence this notation in the formula. The X-ray absorption coefficient is composed of a number of terms:

$$\mu(E_{X_Z}) = \tau_{tot}(E_{X_Z}) + \sigma_{coh}(E_{X_Z}) + \sigma_{incoh}(E_{X_Z}) + \pi(E_{X_Z}) \tag{2.9}$$

with

τ_{tot}	photo-electric absorption coefficient, which describes the interaction whereby the energy of an X-ray is completely absorbed u nder ejection of an electron from its shell, thus creating a vacancy. For low energy X-rays (a few keV) it is the dominating factor.
σ_{coh}	coherent absorption coefficient, which describes the coherent or Rayleigh scattering of an X-ray on an atomic electron. During this process their is no energy loss for the X-ray.
σ_{incoh}	incoherent absorption coefficient, which describes the incoherent or Compton scattering of an X-ray on an electron. During this scattering there is an energy loss for the X-ray.
π	pair production absorbtion coefficient. This term can be neglected since it can only occur for γ-rays with an energy above 1.5 MeV.

In theoretical computations, all terms are calculated separately to obtain the total X-ray absorption coefficient.

There are a number of conditions underlying Eq. 2.6 and Eq. 2.7:

Condition 5 *There is no variation in the factor cos θ.*

There is always some variation in θ, especially, because for low detection limits, the solid angle has to be as large as possible. Also, for large beam spots the angle

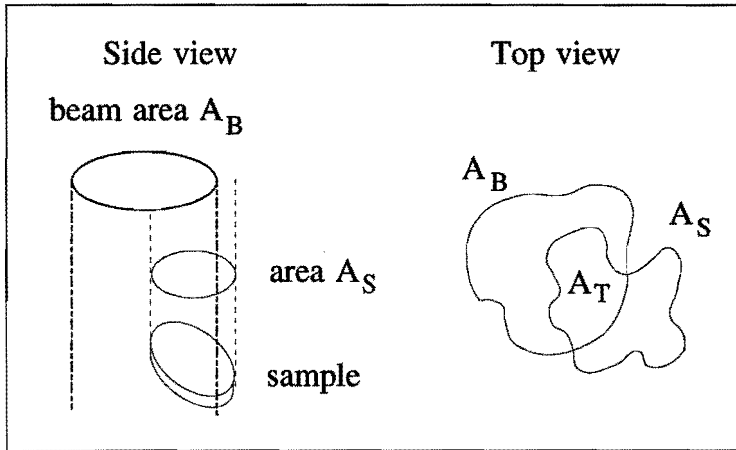

Fig. 2.2: Diagram of the layout of the sample under particle bombardment.

θ varies as a function of the position on the sample. By chosing $\theta = 0°$, the effects of the variation of θ on the variation of cos θ are kept minimal. The use of the total X-ray absorption coefficient is only valid for a narrow beam. For a typical situation in PIXE, the solid angle is so large that the X-rays travelling in the direction of the detector do not form a narrow beam. Therefore, two extra assumptions have to be fulfilled to be allowed to use the total X-ray absorption coefficient:

Assumption 6 *The number of X-rays emitted in the direction of the detector that undergo a small angle coherent scattering and still remain within the detector solid angle Ω can be neglected.*

Assumption 7 *The number of X-rays emitted in a direction out of the detector solid angle that come into the detector solid angle after undergoing a coherent scattering, can be neglected.*

Both effects lead to larger number of X-rays detected than expected on the basis of the theory. After calculation, it was found that the enhancement due to these effects is less than 0.1% for most conditions found in a PIXE setup [Cam 83].

To obtain the total number of detected X-rays, we have to integrate equation 2.6 over the sample volume under ion bombardment. This volume is the area A_T multiplied by the target thickness in the direction of the beam which may be a function of A and is indicated by $t(A)/\cos\alpha$. In general, the area A_T is the intersection of the sample surface A_S perpendicular to the beam with the beam area A_B (see Fig. 2.2). In a practical situation, there are two useful limits: (i) The beam area A_B is larger than the sample surface A_S so that the beam envelops the

sample completely ($A_T = A_S$). (ii) The sample is larger than the beam, $A_S > A_B$ so that $A_T = A_B$.

Condition 8 *All X-rays reaching the detector must leave the sample from one defined surface.*

For X-rays leaving the sample from a side surface, the transmission T_S is too low. When the sample area is larger than the beam area, this assumption always is fulfilled. When the sample area is smaller than the beam area, it only is approximately true when the sample is thin compared to its area under ion bombardment $t/\cos\alpha << A_T$.

The total yield is obtained from eqs. 2.1 and 2.6 by integrating over the sample volume :

$$Y(X_Z) = \varepsilon_{abs}(E_{X_Z}) \int_{A_T} \int_0^{\frac{t(A)}{\cos\alpha}} n_P(A,x) n_Z(A,x) \sigma_{Z,X}^{prod}(E_P(x)) T_S(E_{X_Z}, x, A) dx\, dA \qquad (2.10)$$

Now, it is useful to transform this integral over x to an integral over E_P, using Eq. 2.4, because the cross section $\sigma_{Z,X}^{prod}$ is only known as a function of E_P. One further assumption can be made to simplify the integration :

Assumption 9 *The number of particles scattered in the sample over a large angle can be neglected.*

This means that n_P is independent of x. With Eq. 2.2, it then is possible to derive a complete and most general formula for the thick target PIXE yield:

$$Y(X_Z) = \frac{N_{Av}}{M_Z} \varepsilon_{abs}(E_{X_Z}) \int_{A_T} \left\{ \int_{E_{P,0}}^{E_{P,f}(A)} c_Z(A, E_P) \frac{\sigma_{Z,X}^{prod}(E_P) T_S(E_{X_Z}, E_P, A)}{S_t(E_P, A)} dE_P \right\} n_P(A)\, dA \qquad (2.11)$$

with

$$T_S(E_{X_Z}, E_P, A) = \exp\left\{ -\frac{\cos\alpha}{\cos\theta} \int_{E_{P,0}}^{E_P} \frac{\mu_t(E_{X_Z}, A, E'_P)}{\rho_S} \frac{1}{S_t(E'_P, A)} dE'_P \right\} \qquad (2.12)$$

where $E_{P,f}$ is the particle energy on leaving the sample or zero if the sample is too thick. Note that E_P represents the proton energy in the sample at depth x. This does not mean that quantities that depend x now depend on E_P but only that E_P represents x. $E_{P,f}$ can vary with the place on the sample because of two reasons. The first reason is the inhomogeneity of the sample composition, the second the variation of the sample thickness. To arrive at useful formulas, we introduce the following condition:

Assumption 10 *The influence of thickness variations over the sample on the yield can be neglected.*

In a later chapter (Ch. 3), it is seen that this condition is valid for thick samples even if there are some thickness variations. There are two exceptions when thickness variations are allowed. They are given in the next subsection. Surface roughness, on the other hand, can lead to a decrease in the measured yield of over 10% in certain cases [Cam 85].

In principle, the integral over E_P in Eq. 2.11 can be solved, although only numerically, when $S_t(E_P, A)$, $\sigma^{prod}_{Z,X}(E_P)$, $\mu_t(E_{X_Z})$, $E_{P,0}$ and $E_{P,f}$ are known. The last two quantities have to be determined experimentally, the first three quantities can be obtained from literature. However, there is one problem: the stopping power and the X-ray attenuation coefficient are needed for composite samples while in literature they only are found for individual elements. Therefore, the values of these two quantities have to be composed from the values for individual elements. This can be done using the mass fractions of the elements in the sample.

$$S_t(E_P, A) = \sum_j c_j(A, E_P) S_j(E_P) \tag{2.13}$$

$$\frac{\mu_t(E_{X_Z}, A, E_P)}{\rho_s(A, E_P)} = \sum_j c_j(A, E_P) \frac{\mu_j(E_{X_Z})}{\rho_j} \tag{2.14}$$

with c_j the mass fraction of element j in the sample and $\frac{\mu_j(E_{X_Z})}{\rho_j}$ the mass absorption coefficient of element j. The first formula is first proposed by Bragg and Kleeman [Bra 05] and is now commonly known as Bragg's rule. Both formulas are postulations and, in occasional circumstances, there are deviations from these rules. For instance, there are deviations from Bragg's rule for light elements such as H, C and O (see Section 2.3.2). Nevertheless, we assume that both equations can be used (the assumption is that the condition below is satisfied):

Condition 11 *Eqs. 2.13 and 2.14 are valid for all samples.*

This leaves us with a very important quantity, the sample composition, which must be known beforehand. Unfortunately, the sample composition is often unknown and many times even the subject of the investigation. To calculate the total stopping power and the total X-ray attenuation coefficient, it is not necessary to know the concentration of all elements in the sample, only the major elements must be known. These elements are called the matrix elements. The minimum concentration of a matrix element depends on the accuracy wanted for the calculation.

Assumption 12 *The influence of trace elements with $c_Z < 0.5\%$ on the total stopping power S_t and the total X-ray attenuation coefficient μ_t can be neglected.*

This condition is not always fulfilled. Especially for the X-ray attenuation coefficient, the influence of small concentrations of heavy elements in an otherwise light matrix can be dramatic. For example, in a matrix with 99.5% C and 0.5% Pb, $\mu_t(E_X)$ is more than a factor of two larger than $\mu_C(E_X)$ for $13 < E_X < 21$. How important this effect is for the calculation of the tick-target yield depends on the elements of interest but in general the influence of neglecting elements with small concentrations on the thick-target yield is reduced. For the example above, the thick-target yield increases by a maximum of 5.5% when Pb is also taken as a matrix element. For most cases, the criterium for matrix elements stated in Assumption 12 can be used; in extreme situations, the value of 0.5% has to be decreased. For more information about the influence of the matrix composition on the calculation of the concentration of trace elements, see Subsection 3.3.4. Eqs. 2.11 and 2.12 can be solved iteratively when all matrix elements can be measured with PIXE. This is the case when the X-rays of the element can still be detected with reasonable efficiency, e.g. for elements heavier than neon ($Z > 9$) for a detector with a 8μm Be window. Otherwise, the matrix elements must be measured with some other technique, e.g. NBS (Nuclear Backscattering Spectrometry), or must be known otherwise. A group of samples for which some of the matrix elements cannot be measured with PIXE, is the group of biological samples. For these samples, the matrix constitutes mainly of H, C, N and O.

2.1.2 Applications of the general PIXE formula

So far, there are no limitations made on the A and x dependence of the various quantities. But, in order to be able to separate the integrals over A and x and to solve them, we have to do so now. Formulas for different applications can be arrived at by making different conditions. We make three different conditions.

The first condition

This is the most strict condition and it leads to the most universally used formulas.

Condition 13 *The sample is homogeneous.*

This condition implies that ρ_S and c_Z are independent of A and x. In this case, the matrix elements are no function of A and x. The integrals over x and A can now be separated and the integral over A can be solved: $\int_{A_T} n_P(A)dA = N_P$ with N_P the total number of particles deposited on the sample. N_P is the total number of particles in the beam when the beam area A_B is smaller than the sample area A_S. The resulting formula is the well known thick target PIXE formula derived from eqs. 2.11 and 2.12 :

$$Y(X_Z) = N_P \frac{N_{Av}}{M_Z} c_Z \varepsilon_{abs}(E_{X_Z}) \int_{E_{P,0}}^{E_{P,f}} \frac{\sigma_{Z,X}^{prod}(E_P) T_S(E_{X_Z}, E_P)}{S_t(E_P)} dE_P \qquad (2.15)$$

with

$$T_S(E_{X_Z}, E_P) = \exp\left\{-\frac{\mu_t(E_{X_Z})}{\rho_S}\frac{\cos\alpha}{\cos\theta}\int_{E_{P,0}}^{E_P}\frac{dE'_P}{S_t(E'_P)}\right\} \tag{2.16}$$

In this case, it is not necessary that the particle beam is spatially homogeneous because the sample is already homogeneous.

There are two types of sample for which eqs. 2.15 and 2.16 can be simplified. The distinction is based on a comparison of the sample thickness with the particle range and the transmission probability of the X-rays. The first sample type are targets that are so thin that the particles lose little energy when passing through the sample and the X-rays pass the sample with little loss of intensity. This can be translated in the following conditions:

Assumption 14 *(a)* $\sigma_{Z,X}^{prod}(E_P) \approx \sigma_{Z,X}^{prod}(E_{P,0})$ *and (b)* $T_S(E_{X_Z}, E_P) \approx 1$.

Using Eq. 2.5, we can write Eq. 2.15 as:

$$Y(X_Z) = N_P\frac{N_{Av}}{M_Z}c_Z\rho_S t\,\sigma_{Z,X}^{prod}(E_{P,0})\varepsilon_{abs}(E_{X_Z}). \tag{2.17}$$

This equation is the, also well known, formula for thin targets.

Secondly, we can distinguish the intermediate thick targets. In this case, it is possible to make some corrections for the thick target effects without having to solve the integral numerically [Alo 86]. The condition for this approach is:

Assumption 15 *It is possible to approximate the cross section at every depth in the sample by an average value.*

This average cross section can be given by

$$\overline{\sigma_{Z,X}^{prod}} = (\sigma_{Z,X}^{prod}(E_{P,0}) + \sigma_{Z,X}^{prod}(E_{P,f}))/2. \tag{2.18}$$

The energy range over which this approximation is valid, depends on the start energy $E_{P,0}$ and on the dependence of the cross section on the energy, which varies from element to element. The translation of the energy range to the sample thickness depends on the sample composition. Using this approximation and using Eq. 2.4 to transform the integral over E_P to a integral over x, we obtain

$$\begin{aligned} Y(X_Z) &= N_P\frac{N_{Av}}{M_Z}c_Z\,\overline{\sigma_{Z,X}^{prod}}\varepsilon_{abs}(E_{X_Z})\,\rho_S\int_0^t\exp\left\{-\frac{\mu_t(E_{X_Z})}{\rho_S}\frac{\cos\alpha}{\cos\theta}\rho_S x\right\}dx \\ &= N_P\frac{N_{Av}}{M_Z}c_Z\,\overline{\sigma_{Z,X}^{prod}}\varepsilon_{abs}(E_{X_Z})\frac{\cos\theta}{\cos\alpha\,\mu_t(E_{X_Z})/\rho_S}\left(1 - T_S(E_{X_Z}, t)\right) \end{aligned} \tag{2.19}$$

The second condition

With the next condition, it is not possible to calculate the concentration, only the mass of trace elements.

Assumption 16 *The sample and the particle beam are spatially homogeneous, only the trace element Z can be distributed inhomogeneously over the sample area.*

This condition implies that ρ_S is almost independent of A and x, and n_P is independent of A. Only trace elements can be distributed inhomogeneously otherwise it affects ρ_S. The distributions of the trace elements in the depth have to be homogeneous since it is otherwise not possible to seperate the integrals over A and E_P, where the integral over E_P is a transformation of the integral over the depth x. These conditions can be found in applications where a solution with contaminants is deposited on a filter material. The filter material then contains the matrix elements. The integral over the area can be calculated with the following result :

$$\rho_S \int_{A_T} c_Z(A)\, dA = m'_Z \tag{2.20}$$

with m'_Z the mass per unit length of element Z in A_T. This is the total mass per unit length of the sample if the sample surface A_S is smaller than the beam dimensions. Otherwise, it is the mass per unit length in the sample volume under ion bombardment. Multiplying m'_Z with the sample thickness t gives the total mass of element Z in the sample, m_Z. Eqs. 2.11 and 2.12 can be rewritten with Eq. 2.20 to

$$Y(X_Z) = n_P \frac{N_{Av}}{M_Z} \frac{m'_Z t}{\rho_s t} \varepsilon_{abs}(E_{X_Z}) \int_{E_{P,0}}^{E_{P,f}} \frac{\sigma_{Z,X}^{prod}(E_P) T_S(E_{X_Z}, E_P)}{S_t(E_P)}\, dE_P \tag{2.21}$$

with $T_S(E_{X_Z}, E_P)$ given by Eq. 2.16. The formula can be rewritten for the same two sample types as given above. For thin targets, when Condition 14 is met, Eq. 2.21 can be simplified to give

$$Y(X_Z) = n_P \frac{N_{Av}}{M_Z} m_Z \sigma_{Z,X}^{prod}(E_{P,0}) \varepsilon_{abs}(E_{X_Z}) \tag{2.22}$$

with m_Z the total mass of element Z in the sample. In this case, it is no longer necessary that Condition 10 must apply. Thus thickness variations are now allowed. The factor $N_{Av} m_Z / M_Z$ is the total number of atoms of element Z in the sample. The factor n_P is N_P / A_B, the total number of projectiles per unit area. For intermediate thick samples, Condition 15 must be valid, the same approach can be used as for Eq. 2.19. Eq. 2.21 then becomes

$$Y(X_Z) = n_P \frac{N_{Av}}{M_Z} \frac{m_Z}{\rho_S t} \overline{\sigma_{Z,X}^{prod}} \varepsilon_{abs}(E_{X_Z}) \frac{\cos\theta}{\cos\alpha} \frac{(1 - T_S(E_{X_Z}, t))}{\mu_t(E_{X_Z})/\rho_S} \tag{2.23}$$

Table 2.1: Summary of the combinations of the conditions under which the different formulas in this subsection are valid.

sample uniformity	beam uniformity	beam area	sample thickness		results
homogeneous (Cond. 13)	inhomo-geneous	smaller	thick →	Eq. 2.15 & Eq. 2.16	c_Z
			intermediate →	Eq. 2.19	c_Z
			thin →	Eq. 2.17	c_Z
matrix homog. (Cond. 16)	homo-geneous	envelopping	thick →	Eq. 2.21 & Eq. 2.16	m_Z
			intermediate →	Eq. 2.23	m_Z
			thin →	Eq. 2.22	m_Z
inhomogeneous (Cond. 17)	homo-geneous	envelopping	thick →	-	
			intermediate →	-	
			thin →	Eq. 2.24	m_Z

The third condition

The last condition is least strict, the resulting formulas also are the least useful.

Assumption 17 *The particle beam is spatially homogeneous but the sample is not.*

This means that only n_P is independent of A. Now, it is not possible to separate the integrals over A and x. Consequently, it is not possible to arrive at a formula which can be used in calculations. Only if Condition 14 for thin targets is valid, it is possible to give a useful formula:

$$\begin{aligned} Y(X_Z) &= n_P \frac{N_{Av}}{M_Z} \sigma_{Z,X}^{prod}(E_{P,0}) \varepsilon_{abs}(E_{X_Z}) \int_{A_T} c_Z(A) \rho_S(A)\, dA\, t \\ &= n_P \frac{N_{Av}}{M_Z} m_Z\, \sigma_{Z,X}^{prod}(E_{P,0}) \varepsilon_{abs}(E_{X_Z}) \end{aligned} \quad (2.24)$$

Be aware that m_Z only is the total mass of element Z in the sample if the sample is completely enveloped by the particle beam ($A_S \subset A_B$). Again, as for Eq. 2.22, thickness variations are allowed.

The thick target PIXE formula Eq. 2.15 with Eq. 2.16 is used in the remainder of this thesis unless otherwise noted. The sample has to be homogeneous in order to be able to use this formula. In other cases, one of the equations 2.22, 2.23 or 2.24 has to be used. In Table 2.1, the results of this subsection are summarized.

2.2 Secondary Fluorescence Yield

There are several secondary excitation processes able to create additional characteristic X-rays. These processes rely on different mechanism to ionize the sample

atoms. There are four possibilities: (1) ionization by other characteristic X-rays, (2) ionization by secondary electrons, (3) ionization by Auger electrons and (4) ionization by Bremsstrahlungs X-rays. The secondary electrons are produced in the sample by collision with the protons. The energy of the secondary electrons has a continious distribution with a maximum value for a head on collision. For 3 MeV protons, the maximum energy transfer is about 6 keV. This is also the maximum value of the produced X-rays. There are some secondary electrons with higher energies due to the binding energy of the electrons in the sample atoms before collision. The cross section for the production of secondary electrons is considerable, especially for low electron energy, but the range of a few keV electrons in matter is very short. The cross section for ionization by electrons is also high but the short range of the electrons limits their effectiveness. There is very little relevant data about this subject and it may result in an enhancement of the yield for light elements of a few percent [Ahl 77]. About the same arguments hold for the ionization by Auger electrons as for the ionization by secondary electrons; however, there is one extra condition: There has to be an element present that produces Auger electrons with higher energies than the ionization energy needed for the X-ray lines of interest. In this case, the first secondary process cited above is dominant because the range of the X-rays is much longer than the range of the Auger electrons. Also, for the ionization by Bremsstrahlungs X-rays, the same arguments as for the ionization by secondary electrons hold. The ionization by this process is even smaller since Bremsstrahlungs X-rays are mainly produced by secondary electrons, which makes this a tertiary process with corresponding smaller cross sections. Of the four processes, the ionization by characteristic X-rays, called Secondary Fluorescence (SF), is the only process with a sufficiently high yield that correction for it is necessary [Ahl 77]. This process is treated in the rest of this section.

SF is a process whereby characteristic X-rays produced in the target can, in their turn, ionize target atoms that can then produce new X-rays. These last X-rays have a lower energy than the ionizing X-rays. In this section, a formula is derived for the SF yield. There are several derivations given in literature [Reu 75, Smi 85]. In the present derivation, special attention is paid to the physical meaning of the final formula. To simplify the derivation, several assumptions are made beforehand; they are:

Condition 1 *The sample is homogeneous.*

This means that ρ_S, S_t and μ_t do not depend on the position on the sample.

Condition 2 *The particle beam enters the sample parallel to the sample surface normal ($\alpha = 0$, in Fig. 2.1).*

Also, conditions 1-12 from Section 2.1 must be valid. Assumptions 5 and 6 must be valid for the A X-rays. The case for B X-rays is treated later on. The derivation

of the SF yield is only done for K-shell X-rays. It can, however, easily be extended for L-shell X-rays.

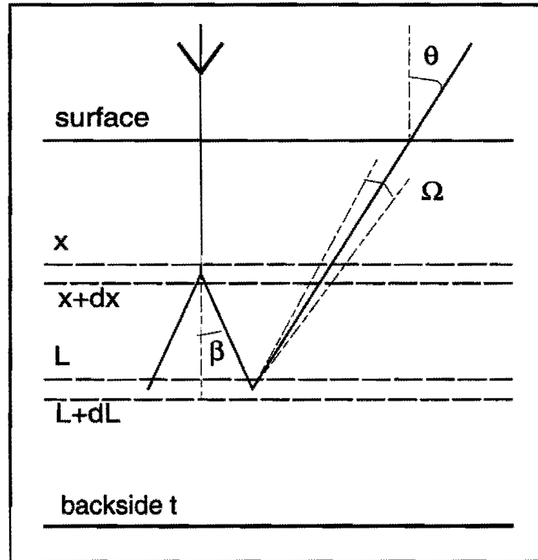

Fig. 2.3: Schematic drawing of the production of secondary X-rays of element A in layer $(L, L+dL)$ by primary X-rays of element B produced in layer $(x, x+dx)$. The movement of the B X-rays to layer $(L, L+dL)$ is in a cone of revolution. The top angle of the cone is 2β and the azimuthal angle is ϕ. The angle θ defines the direction of the detector with respect to the surface normal.

A schematic drawing of the SF process is given in Fig. 2.3. The element that produces the secondary X-rays is called element A and the element which produces the primary X-rays is called element B. The calculation of the SF process can be divided in a number of steps:

1. Calculate the production of X-rays of element B in layer $(x, x+dx)$.
2. Calculate the transmission of B X-rays from layer $(x, x+dx)$ to layer $(L, L+dL)$ with angles β and ϕ.
3. Calculate the production of A X-rays in layer $(L, L+dL)$ by B X-rays.
4. Integrate points 1 to 3 over all layers $(x, x+dx)$ and over all angles β and ϕ to obtain the total number of X-rays of element A produced in layer $(L, L+dL)$ by X-rays of element B reaching this layer.
5. Calculate the transmission of A X-rays through the sample in the direction of the detector and the detection in the detector.
6. Integrate points 4 and 5 over all layers $(L, L+dL)$ in the sample.

Now, these points will be investigated in detail.

1. The number of X-rays of element B produced in layer $(x, x+dx)$ $(= dN_B(x))$ can be derived from the formula for the thin target yield (Eq. 2.17)

$$dN_B(x) = \frac{dN_B(x)}{dx}dx = N_P \frac{N_{Av}}{M_B} c_B \sigma_{B,X}^{prod}(x) \rho_S dx \tag{2.25}$$

All terms are explained in section 2.1. Note that for $\sigma_{B,X}^{prod}$ the dependency on the depth x is used rather then the dependency on the particle energy E_P.

2. There are two possibilities for the transmission probability of B X-rays from layer $(x, x+dx)$ to layer $(L, L+dL)$, namely $x < L$ and $x > L$. These transmission probabilities can be calculated with Eq. 2.7

$$T_{x<L}(E_{X_B}, x{\rightarrow}L, \beta) = \exp\left\{-\frac{\mu_t(E_{X_B})}{\rho_S}\rho_S\frac{L-x}{\cos\beta}\right\} \tag{2.26}$$

$$T_{x\geq L}(E_{X_B}, x{\rightarrow}L, \beta) = \exp\left\{-\frac{\mu_t(E_{X_B})}{\rho_S}\rho_S\frac{x-L}{\cos(\pi-\beta)}\right\} \tag{2.27}$$

Note that these equations are independent of ϕ. Note also that $\cos\alpha$ in Eq. 2.7 is one, that θ is replaced by ϕ and that there is no A and x dependence because the sample is assumed to be homogeneous.

3. Let us call the probability that an X-ray of element B produces an X-ray of element A when passing through a layer $(L, L+dL)$ under angle β, $P(E_{X_B}{\rightarrow} E_{X_A}, L, \beta)$. This probability is given by

$$P(E_{X_B}{\rightarrow}E_{X_A}, L, \beta) = \frac{\tau_{A,K}(E_{X_B})}{\rho_S}\omega_{A,K} b_{A,X} \rho_S c_A \frac{dL}{|\cos\beta|} \tag{2.28}$$

with

$\tau_{A,K}(E_{X,B})$ photo-electric absorption coefficient for ionization of the K-shell of element A by a B X-ray (units cm^{-1}). This is divided by ρ_S to obtain the mass absorption coefficient,

$\rho_s c_A \frac{dL}{|\cos\beta|}$ mass thickness of element A which is encountered by the B X-ray on its passage through the layer $L, L+dL$ (g/cm^2).

The other factors are described in section 2.1. The absolute value for $\cos\beta$ is needed when $x > L$. Alternatively: $|\cos\beta| = \cos\beta$ when $x < L$ and $|\cos\beta| = \cos(\pi-\beta)$ when $x > L$. This case is analogous to that of the production of X-rays by particles except that the scattering cross section $\sigma_{Z,K}^{ion}$ is replaced by the absorption coefficient $\tau_{Z,K}$. In the case of element

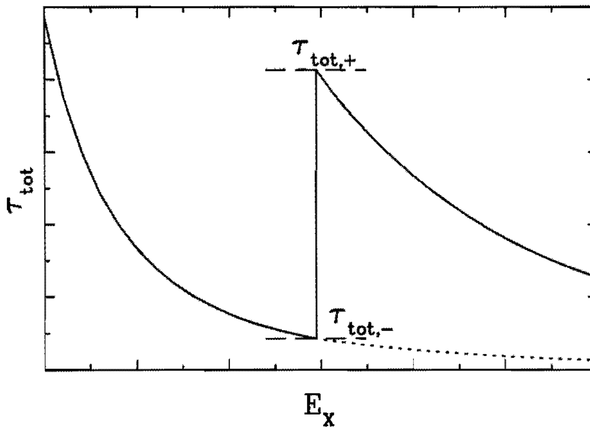

Fig. 2.4: Graph of the photo-electric absorption coefficient τ_{tot} as a function of the X-ray energy on arbitrary scales.

A, $\tau_{A,K}(E_{X_B})$ is zero when $E_{X_B} < E_{A,K}$ with $E_{A,K}$ the energy of the absorption edge of the K-shell of element A. This leads to the following condition, necessary for secondary fluorescence:

Condition 3 *The X-ray energy of element B, E_{X_B}, is larger than the K-shell absorption edge of element A, $E_{A,K}$.*

It should be noted that since $\tau_{A,K}$ decreases rapidly with increasing B X-ray energy the SF yield is only significant for B X-rays with an energy above and near the K absorption edge of element A. A problem in using Eq. 2.28 is that not $\tau_{A,K}$ is known but $\tau_{A,tot}$ (see Fig. 2.4). These two quantities are related according to the following formula :

$$\tau_{A,tot}(E_{X_Z}) = \tau_{A,K}(E_{X_Z}) + \sum_{i=1}^{3} \tau_{A,Li}(E_{X_Z}) + \sum_{i=1}^{5} \tau_{A,Mi}(E_{X_Z}) + ... \quad (2.29)$$

The number of terms needed in this equation depends on the atomic number Z. This equation is not useful for obtaining a value for $\tau_{A,K}$, so we make the following assumption:

Condition 4 $\frac{\tau_{A,K}(E_{X_Z})}{\tau_{A,tot}(E_{X_Z})} = const.$ *for all energies* $E_{X_Z} > E_{A,K}$

This relation is not strictly true but it varies only slowly with energy [Sto 70, page 569]. We now introduce the absorption edge ratio for the K-shell of

element A, $r_{A,K}$, defined as

$$r_{A,K} \equiv \frac{\tau_{A,tot,+}(E_{A,K})}{\tau_{A,tot,-}(E_{A,K})} \tag{2.30}$$

with $\tau_{A,tot,+}(E_{A,K})$ the total photo-electric absorption coefficient just above the absorption edge energy $E_{A,K}$ and $\tau_{A,tot,-}(E_{A,K})$ the total photo-electric absorption coefficient just below $E_{A,K}$. Now, $\tau_{A,K}(E_{A,K})$ is just the difference between $\tau_{A,tot,+}$ and $\tau_{A,tot,-}$. Combining Assumption 4 with Eq. 2.30, we obtain

$$\frac{\tau_{A,K}(E_{X_B})}{\tau_{A,tot}(E_{X_B})} \approx \frac{\tau_{A,K}(E_{A,K})}{\tau_{A,tot,+}(E_{A,K})} = 1 - \frac{1}{r_{A,K}} \tag{2.31}$$

Substituting Eq. 2.31 in Eq. 2.28 gives

$$P(E_{X_B} \rightarrow E_{X_A}, L, \beta) = \tau_{A,tot}(E_{X_B})(1 - \frac{1}{r_{A,K}})\omega_{A,K} b_{A,X} c_A \frac{dL}{|\cos\beta|} \tag{2.32}$$

4. Steps 1,2 and 3 together result in the number of A X-rays $dY_{SF,0}(X_A, X_B, x, L, \beta)$ produced in layer $(L, L + dL)$ by B X-rays, which are produced in $(x, x + dx)$ and are emitted in a direction characterized by the angles β and ϕ.

$$\begin{aligned} & dY_{SF,0,x \lesseqgtr L}(X_A, X_B, x, L, \beta) \\ = \quad & \frac{dN_B(x)}{dx} dx \, T_{x \lesseqgtr L}(E_{X_B}, x \rightarrow L, \beta) P(E_{X_B} \rightarrow E_{X_A}, L, \beta) \end{aligned} \tag{2.33}$$

This equation has to be integrated over the solid angle and all layers $(x, x + dx)$ to find the total number of A X-rays $dY_{SF,0}(X_A, X_B, L)$ produced in layer $(L, L + dL)$ by B X-rays. The integration order can be changed because the solid angle (determined by angles β and ϕ) and x are independent variables. These integrals have to be done in two steps because x can be larger or smaller than L. First, the integration over the solid angle is performed by integrating $d\Omega = \sin\beta d\beta \, d\phi$ with the normalization $\int d\Omega = 4\pi$.

$$\begin{aligned} & dY_{SF,0}(X_A, X_B, L, x) \\ = \quad & \frac{1}{4\pi} \int_0^{\pi/2} d\beta \, \sin\beta \int_0^{2\pi} d\phi \, dY_{SF,0,x<L}(X_A, X_B, x, L, \beta) \\ & + \frac{1}{4\pi} \int_{\pi/2}^{\pi} d\beta \, \sin\beta \int_0^{2\pi} d\phi \, dY_{SF,0,x \geq L}(X_A, X_B, x, L, \beta) \\ = \quad & \frac{1}{2} \int_0^{\pi/2} d\beta \, \sin\beta dY_{SF,0,x<L}(X_A, X_B, x, L, \beta) \\ & + \frac{1}{2} \int_{\pi/2}^{\pi} d\beta \, \sin\beta dY_{SF,0,x \geq L}(X_A, X_B, x, L, \beta) \end{aligned} \tag{2.34}$$

Next, we can integrate over x.

$$dY_{SF,0}(X_A, X_B, L) = \frac{1}{2}\int_0^L dx \int_0^{\pi/2} d\beta \sin\beta \frac{dY_{SF,0,x<L}(X_A, X_B, x, L, \beta)}{dx} + \frac{1}{2}\int_L^t dx \int_{\pi/2}^{\pi} d\beta \sin\beta \frac{dY_{SF,0,x\geq L}(X_A, X_B, x, L, \beta)}{dx} \quad (2.35)$$

with t the total target thickness.

5. The transmission probability of the A X-rays in the direction of the detector (angle θ) is analog to Eq. 2.7 ,:

$$T(E_{X_A}, L \rightarrow \text{surface}) = \exp\left\{-\frac{\mu_t(E_{X_A})}{\rho_S}\rho_S \frac{L}{\cos\theta}\right\} \quad (2.36)$$

The absolute detection efficiency of the detector, $\varepsilon_{abs}(E_{X_A})$, is given by Eq. 2.8.

6. Finally, eqs. 2.35 and 2.36 have to be integrated over all layers $(L, L+dL)$ to obtain the total number of detected A X-rays produced by B X-rays:

$$Y_{SF}(X_A, X_B) = \int_0^t dL \frac{dY_{SF,0}(X_A, X_B, L)}{dL} T(E_{X_A}, L \rightarrow \text{surface}) \varepsilon_{abs}(E_{X_A}) \quad (2.37)$$

To obtain the full equation, Eq. 2.37 has to be combined with eqs. 2.26, 2.27, 2.32, 2.33, 2.35, 2.36.

$$Y_{SF}(X_A, X_B) = \frac{1}{2}\frac{\tau_{A,tot}(E_{X_B})}{\rho_S}(1 - \frac{1}{r_{A,K}})\omega_{A,K} b_{A,X} \rho_S c_A \varepsilon_{abs}(E_{X_A}) \int_0^t dL \exp\left\{-\frac{\mu_t(E_{X_A})}{\rho_S}\rho_S \frac{L}{\cos\theta}\right\} \left(\int_0^L dx \int_0^{\pi/2} d\beta \frac{\sin\beta}{\cos\beta}\frac{dN_B(x)}{dx}\exp\left\{-\frac{\mu_t(E_{X_B})}{\rho_S}\rho_S \frac{L-x}{\cos\beta}\right\} + \int_L^t dx \int_{\pi/2}^{\pi} d\beta \frac{\sin\beta}{\cos(\pi-\beta)}\frac{dN_B(x)}{dx}\exp\left\{-\frac{\mu_t(E_{X_B})}{\rho_S}\rho_S \frac{x-L}{\cos(\pi-\beta)}\right\}\right) \quad (2.38)$$

with $dN_B(x)$ given by Eq. 2.25. This threefold integral can be simplified and one integral can be solved analytically. The full calculations can be found in Appendix B. The result of these calculations is a final formula for the SF yield :

$$Y_{SF}(X_A, X_B) = f_A(E_{X_A}, E_{X_B}) \int_{E_{P,0}}^{E_{P,f}} \frac{dN_B(E_P)}{dE_P}\left\{T_{0\leq L\leq x}(x) + T_{x\leq L\leq t}(x)\right\} dE_P \quad (2.39)$$

with

$$f_A(E_{X_A}, E_{X_B}) = \frac{1}{2}\tau_{A,tot}(E_{X_B})(1 - \frac{1}{r_{A,K}})\omega_{A,K} b_{A,X} c_A \varepsilon_{abs}(E_{X_A}) \quad (2.40)$$

$$\frac{dN_B(E_P)}{dE_P} = N_P \frac{N_{Av}}{M_B} c_B \sigma^{prod}_{B,X}(E_P) \frac{1}{S_t(E_P)} \quad (2.41)$$

$$T_{0\leq L\leq x}(x) = \frac{1}{p}\exp(-px)\ln(\frac{q}{|-p+q|}) + \int_1^\infty \frac{\exp(-qxy)}{y(p-qy)}dy \quad (2.42)$$

and

$$T_{x\leq L\leq t}(x) = \frac{1}{p}\exp(-px)\ln(\frac{p+q}{q}) - \int_1^\infty \frac{\exp(-q(t-x)y-pt)}{y(p+qy)}dy \quad (2.43)$$

Here, p stands for $\frac{\mu_t(E_{X_A})}{\rho_S}\frac{\rho_S}{\cos\theta}$ and q for $\frac{\mu_t(E_{X_B})}{\rho_S}\rho_S$. When given in this form, it is easy to see the physical meaning of the various terms. The variable dN_B (Eq. 2.41) gives the total number of X-rays with energy E_{X_B} produced at proton energy E_P thus at depth x in the sample, it is dimensionless. The quantity f_A (Eq. 2.40) describes the production cross section for the production of an X-ray with energy E_{X_A} by an X-ray of line X_B multiplied by the absolute detector efficiency (detector efficiency times solid angle) and by the concentration of element A. The dimension of f_A is cm^{-1}. The two transmission correction terms (Eq. 2.42 and 2.43) represent the transmission of the X-ray of line X_B from layer $(x, x+dx)$ at angle β to layer $(L, L+dL)$ and the transmission of the X-ray of line X_A from layer $(L, L+dL)$ to the detector at an angle θ. The quantity $T_{0\leq L\leq x}$ gives this transmission integrated over all depths L, lying between the sample surface and the depth x, and integrated over all angles β. The quantity $T_{x\leq L\leq t}$ is analogous to the first transmission but it is integrated over the depths L between depth x and the back side t of the sample. The dimension of the two transmission correction terms is cm. The integration over L introduces the dimension. The thickness t can be replaced by ∞ if the sample is thick enough. The last term in Eq. 2.43 then becomes 0. The last term in Eq. 2.42 can give problems when it has to be integrated numerically because the function of y to be integrated contains an asymptote between the integration bounderies 1 and ∞ when $p > q$. A solution to this problem of numerical integration is given in Appendix B.

In addition to the assumptions given in the beginning of this section, there is one extra assumption necessary for the validity of Eq. 2.39. In step two, we have used the total X-ray attenuation coefficient $\mu_t(E_{X_B})$ for the calculation of the transmission of B X-rays to layer $(L, L+dL)$. This is not completely justified because a part of the B X-rays is coherently scattered and then remains in the sample with the same energy although moving in a different direction. These X-rays still can ionize atoms of element A but at a different place. It is therefore better to use $\mu - \sigma_{coh}$ in Eq. ??. For incoherently scattered X-rays, the case is

somewhat different since the energy of the B X-rays after scattering has decreased. There still is the condition that the energy of the X-rays after scattering must be higher than the ionization energy for element A. The following equation gives the X-ray energy E_{inc} after scattering by a single free electron [Com 35]:

$$E_{inc} = \frac{E_0}{1 + \frac{E_0}{m_0 c^2}(1 - \cos\theta)} \tag{2.44}$$

with
E_0 X-ray energy before scattering
θ scattering angle
m_0c^2 = 511 keV

For X-rays with an energy up to 40 keV, the energy after scattering lies in the interval $[0.86E_0, E_0]$. For small scattering angles and low X-ray energies E_{inc} is close to E_0. Therefore, the argument used for coherent scattering is also valid and it is better to use $\mu - \sigma_{coh} - \sigma_{incoh}$ in Eq. ??. Nevertheless, we give the following assumption:

Assumption 5 *The total X-ray attenuation coefficient μ can be used instead of $\mu - \sigma_{coh} - \sigma_{incoh}$.*

It is possible to do this because in the case of an X-ray with an energy below 40 keV the photo-electric absorption coefficient is the dominant factor. Both scattering terms only make up a few percent of the total X-ray attenuation coefficient.

It should be noted that there is a possibility for a more complicated form of secondary fluorescence. It is possible that B X-rays produce X-rays of element C which in turn produce the X-rays of element A. This is called the third element effect. This effect will usually be very small except for special combinations of elements and concentrations.

In a practical situation, the total yield of an X-ray line $(Y(X_A))$ is measured. This is a combination of the primary yield for that line $(Y_P(X_A))$ and all the possible combinations of SF yields $(Y_{SF}(X_A, X_B))$ according to

$$Y(X_Z) = Y_P(X_A) + \sum_{X_B} Y_{SF}(X_A, X_B) \tag{2.45}$$

The summation has to be carried out over all X-ray lines able to excite the K-shell of element A when X_A is an X-ray line from the K-shell. A new quantity $R(SF/P) = \sum_{X_B} Y_{SF}(X_A, X_B)/Y_P(X_A)$ is introduced to be able to establish the importance of the SF yield in comparison with the primary PIXE yield.

2.3 The Data Base

2.3.1 Introduction

To be able to solve the thick target PIXE formula (Eq. 2.15 with Eq. 2.16), the values for various physical quantities are needed. A set of these values is generally

called the data base. The quantities in the data base are the stopping power $S(E_P)$, the ionization cross section $\sigma^{ion}_{Z,K}(E_P)$, the fluorescence yield $\omega_{Z,K}$, the branching ratio $b_{Z,X}$, the Coster-Kronig transition rate f^s_{ij} and the linear mass absorption coefficient $\mu_Z(E_X)$. The values of these quantities must either be calculated from theory or be determined experimentally.

There are several general reviews about the relevant data bases [Joh 88, Coh 87, Cam 83] as well as many reviews of only one specific physical quantity [Cam 89, Che 89, Coh 85, Cre 87, Zie 85] etc. . Shorter discussions about the data base are presented in articles concerning programs for the calculation of the thick target yield [Max 89, Orl 90]. The purpose of this section is finding the best or most useful values of the quantities in the data base and establishing the uncertainties in these values. We therefore do not give a general review but we limit ourselves to the most recent information. In view of its use in PIXE, the following limits for our data base are imposed:

- particles : protons,
- particle energy range : 0.1 - 10 MeV,
- X-ray energy range : 1 - 40 keV, K-shell X-rays,
- target atomic number : 11 - 92 and for stopping powers only: 1 - 92.

The values for the L-shell are treated in Appendix A. The data base is extended with the data for the non Rutherford scattering cross sections for several elements beause in many cases NBS is used for the determination of the thickness of the sample and the concentrations of the light elements ($Z \leq 10$).

2.3.2 Stopping Power

The stopping power for individual elements is probably the most accurately known quantity of the database. Some results for the stopping power for Helium is used below because it can useful information about the accuracy of the stopping power for protons. Two recent and comprehensive data sets are those of Janni [Jan 82] and Ziegler *et al.* [Zie 85]. Janni uses a semi-empirical approach and has given error estimates for all tabulated values, but for protons only. The error is about 2% for 3 MeV protons averaged over 20 elements spread over the periodic table. The error increases for lower proton energies. The values are available in the form of tables in ref. [Jan 82].

Ziegler *et al.* give theoretical formulas for the stopping power. Their values are available in the computer program TRIM. They have compared their results with experimental data. For all elements ($1 \leq Z \leq 92$) and all bombarding ions, they find an average deviation of 26% for ion energies ranging from 0-25 keV, of 8% for ion energies between 25-200 keV and of 4% for the range 200-100,000 keV. These errors are averaged over all experimental data and large deviations from

the average of only a few experiments can have significant impact on the value of the average ([Zie 85, page 166]). Therefore, Ziegler *et al.* give a percentage of the available values which are accurate within 10 or 20%. Johansson *et al.* [Joh 88] conclude that the disagreement between experimental and calculated values is about 1 to 2% for the proton energy range of 1-4 MeV.

The energy range can be divided in three regions. The lowest one is the energy range up to the Bohr velocity, $v_0 = 25$ keV/amu. In the next range, a maximum in the stopping power is reached at about $v_{max} = 3v_0 Z_P^{2/3}$, with Z_P the particle atomic number. The third range is the high energy range above 1 MeV for protons. This is the so-called Bethe region. The uncertainty in the stopping power in the lowest energy region is largest but the lower energy limit of the data base is chosen above the Bohr velocity for protons.

For a few selected elements, there is a very recent review of experimental data for the proton energy range of 10-2500 keV and the helium range of 60-7500 keV [Pau 91]. For these data, Paul *et al.* have given empirical fits, which are for protons in general lower than the values of Ziegler *et al.* [Zie 85], by several percent at 100 keV. The fitted values for He ions on Ag and Au are in better agreement with other data sets. The relative accuracy of the fits of Paul *et al.* in the region of 51-250 keV is about 3%. Taking this into account, the uncertainty for the Ziegler values in the energy region of 100-200 keV probably does not exceed 5%. For our data base, we have chosen the stopping power values of Ziegler *et al.* [Zie 85], because of its accuracy and ease of use.

The discussion above is only valid for the stopping power of individual elements. These values must be summed according to Bragg's rule (Eq. 2.13) to arrive at the total stopping power of the sample. Bragg's rule, however, is a postulate and there is an abundance of evidence of its breakdown when the sample contains molecules with strong chemical bonds. There can also be differences in the stopping powers of the same element in different phases (solid/liquid/gas). Many of these studies have been reviewed by Thwaites ([Thw 83, Thw 85, Thw 87]). Differences have been found between the solid/liquid phase and the gas phase for H_2O and organic materials. The stopping power of these materials in the vapour phase can be up to 5-10% larger at the energy where the stopping power maximum reaches its maximum. At energies below the energy where the stopping power is maximum, the difference is still uncertain [Thw 85]. For more complex compounds, the differences between physical phases disappear. Another major problem for Bragg's rule is organic compounds. In this case, the chemical bonds influence Bragg's rule. Chemical bonds change the ionization state of outer electrons. This effect is most important for light elements where these electrons make up a large part of the total number of electrons, especially for hydrogen with only one electron. The deviations are largest around the maximum of the stopping power. Several solutions are proposed [Zie 88]. One solution is the weighted summation of groups instead of atoms (e.g. C-H_2). Another solution is the so called "cores and bonds"

approach. In this approach, the contribution of the core and valence electrons are added separately. Both models can improve the accuracy of the total stopping power. The second method is included in the TRIM89 program for several compounds. All differences tend to disappear for higher energies and, for ion velocities above $10v_0$, Bragg's rule can again be applied without corrections.

Ziegler *et al.* [Zie 88] also conclude that Bragg's rule holds within 2% for compounds made up of heavier elements. It can thus be concluded that the uncertainty in the stopping power in compounds is between 2-3% for protons above 1 MeV. The uncertainty increases to 10% for lower energies.

2.3.3 Ionization Cross Section

A number of theories for the calculation of the cross sections exist. The ECPSSR theory, developed by Brandt and Lapicki, is most widely used. [Bra 79, Bra 81]. This theory is based on the Plane Wave Born Approximation (PWBA) including corrections for Coulomb repulsion between projectile and target (C), polarization and binding energy changes via the perturbed stationary states (PSS), relativistic effects (R) and projectile energy loss (E). In the following paragraphs several tabulations based on this theory are discussed for K-shell ionization.

There are a number of tabulations for protons based on the ECPSSR theory, one of Cohen and Harrigan [Coh 85], using hydrogenic electron wave functions and another one of Chen and Crasemann [Che 85, Che 89], using Dirac-Hartree-Slater wave functions. The latter wave functions are somewhat more realistic than the hydrogenic ones. The last tabulation to be discussed is from Paul *et al.* ([Pau 86, Pau 89]). They have reviewed experimental data for K-shell ionization and have compared this with their own calculations based on the ECPSSR theory of Brandt and Lapicki. Paul *et al.* have found systematic deviations, most notably for low ion energies where the theory overestimates the cross sections. Based on the experimental values, Paul *et al.* have generated reference cross sections for protons with error estimates for all values. The error is generally less than 5% for medium range energies. The energy dependence of the cross section depends on Z. Therefore, the energy range of the error is also dependent on Z. Large errors, outside the medium energy range, are found for low Z values above 1 MeV (errors up to 10%) and for high Z values (above Z=40) for proton energies below 1 MeV (errors up to 20%). The above stated regions should not be taken too strictly and are only mentioned to give an impression of the energy dependence of the errors.

The values of Cohen and Harrigan for the region of high Z and low energy are even higher than the values of Paul *et al.* due to a slightly different calculation [Coh 89, Lap 87]). The difference increases to a factor 2 for Z=92 and 0.3 MeV. However, for this Z value the energy of the X-rays produced by K-shell ionization is too high to be measured by a normal Si(Li) detector and the cross section too small. The above stated errors are also confirmed in a recent review [Coh 90].

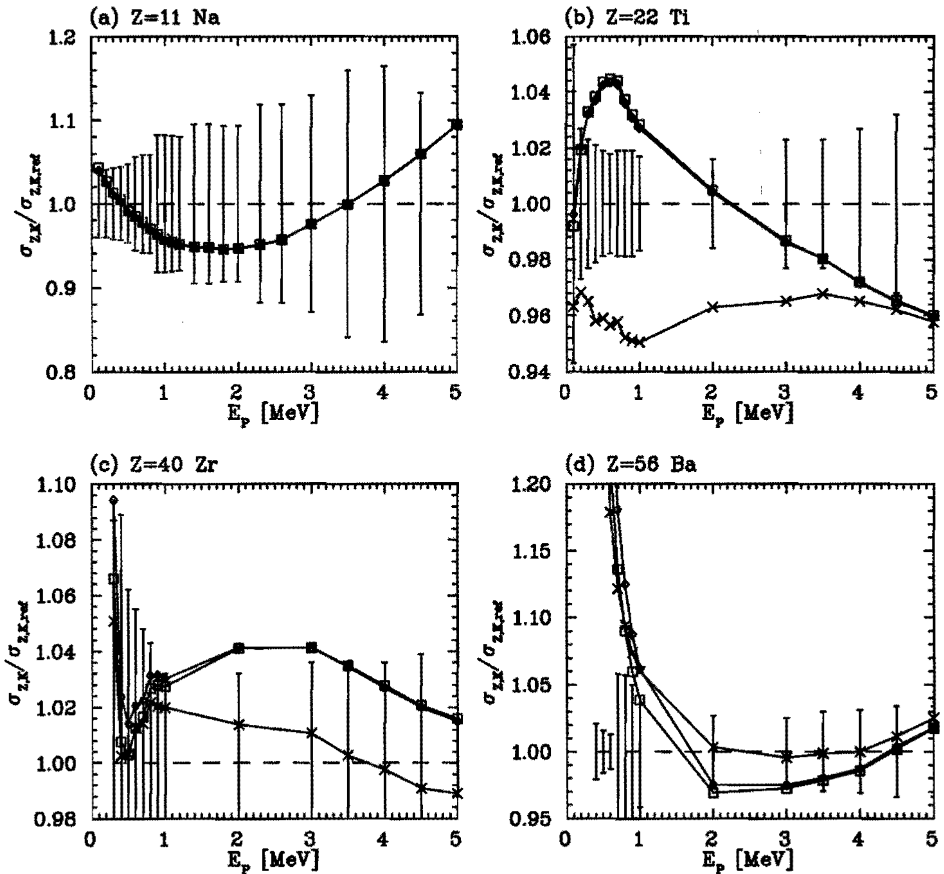

Fig. 2.5: Comparison of various theoretical ionization cross sections. The cross sections are normalized on the reference cross sections of Paul *et al.* [Pau 89] to eliminate the large energy dependence. x = ECPSSR theory of Chen *et al.* ([Che 85,Che 89]), □ = ECPSSR theory of Paul *et al.* ([Pau 89]) and ◇ = ECPSSR theory of Cohen & Harrigan ([Coh 85]). The error bars are the errors given by Paul *et al.* for their reference cross sections.

In Fig. 2.5 the different calculations are compared for selected values of Z. Generally the values of Chen and Crasemann are closer to the reference values of Paul *et al.* but their tabulations are limited to selected Z values and selected energies between 0.1 and 5 MeV. Maxwell *et al.* [Max 89] have used the tables of Chen and Crasemann to make fits using the semi-empirical formula of Johansson *et al.* ([Aks 74, Joh 76]). They have calculated the coefficients separately for all elements in the range $10 \leq Z \leq 60$ for the K-shell. They reproduced the tables of Chen and Crasemann within 1% for proton energies between 0.3 and 3 MeV.

The polynomial fits of Maxwell *et al.* are used when possible, since they

are based on the most accurate calculations and they facilitate fast calculations. Outside the energy range where the fits of Maxwell *et al.* are valid the calculations of Cohen and Harrigan are used because they are the most comprehensive. In most ranges relevant for PIXE the error in the K-shell ionization cross section is about 5%.

2.3.4 Branching ratio

Data about branching ratios are very often given as a ratio of line intensities, the most used ratio is the Kβ/Kα ratio. For high Z values there can be more transitions and the Kα and Kβ line groups are made up of several sublines. For the K-shell there exists a widely used semi-empirical table of fitted experimental data of Salem *et al.* [Sal 74]. The uncertainty for the Kβ/Kα ratio is estimated to be about 2%. Salem *et al.* have used data from experiments with radioactive sources or sources ionized by photon or electron bombardment. They have excluded data from ion bombardment since they claim it can create multiple vacancies and can alter the natural state of the atom. Scofield [Sco 74, Sco 74a] has done theoretical calculations both using Hartree-Slater wave functions and Hartree-Fock wave functions. The results using the Hartree-Fock theory are in better agreement with experiments than the Hartree-Slater theory. Careful evaluation of experimental data showed a discrepancy between experiment and the Hartree-Fock theory for the region $22 \leq Z \leq 32$. This discrepancy was confirmed by Perujo *et al.* [Per 87]

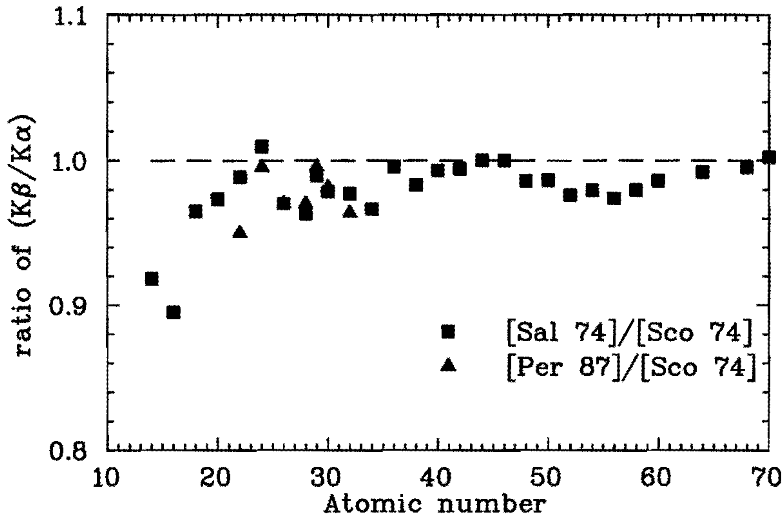

Fig. 2.6: Figure of the experimental Kβ/Kα intensity ratio divided by the theoretical Hartree-Fock intensity ratio of Scofield [Sco 74]. The experimental values are from Salem *et al.* [Sal 74] and Perujo *et al.* [Per 87].

who determined values for the Kβ/Kα ratio for seven elements with $22 \leq Z \leq 32$ and with uncertainties ranging from 0.7-1.2%. In Fig. 2.6 the experimental Kβ/Kα intensity ratios and the theoretical Hartree-Fock ratios are compared. This figure shows that the discrepancy between experiment and theory extends below the $22 \leq Z \leq 32$ region. Above this region the difference between experiment and theory is within the uncertainty (2%) for the values of Salem *et al.* . For our data base we have used the values of Scofield [Sco 74] with the values of Perujo *et al.* [Per 87] for the region $22 \leq Z \leq 32$. The uncertainty is estimated to be 2% except the region below $Z = 22$ where it will be larger.

2.3.5 Fluorescence Yield

The situation for the K-shell is quite simple because there are no subshells. The only quantity necessary for the K-shell is the fluorescence yield $\omega_{Z,K}$. For this quantity there is good agreement between theoretical calculations and experimental data. Theoretical calculations have been performed by Chen, Crasemann and Mark [Che 80], using relativistic Dirac-Hartree-Slater wave functions for 25 elements with $18 \leq Z \leq 96$. Compilations were made by Krause [Kra 79] for all elements with $5 \leq Z \leq 110$ and Bambynek [Bam 84] for $11 \leq Z \leq 60$. The compilations include both theoretical and experimental data. The estimated uncertainties for the compilations of Krause and of Bambynek are as follows: 5-10% and 3-5% for Z is 10-20, 3-5% and 1-3% for Z is 20-30, 3% and 0.5-1% for Z is 30-40 and 1-2% and 0.3-0.5% for Z is larger than 40. Within the uncertainties the experimental values agree with the theoretical values of Chen *et al.* The compilation of Bambynek is chosen for our data base since the uncertainties in these values are smallest.

2.3.6 X-ray Attenuation Coefficient

There are many schemes for the X-ray attenuation coefficient μ, both experimental compilations, semi-empirical schemes and tables based on theory. However, differences between the various values of μ can be as large as 10% (see the tables in [Joh 88] and [Cam 83]). In a recent article [Cam 89] various semi-empirical schemes and the theoretical values by Berger [Ber 90] are compared with high accuracy experimental data from the X-ray Attenuation Project of the International Union of Crystallography [Cre 87]. The experimental data is collected for C, Si and Cu. They [Cam 89] conclude from this comparison that the theoretical values agree better with experiment than the semi-empirical schemes. For the selected elements and for energies above the K-shell absorption edge, the difference between the experimental and the theoretical values is less than 3%. For the semi-empirical scheme of Thinh & Leroux [Ler 77, Thi 79]) the accuracy is estimated to be about 5% except near the L-shell absorption edges where the accuracy is 10% or worse [Cam 83]. This is the most widely used semi-empirical scheme because it is easy

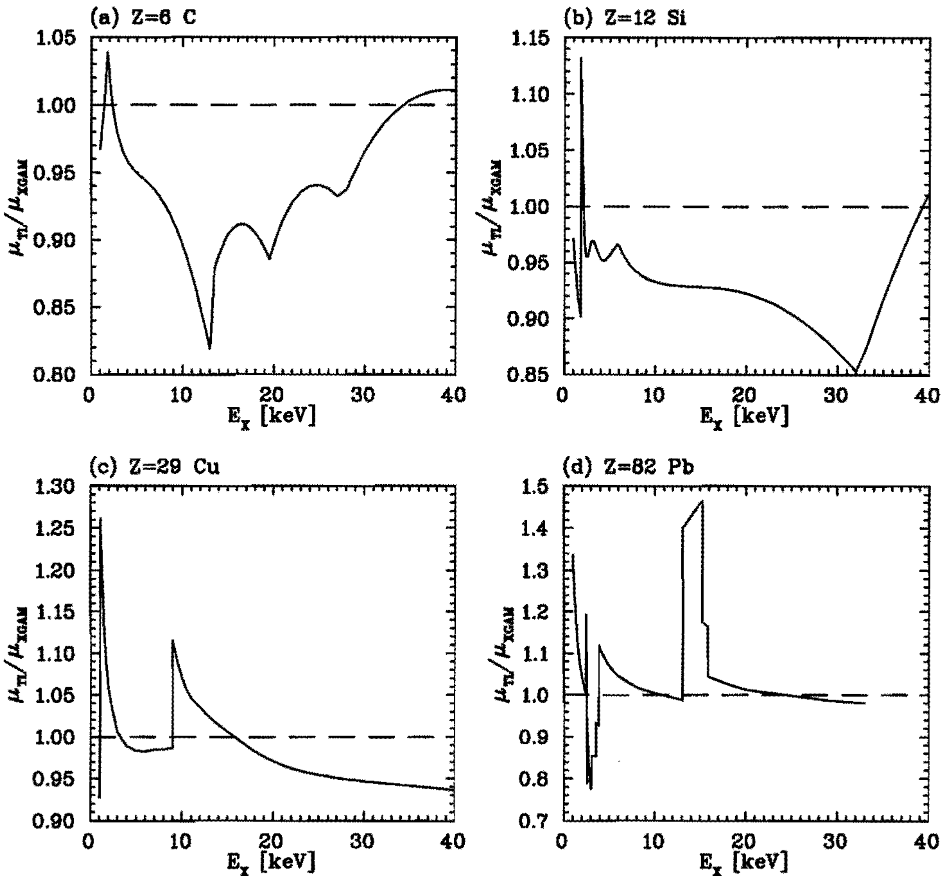

Fig. 2.7: Comparison of the mass attenuation coefficient as calculated by Thinh & Leroux [Thi 79] and by Berger [Ber 90], given as the ratio of the two values. The abrupt changes are either caused by absorption edges or by different fitting regions for the values of Thinh & Leroux.

to apply and it has a wide range for Z (1-94) and for the X-ray energy (1-40 keV). The comparison in [Cam 89] was limited to the X-ray energies above the K-shell absorption edges. Moreover, they didn't take into account a revision made by Thinh & Leroux to their scheme [Thi 79]. Therefore, we have made a comparison between the scheme of Thinh & Leroux and the program XGAM of Berger [Ber 90], see Fig. 2.7. From this figure, it can be concluded that the uncertainties stated above are probably still too optimistic. An uncertainty of 10% seems more realistic, with even larger values at the L-shell absorption edges. We have chosen to use the semi-empirical scheme of Thinh &Leroux, because of its ease of use and its wide applicability. As with the stopping power, the total X-ray attenuation coefficient of the sample is obtained by summing the individual values according to

the mass fraction (see Eq. 2.14). There is very little information about the validity of this summation rule. However, the main contribution to the X-ray attenuation coefficient of X-rays comes from the photo-electric absorption coefficient τ_{tot} (see Eq. 2.9). Especially for low Z elements, the inner shells contribute mostly to τ_{tot}. The most important factor leading to deviations of the summation rule are atomic bindings, which are made between outer-shell electrons. Therefore, the summation rule for the X-ray attenuation coefficient will in most cases be valid although there might be exceptions. Also, the X-ray attenuation coefficient of individual elements is not known with sufficient accuracy to allow conclusions to be made about the validity of the summation rule.

2.3.7 Scattering Cross Section

In many cases NBS is used to determine the mass thickness of the sample and the concentrations of the matrix elements with $Z \leq 10$. The matrix elements of a biological sample, for example, are mainly C, N and O. For these elements and three MeV protons, the Rutherford scattering cross section is not valid. Therefore alternative scattering cross sections have to be found.

A literature survey was done [Ude 92] to find values for the scattering cross sections for proton scattering on C, N and O with an energy range as large as possible but at least including the energy range 2-3 MeV. An additional condition is that these cross sections are available for the same scattering angle. The following articles were found to provide satisfactory data: [Jac 53] for proton scattering on C for the energy range 0.3-4.4 MeV and for the scattering angle 146.2° ; [Bas 59] for scattering on N with energies of 1.0-3.7 MeV and angle 147.2° ; and [Har 62] for scattering on O with energies of 2.5-5.6 MeV and angle 147.5° . The cited errors in the cross sections range from 3-5%. Afterwards, new data for the scattering cross sections for C and O is found in [Ami 93], which contains high precision data especially measured for micro-NBS analysis. The scattering angle for these data is slightly different viz. 150° . The reproducibility was 3% for most of the repeated data points. In Fig. 2.8 both data sets are compared for C and O. The difference between the two data sets is very small, within a few percent, with the exception of the resonance for O at about 3.5 MeV where it is much larger. The old data for the scattering cross section is still in use since we have fixed our measuring angle at 147° . Therefore, an average uncertainty of 5% is used.

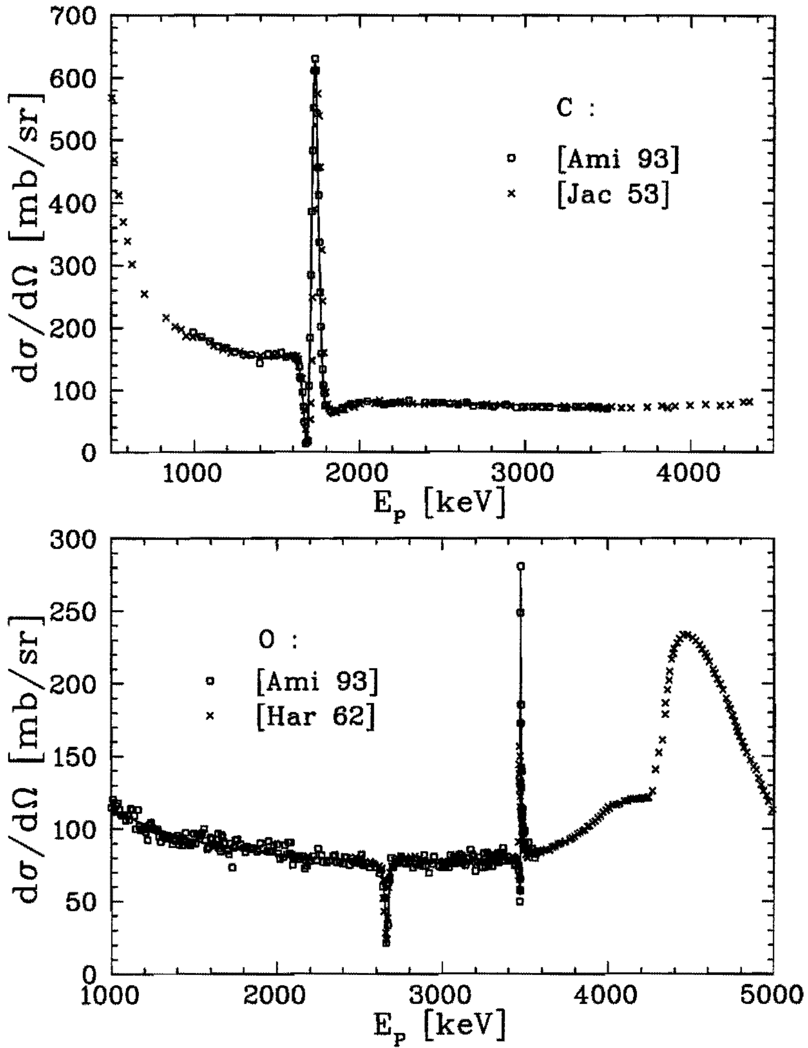

Fig. 2.8: Comparison of the scattering cross sections as a function of proton energy for C (top figure) and O (bottom figure). The solid line is a fit by Amirikas *et al.* [Ami 93] to the experimental data.

3 Error propagation of the uncertainty in various quantities to the uncertainty in the primary PIXE yield and Secondary Fluorescence yield. [1]

The uncertainty in the PIXE yield or concentration due to the uncertainty in various quantities is discussed for both the primary PIXE yield and the SF yield. The error propagation factor is determined, in a numerical approach, as the propagation of an uncertainty in a quantity to the uncertainty in the yield or concentration. The dependence of the error propagation factor on the X-ray and proton energies, and on the matrix composition is investigated for quantities, such as the ionization cross section, the stopping power, the X-ray attenuation coefficient, the matrix composition and the proton beam energy. The physical background of these dependencies is explained. This also facilitates obtaining a better physical insight in the formulas for the primary yield and the SF yield.

3.1 Introduction

In this chapter, the influence of errors in the ionization cross section, the stopping power, the X-ray attenuation coefficient, the matrix composition and the ion beam energy on the yield or the calculated concentration is investigated. These quantities are chosen because the propagation of errors in these quantities into the error of the yield is not trivial; for all other quantities necessary for the calculation of the yield the propagation is straightforward. The propagation of the uncertainty to the yield is in most cases identical to the propagation of the uncertainty to the concentration. Therefore, the propagation to the uncertainty in the concentration is only given where it deviates from the propagation to the yield. This study is done for both the primary PIXE yield (see Section 2.1) and for the Secondary Fluorescence (SF) yield (see Section 2.2). An estimate of the uncertainties in the quantities of the data base is given in Section 2.3. First, the error-calculation theory is described in Section 3.2. Then the propagation of these errors through the formulas of the primary yield and the SF yield is discussed in Section 3.3 and

[1] This chapter is based on an article by F. Munnik, P.H.A. Mutsaers, E. Rokita and M.J.A. de Voigt published in 'Int. J. of PIXE', vol. 3/2, (1993) 145.

Section 3.4 respectively. The objective is to obtain a basic understanding of these formulas and of the error propagation for the above mentioned quantities.

3.2 Uncertainty Calculation

An important aspect of any calibration procedure is the assessment of the uncertainties. Since we have chosen the absolute calibration method, we have to develop a form of uncertainty calculation to assess the influence of the uncertainty in various quantities on the uncertainty in the calculated concentration. Use has been made of general treatments of error analysis, such as [Bev 69, Bar 89], and of treatments more specific for ion beam analysis, such as in [Kno 79].

The rules determining the calculations of the uncertainties in the results are dependent on the type of uncertainty. Therefore, the type of uncertainty for the various quantities has to be established first. A common type of uncertainty is the standard deviation. In this case there is a 68% probability that the 'real' value of a quantity is situated in an interval of plus minus one standard deviation around the measured value. The underlying distribution is the Gaussian distribution or the binomial distribution. A more simple type of uncertainty is the maximum deviation. This type can be used for e.g. the reading of an instrument. Often, it is not known what the underlying distribution for a physical quantity is. However, if the uncertainty in this quantity is influenced by a large number of small effects, the uncertainty distribution may be approximated by a Gaussian distribution; even if the distributions for the effects are not Gaussian [Bar 89]. We assume that the uncertainties for the quantities needed for TT-PIXE can be treated as standard deviations of a Gaussian distribution because of the complex nature of the corresponding data.

Once the type of uncertainty is established, we can determine the type of uncertainty calculation. If all quantities are independent and the uncertainties are standard deviations, the most commonly used rules for the uncertainty calculation can be applied. The most general rule for the uncertainty s_y in a function y of the quantities $x_1, ..., x_n$ is in the Gaussian approximation:

$$s_y^2 = \sum_{i=1}^{n} \left(\frac{\partial y}{\partial x_i} s_{x_i} \right)^2 \tag{3.1}$$

with s_{x_i} the uncertainty in quantity x_i. The error calculations in this study are based on this rule unless stated otherwise. We now define the partial uncertainty in y caused by the uncertainty in x_i as $s_{y,x_i} = \frac{\partial y}{\partial x_i} s_{x_i}$. The error propagation factor can then be defined as:

$$P(y, x_i) = \frac{s_{y,x_i}}{y} \bigg/ \frac{s_{x_i}}{x_i} \tag{3.2}$$

If this factor is unity, the uncertainty in the quantity x_i is linearly translated into the result y and if this factor is close to zero, the uncertainty in the quantity can

be neglected. If all the error propagation factors and the uncertainties s_{x_i} are known, the total uncertainty in y can be calculated according to Eq. 3.1.

The error propagation factors to the yield for several quantities are calculated. The quantities are the ionization cross section $\sigma_{Z,K}^{ion}$, the stopping power S_t, the X-ray attenuation coefficient μ_t, the matrix composition and the ion beam energy $E_{P,0}$. For these quantities, except for μ_t, the error propagation factor cannot be calculated analytically because the formula for the yield (Eq. 2.15) contains an integral over E_P with functions of E_P that are not known analytically. For all other quantities, the error propagation factor is one. However, numerical calculations can be done using the approximation

$$\frac{\partial Y(x)}{\partial x}(x_0) \approx \frac{Y(x_0+\delta) - Y(x_0-\delta)}{2\delta}, \tag{3.3}$$

with x the quantity under investigation, x_0 the value of the quantity for which the partial error has to be calculated and δ a small step in the quantity x. The propagation factor for the uncertainty in x ($P_Z(Y,x)$) is then given by the following formula:

$$P(Y(X_Z),x) = \left(\frac{s_{Y,x}}{Y(x)}\right)_{x_0} \Bigg/ \frac{s_x(x_0)}{x_0} \approx \frac{Y(x_0+\delta) - Y(x_0-\delta)}{2Y(x_0)\delta/x_0}. \tag{3.4}$$

protons as bombarding particles and to K-shell X-rays. We always consider infinitely thick homogeneous targets with an unknown matrix. If the word error is used it should be read as uncertainty. Throughout this chapter, we have always taken the total detector efficiency $\varepsilon = 1$. The detector solid angle $\Omega = 10$ msr, so chosen because this is close to the value of our detector geometry. The yield is calculated for 1 μC of protons deposited on the target. Normally, the propagation factor $P(Y,x)$ should always be positive since the relative error always is positive. However, we have allowed the propagation factor to become negative because the sign of the propagation factor $P(Y,x)$ gives insight in how the yield behaves when the quantity x changes. The propagation factor $P(c_Z,x)$ for the uncertainty in the concentration due to the uncertainty in quantity x is equal to the negative value of $P(Y,x)$. This is not always true when x is the matrix composition, the exceptions are discussed in Section 3.3.4.

3.3 The Uncertainty in the Primary Yield

3.3.1 Introduction

Using the scheme described in the previous section, it is possible to calculate the total uncertainty in the yield given by the TT-PIXE formula (eqs. 2.15 and 2.16):

$$\left(\frac{s_Y}{Y(X_Z)}\right)^2 = \left(\frac{s_c}{c_Z}\right)^2 + \left(\frac{s_Q}{Q}\right)^2 + \left(\frac{s_\omega}{\omega_{Z,K}}\right)^2$$

$$+ \left(\frac{s_b}{b_{Z,X(K)}}\right)^2 + \left(P(Y(X_Z),\sigma)\frac{s_\sigma}{\sigma^{ion}_{Z,K}}\right)^2 + \left(P(Y(X_Z),S_t)\frac{s_S}{S_t}\right)^2$$
$$+ \left(\frac{s_\varepsilon}{\varepsilon(E_{X_Z})}\right)^2 + \left(\frac{s_T}{T_{\mathrm{abs}}(E_{X_Z})}\right)^2 + \left(\frac{s_\Omega}{\Omega}\right)^2$$
$$+ \left(P(Y(X_Z),\mu_t)\frac{s_\mu}{\mu_t}\right)^2 + \left(P(Y(X_Z),E_{P,0})\frac{s_E}{E_{P,0}}\right)^2 + \left(\frac{s_{Y,c}}{Y(X_Z)}\right)^2 \quad (3.5)$$

The experimental uncertainties $\frac{s_E}{E_{P,0}}$, $\frac{s_\varepsilon}{\varepsilon(E_{X_Z})}$, $\frac{s_T}{T_{\mathrm{abs}}(E_{X_Z})}$, and $\frac{s_\Omega}{\Omega}$ are given in Chapter 4 and $\frac{s_Y}{Y(X_Z)}$, and $\frac{s_Q}{Q}$ can be calculated as described in Chapter 4. The uncertainties in the data base are given in Section 2.3. The error propagation factors can be calculated according to Eq. 3.4 and are discussed in this section. The term $\frac{s_c}{c_Z}$ should only be added when element Z is not a matrix element, otherwise it is included in the term $\frac{s_{Y,c}}{Y(X_Z)}$. Also, the partial uncertainty in the concentration due to the matrix composition, $\frac{s_{Y,c}}{Y(X_Z)}$, is discussed in this section, although for only two matrix elements. The more complicated case of several matrix elements is discussed in Section 5.7.

In many practical cases, the concentration of the analyte element has to be calculated and the uncertainty in this concentration has to be known. Generally, the error propagation factor to the concentration is identical to that to the yield. The only exception is the error propagation factor for the matrix composition, which is different for the yield and the concentration. We discuss here the error propagation factor to the yield only, with the exception of the matrix composition where the error propagation factor to both the yield and the concentration is given. The uncertainty in the SF yield is discussed in Section 3.4.

3.3.2 Propagation Factor for the Cross Section

The calculation of the propagation factor for the cross section has one extra problem: the cross section depends on the proton energy E_P. Eq. 3.4 is only valid if we assume that s_σ/σ and δ_σ/σ are constant for all proton energies E_P. As mentioned in Section 2.3.3, the error increases at lower proton energy especially for larger Z values. Nevertheless this assumption does not introduce large errors as is shown in Section 3.3.5. The propagation factor using Eq. 3.4 under this assumption is

$$P(Y(X_Z),\sigma) = \frac{s_{Y,\sigma}}{Y(X_Z)} / \frac{s_\sigma}{\sigma} \approx 1. \quad (3.6)$$

A derivation is given in Appendix C. In consequence of Eq. 3.6, accurate cross section data is very relevant. However, when using cross section data with large errors the use of external thin or (preferably) thick standards reduces the error in the yield caused by the error in the cross section to a maximum of 5% and 1%, respectively [Cam 83].

3.3.3 Propagation Factor for the Stopping Power and the X-ray Attenuation Coefficient

The discussion for the propagation factor for the stopping power and the X-ray attenuation coefficient is combined because these factors are interrelated, as is shown later. The error in the total stopping power can be derived from the error in the stopping power of single elements using Eq. 2.13 (Bragg's rule) :

$$s_{S_t}^2 = \sum_i (c_i s_{S_i})^2 \Rightarrow \frac{s_{S_t}}{S_t} = \frac{\sqrt{\sum_i (c_i s_{S_i})^2}}{\sum_i c_i S_i} \tag{3.7}$$

with c_i the mass fraction of element i and S_i the stopping power of element i. This equation can be extended since c_i can also have an error as is discussed in Section 3.3.4. Eq. 3.7 does not give a simple dependence of s_{S_t}/S_t on s_{S_i}/S_i but it can be simplified if we assume that s_{S_i}/S_i is identical for every element i :

$$s_{S_t}/S_t \approx s_{S_i}/S_i \frac{\sqrt{\sum_i (c_i S_i)^2}}{\sum_i c_i S_i} \leq s_{S_i}/S_i. \tag{3.8}$$

The propagation factor $P(Y(X_Z), S_t)$ can be calculated using eqs. 3.4 and 3.8 under the assumption that the relative error in the stopping power, s_{S_i}/S_i, and the step in Eq. 3.4, δ_{S_t}/S_t, are constant for all ion energies E_P.

$$P(Y(X_Z), S_t) = \frac{s_{Y,S_t}}{Y(X_Z)} / \frac{s_{S_t}}{S_t} \approx - \frac{\int \frac{\sigma(E_P) T_S(E_{X_Z}, E_P)(1 + \ln T_S(E_{X_Z}, E_P))}{S_t(E_P)} dE_P}{\int \frac{\sigma(E_P) T_S(E_{X_Z}, E_P)}{S_t(E_P)} dE_P} \tag{3.9}$$

This formula is a first order approximation, valid for small values of δ_{S_t}/S_t; a derivation is given in Appendix C. For the above assumption, the same argument is used as for the cross section.

For the X-ray attenuation coefficient, the derivative $\partial Y(X_Z)/\partial \mu_t$ can be solved analytically since μ_t is independent of E_P. The propagation factor for μ_t is

$$P(Y(X_Z), \mu_t) = \frac{s_{Y,\mu_t}}{Y(X_Z)} / \frac{s_{\mu_t}}{\mu_t} = \frac{\int \frac{\sigma(E_P) T_S(E_{X_Z}, E_P) \ln T_S(E_{X_Z}, E_P)}{S_t(E_P)} dE_P}{\int \frac{\sigma(E_P) T_S(E_{X_Z}, E_P)}{S_t(E_P)} dE_P}, \tag{3.10}$$

and

$$s_{\mu_t}^2 = \sum_i (c_i s_{\mu_i})^2, \tag{3.11}$$

with c_i the mass fraction of element i and μ_i the X-ray attenuation coefficient of element i. The derivation of Eq. 3.10 is again given in Appendix C.

These two propagation factors are interrelated according to the following formula

$$|P(Y(X_Z), S_t) + P(Y(X_Z), \mu_t)| = 1 \tag{3.12}$$

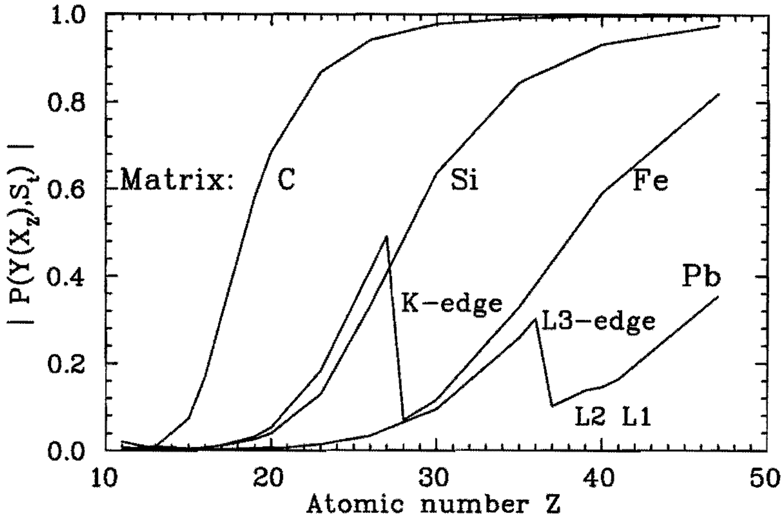

Fig. 3.1: Plot of $P(Y(X_Z), S_t)$ for several matrices as a function of atomic number of the element, for which the yield is calculated; $E_{P,0} = 3$ MeV.

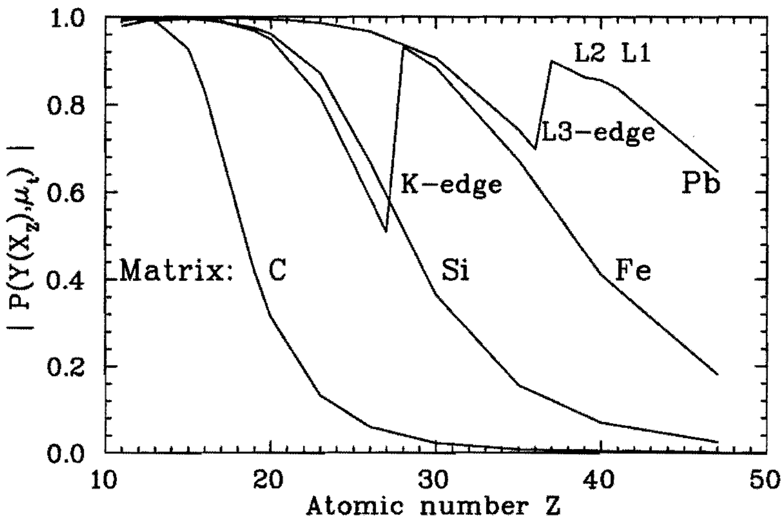

Fig. 3.2: Plot of $P(Y(X_Z), \mu_t)$ for several matrices as a function of atomic number of the element, for which the yield is calculated; $E_{P,0} = 3$ MeV.

This is simply the summation of eqs. 3.9 and 3.10. From a physical point of view, the two propagation factors are interrelated because the corresponding quantities are linked through the depth. The quantity that changes fastest as a function of depth, has the largest influence on the uncertainty in the yield. The propagation factors for S_t and μ_t are shown in figures 3.1 and 3.2 respectively for several

matrices. In Eq. 3.12 there are two extremities. In one extremity the propagation factor for the stopping power is one and the propagation factor for the X-ray attenuation coefficient is zero. In this approximation the error caused by the transmission T_S is neglected. In a practical situation this approximation is possible when T_S is large for all E_P. If $T_S \geq \frac{1}{e}$ for all proton energies then $T_S > -T_S \ln T_S$ for all E_P and it follows from Eq. 3.10 that the error propagation factor for μ_t is very small. Note that $0 \leq T_S \leq 1$ so that $\ln T$ always is negative. The propagation factor for μ_t is very small for light matrices and large values of Z. For large values of Z, the X-rays of element Z have a high transmission probability, which is even higher for light matrices. In the other extremity, the propagation factor for S_t is zero and for μ_t it is one. This occurs when the X-ray transmission changes rapidly with changing proton energy or depth in the sample so that for most proton energies $T_S < -T_S \ln T_S$. This case can be found for low values of Z, especially for heavy matrices.

In figures 3.1 and 3.2, there also are some steps visible for the matrices composed of Fe and Pb. These steps are caused by the absorption edges of the matrix elements. The absorption edges cause changes in the value of the X-ray attenuation coefficient and thus, via the transmission, in the propagation factor.

3.3.4 Propagation Factor for the Matrix Composition

An impression of the influence of the matrix composition can be obtained from figures 3.1 and 3.2. There are two possibilities for the error calculation. One is the calculation of the change in the yield as a function of the change in the matrix composition, according to Eq. 3.4. The other possibility is the calculation of s_{S_t}/S_t and s_{μ_t}/μ_t caused by the error in the matrix concentrations and subsequently using the propagation factor for these errors, as described in the previous subsection. The errors in S_t and μ_t are caused by the errors in S_i and μ_i of the individual elements and the errors in the concentrations of these elements. Because of facts explained in Appendix C we have chosen to use the first method of direct calculation of the change in the yield as a function of the change in the matrix composition.

For the discussion of the propagation factor, we consider a binary matrix A_cB_{1-c} to simplify the reasoning. In this case, the absolute value of the error in the concentration, s_c, is used instead of the relative error, $\frac{s_c}{c}$, because the concentration is in itself a relative variable. For this value, the smallest of the two absolute errors s_{c_A} and s_{c_B} has to be taken. This is explained by the fact that the two concentrations c_A and c_B are dependent because their sum must be one. From this dependence, it follows that the errors in c_A and c_B also depend on each other. To be able to use the absolute error, the propagation factor $P'(Y(X_Z), c) = \frac{s_{Y,c}}{Y}/s_c$ is introduced. The relation between the two propagation factors is $P'(Y(X_Z), c) = P(Y(X_Z), c)/c$. Note, that the subscript c denotes the

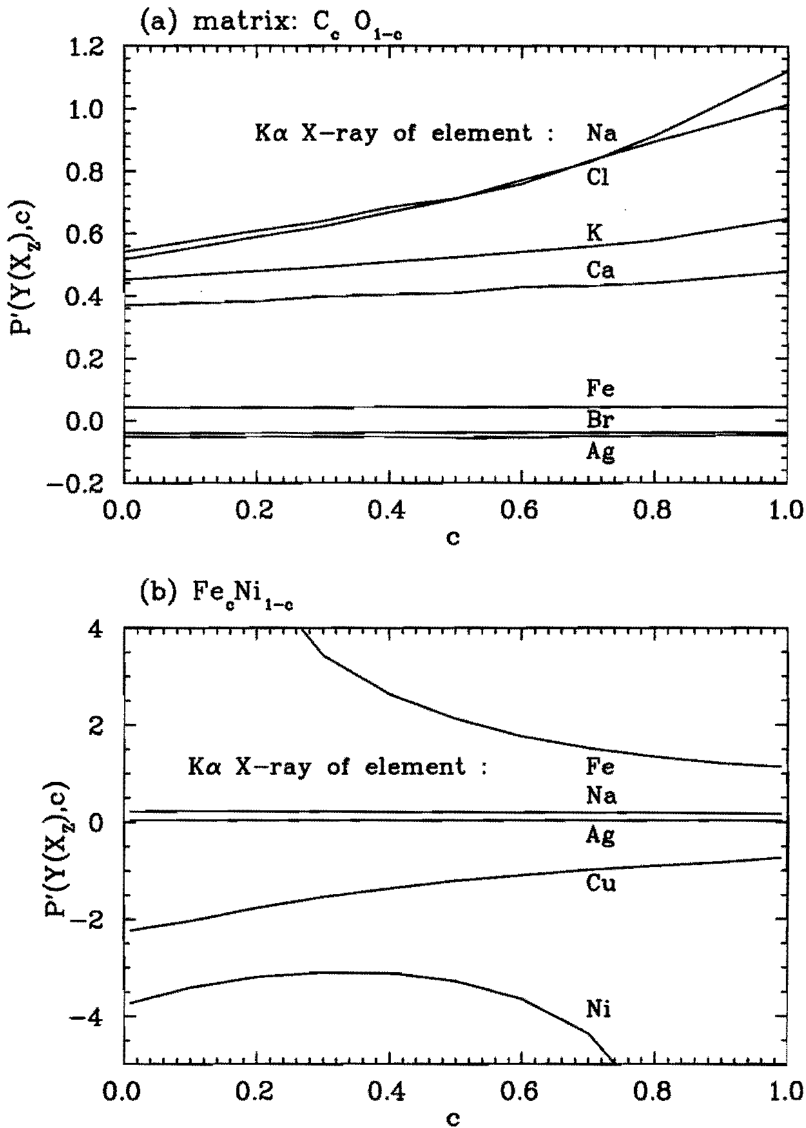

Fig. 3.3: Plot of the propagation factor to the primary yield for several elements as a function of the matrix composition for (a) a C_cO_{1-c} matrix and (b) a Fe_cNi_{1-c} matrix. The beam energy is 3 MeV. For figure (a), elements between Na and Cl have a similar behaviour. For figure (b), elements between Na and Ag, with the exception of Fe, Ni and Cu, have a matrix dependency between that of Na and Ag. A negative value means the yield decreases when the concentration c increases.

concentration of a matrix element. This quantity is different from c_Z, the concentration of the element of interest used in Eq. 2.15. For two types of matrix ,the influence of the composition has been investigated in more detail. One type is a matrix of C_cO_{1-c} (chosen because C and O are the main constituents, in mass, of biological material and backing foils) and the other is Fe_cNi_{1-c}. The propagation factor $P'(Y(X_Z), c)$ is displayed in Fig. 3.3 for X-rays of several elements. A positive value of $P'(Y(X_Z), c)$ implies that the yield increases with increasing C or Fe concentration.

From Fig. 3.3(a), it is clear that the matrix composition plays an important role for light elements (Na-Cl) in a C_cO_{1-c} matrix. The yield for the light elements increases by about a factor of 2 for the change of a 100% O matrix to a 100% C matrix. A rough estimate of this increase can be found from Fig. 3.3(a) by integrating $P'(Y(X_Z), c)$ over all concentrations c. The large increase is caused by the fact that the values of μ decrease by about a factor 2 for this change and thus the transmission probability (T_S) increases. The uncertainty in such a matrix composition thus plays an important role in the uncertainty of the yield for light elements. The stopping power of the protons increases about 6% for the change of a oxygen matrix to a carbon matrix. Accordingly the yield for the heavy elements decreases by about the same amount, resulting in a negative value for $P'(Y(X_Z), c)$. For heavy elements the change in the X-ray attenuation coefficient is of much less importance because of its low value and hence the high transmission. The uncertainty in the yield due to the matrix composition is thus of much less importance for heavy elements.

For the Fe_cNi_{1-c} matrix, the effects are less pronounced except for the yield of Fe, Ni and Cu (see Fig. 3.3(b)). For Na, the yield increase by about 23% for a change from 100% Ni to 100% Fe. This results in an average value of about 0.2 for the propagation factor $P'(Y(X_Z), c)$. The 23% increase in yield can be explained by a 19% decrease of the X-ray attenuation coefficient. For Ag, the yield increases by $\sim$ 3% for a change from 100% Ni to 100% Fe. This is the result of a 17% decrease in the X-ray attenuation coefficient, not so important because of the high transmission probability. The change in the X-ray attenuation coefficient is partly, but not completely, counterbalanced by an increase of the stopping power, less than 1% increase for 3 MeV protons and 3% for 1 MeV protons. All elements between Na and Ag have values for the propagation factor between those of Na and Ag, with the exception of Fe, Ni and Cu. The values of the propagation factor for Cu are very large because the X-ray energy of Cu is above the absorption edge of Fe while it is still below the absorption edge of Ni. This results in a much higher value of $\mu_Z(E_{X,Cu})$ for Fe than for Ni. Therefore, the yield decreases drastically when the Fe content of the sample increases, resulting in large positive values for the propagation factor for the matrix composition. The propagation factor $P'(Y(X_Z), c)$ for the matrix composition of Fe is strongly influenced by the fact that it is a matrix element. In first order, the yield is linearly

dependent on c ($c_Z = c$ for Fe). Thus $P(Y(X_{Fe}), c) \approx 1$ and $P'(Y(X_{Fe}), c) \approx 1/c$ which is in reasonable agreement with Fig. 3.3(b). It should be remembered that this discussion is only for the primary yield while for Fe there is also a SF yield. $P'(Y(X_{Ni}), c)$ is determined by the two factors mentioned above: the change in the X-ray attenuation coefficient because $E_{X_{Ni}}$ is still above the Fe absorption edge, and the linear dependence on the matrix composition, $P'(Y(X_{Ni}), c) \approx 1/(1-c)$ (in first order).

From these facts, it can be concluded that the matrix composition plays an important role in the uncertainty of the yield when it leads to drastic changes in μ_t and thus in the transmission. This is the case when the matrix elements have a low atomic number or when the X-ray energies are near to the absorption edges of matrix elements. Of course, the matrix composition also is important when the element of interest is itself a matrix element.

A last point of interest is the propagation factor to the concentration c_Z, $P'(c_Z, c) = \frac{s_{c_Z,c}}{c_Z}/s_c$. $P'(c_Z, c) = -P'(Y(X_Z), c)$ for none matrix elements. For matrix elements, however, the two propagation factors to c_Z and to Y are different. For a binary matrix A_cB_{1-c}, they can be correlated according to

$$P'(c_A, c) \approx -P'(Y(X_A), c) + 1/c \tag{3.13}$$

$$P'(c_B, c) \approx -P'(Y(X_B), c) - 1/c_B \tag{3.14}$$

with $c_B = 1 - c$. A derivation of these equations is given in Appendix C. Application of Eq. 3.13 and Eq. 3.14 results in values of $P'(c_{Fe}, c)$ that are in between those of Na and Ag and in values of $P'(c_{Ni}, c)$ that have a similar dependence on c as those of Cu but are slightly larger. Thus, for the propagation factor to the concentration, there is no longer any difference between matrix elements and other elements.

3.3.5 Influence of the Ionization Depth on the Propagation Factor

Another influence on the error in the yield of X-rays is the effect of the depth in the sample at which the ionization takes place. The depth in the sample influences on the one hand the energy of the protons and thus the cross section and on the other hand the transmission probability of the X-rays. Both the cross section and the transmission decrease with increasing depth. The ionization cross section has a maximum in the proton energy. For all elements with $Z > 12$, this maximum lies above 3 MeV. As described in Section 2.3.2, the errors in the stopping power and the cross section increase as the projectile energy decreases. In contrast with this, we assumed a constant error in the previous discussion (sections 3.3.2 and 3.3.3). Fortunately, the increase of the error is in part cancelled by the fact that the contribution to the total yield from parts of the sample at larger depths is very small. This is illustrated in Fig. 3.4. From this figure, it is clear that 99% of

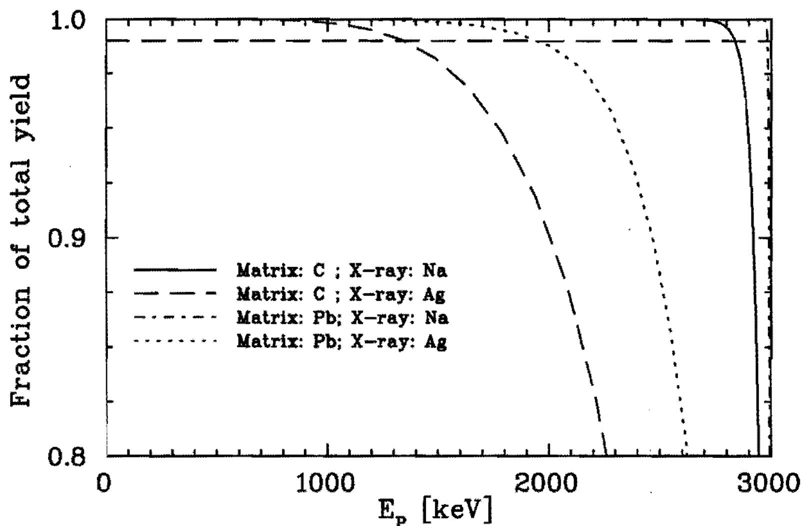

Fig. 3.4: Plot of the cumulative fraction of the yield as a function of the proton energy for two X-ray lines and two matrices. The beam energy $E_{P,0}$ is 3 MeV. The fraction is 0 at 3 MeV and 1 at 0 MeV. The dashed line represents 99% of the total yield.

the contribution to the yield comes from that part of the sample where the proton energy is larger than 1 MeV. It can also be concluded from this figure that the contribution to the yield for light elements comes from a very small top layer of the sample. This is caused by the small transmission probability of low energy X-rays.

3.3.6 Propagation Factor for the Proton Beam Energy

Finally, we consider the effect of the proton energy $E_{P,0}$ on the error in the yield. The beam energy $E_{P,0}$ is used as the starting point of the integration over E_P. For the calculation of this propagation factor, Eq. 3.4 is solved numerically. In Fig. 3.5, the propagation factor $P(Y(X_Z), E_0)$ at $E_{P,0} = 3$ MeV is shown for several matrices. The sample is assumed to be infinitely thick so that $E_{P,f} = 0$. The propagation factor is somewhat smaller than zero for light elements, meaning a decrease in yield for an increase in energy. This can be explained by the fact that the cross section for Na and Mg reaches a maximum below 3 MeV. As discussed above, only the top layer contributes to the yield (see Fig. 3.4) so the contribution to the yield of layers in the sample where the cross section has its maximum is minimal. These two facts together lead to a decrease in the yield when the projectile energy increases. For heavy elements, the propagation factor $P(Y(X_Z), E_0)$ is about 3 to 5 depending on the matrix. The error in the beam energy is in this case very important, a 2% error in the beam energy leads to a 6-10% error in the yield

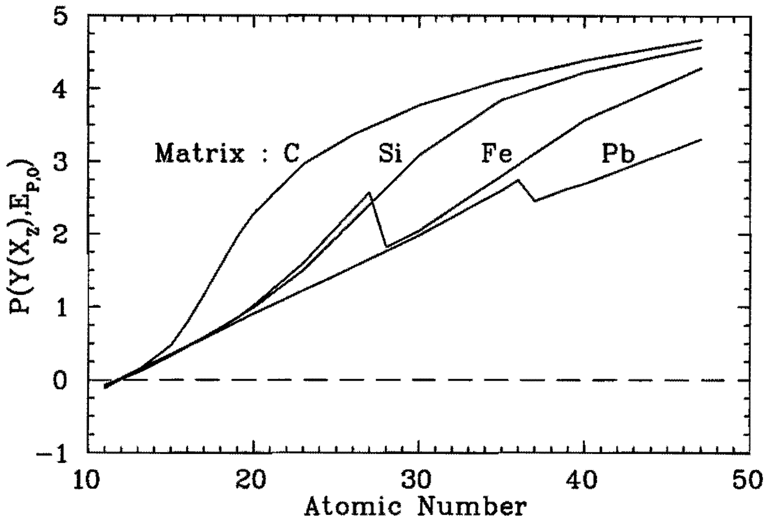

Fig. 3.5: Plot of $P(Y(X_Z), E_0)$ as a function of the atomic number of the element, for which the yield is calculated, for various matrices. The beam energy $E_{P,0}$ is 3 MeV.

for heavy elements. It can be explained by the fact that for heavy atoms the cross section increases with increasing energy, at 3 MeV by about 3% for a 1% change in energy for $Z > 40$. In Fig. 3.5, differences for various matrix compositions also are visible. Since the cross section does not depend on the matrix composition, it must be due to an X-ray transmission change. The transmission increases for heavier elements and lighter matrices. Thus, the transmission is highest for a C matrix and heavy elements. In this case, there is a larger contribution from deeper layers. In these deeper layers, at lower energies, the increase of the cross section by an increase of the energy is even larger, about 5% for a 1% change in energy at 2 MeV for $Z = 50$. The abrupt changes for the iron and lead matrices in Fig. 3.5 are again caused by changes in μ_t produced by absorption edges in the matrix material. It can be concluded that the optimum particle energy (the energy at which the yield is maximum for a given amount of material) is the energy where the cross section is maximum. For heavy elements ($Z > 21$), this maximum is not reached below 10 MeV. In a practical situation, there are of course other considerations for an optimum energy, such as the background production.

3.3.7 Conclusion

There are many quantities in the formula for the TT-PIXE yield (Eq. 2.15). For most of them, such as the number of protons N_P, the relative error in the quantity may be added quadratically to give the total error in the yield. This is not possible for the quantities in the integral. Here, the partial error in the yield for this

quantity has to be calculated first and after that this error can be added quadratically. In this section, the various propagation factors have been calculated. In combination with the error estimates of Section 2.3, this leads to the following results :

$\frac{s_\sigma}{\sigma} \approx 5\%$	$P(Y(X_Z),\sigma) \approx 1$	The partial error in the yield for the cross section is about 5%. This error can be reduced further by using external standards.
$\frac{s_{S_t}}{S_t} \approx$ 1-2%	$\lvert P(Y(X_Z),S_t) + P(Y(X_Z),\mu_t)\rvert = 1$	The partial error in the yield always is smaller than 2%.
$\frac{s_\mu}{\mu} \approx 10\%$		The partial error in the yield can be as high as 10% for low Z elements or for elements just above the absorption edges of matrix elements.
$s_{c_i} \approx$ 2-5%	$P'(Y(X_Z),c)$ varies	The relative partial error in the yield for the matrix composition can be very large when errors in the matrix composition lead to large changes in μ_t as exemplified for Ni $K\alpha$ X-rays in a Fe_xNi_{1-x} matrix.
$\frac{s_{E_{P,0}}}{E_{P,0}} \approx 1\%$	$P(Y(X_Z),E_P) \leq 5$	The partial error in the yield is in most cases below 5% for a beam energy of 3 MeV. For lower beam energies however, the partial error can increase further.

3.4 The Uncertainty in the Secondary Fluorescence Yield

3.4.1 Introduction

In this section, the uncertainty in the X-ray yield due to Secondary Fluorescence (SF), as described in Section 2.2, is discussed in detail. The SF process is rather complicated, so we make our analysis in two steps. First, we shall provide some insight in the physical meaning of the formula for SF. The aim is to understand the behaviour of SF under variation of several quantities, such as particle energy, atomic number and matrix composition. Secondly, we want to investigate the influence of uncertainites in quantities, such as the cross section, the stopping power and the X-ray absorption coefficient on the SF yield. The propagation factor is treated in the same way as in the previous section. Each quantity is discussed in a separate paragraph, with exception of the cross section since the dependence of the SF yield on the cross section is identical to that of the primary yield. The propagation factor for the cross section to the SF and primary yield

are identical :

$$\frac{s_{Y_{SF},\sigma}}{Y_{SF}(X_A,X_B)} / \frac{s_\sigma}{\sigma} \approx 1, \tag{3.15}$$

under the same assumption as made in Subsection 3.3.2. Note that the cross section for element B producing the primary X-rays, is used.

The total uncertainty in the SF yield is calculated using all the quantities in the SF yield formulas (eqs. 2.39 to 2.43):

$$\begin{aligned}\left(\frac{s_{Y_{SF}}}{Y_{SF}(X_A,X_B)}\right)^2 &= \left(\frac{s_{Y_{SF},c}}{Y_{SF}(X_A,X_B)}\right)^2 + \left(\frac{s_Q}{Q}\right)^2 \\ &+ \left(\frac{s_T}{T_{\text{abs}}(E_{X_A})}\right)^2 + \left(\frac{s_\varepsilon}{\varepsilon(E_{X_A})}\right)^2 + \left(\frac{s_\Omega}{\Omega}\right)^2 \\ &+ \left(\frac{s_b}{b_{B,X(K)}}\right)^2 + \left(\frac{s_\omega}{\omega_{B,K}}\right)^2 + \left(P(Y_{SF}(X_A,X_B),\sigma)\frac{s_\sigma}{\sigma^{ion}_{B,K}}\right)^2 \\ &+ \left(P(Y_{SF}(X_A,X_B),S_t)\frac{s_S}{S_t}\right)^2 + \left(\frac{s_b}{b_{A,X(K)}}\right)^2 + \left(\frac{s_\omega}{\omega_{A,K}}\right)^2 + \left(\frac{s_c}{c_A}\right)^2 \\ &+ \left(P(Y_{SF}(X_A,X_B),\mu_t)\frac{s_\mu}{\mu_t}\right)^2 + \left(P(Y_{SF}(X_A,X_B),E_{P,0})\frac{s_E}{E_{P,0}}\right)^2 \end{aligned} \tag{3.16}$$

The term $\frac{s_c}{c_A}$ should only be added when element A is not a matrix element, otherwise it is included in the term $\frac{s_{Y_{SF},c}}{Y_{SF}(X_A,X_B)}$. In this section, the term $\frac{s_{Y_{SF},c}}{Y_{SF}(X_A,X_B)}$ is only discussed for a binary matrix.

The total yield, including primary X-rays and SF X-rays, is given by Eq. 2.45:

$$Y(X_A) = Y_P(X_A) + \sum_{X_B} Y_{SF}(X_A,X_B) \tag{3.17}$$

Because some quantities in Y_P and Y_{SF} are the same, the uncertainties in the two cannot be simple added according to the standard error calculation rules. Instead, the formulas for Y_P and Y_{SF} have to be substituted in Eq. 3.17 and then the normal rules can be applied to obtain the uncertainty in the total yield:

$$\begin{aligned}\left(\frac{s_Y}{Y(X_A)}\right)^2 &= \left(\frac{s_{Y,c}}{Y(X_A)}\right)^2 + \left(\frac{s_c}{c_A}\right)^2 + \left(\frac{s_Q}{Q}\right)^2 \\ &+ \left(\frac{s_T}{T_{\text{abs}}(E_{X_A})}\right)^2 + \left(\frac{s_\varepsilon}{\varepsilon(E_{X_A})}\right)^2 + \left(\frac{s_\Omega}{\Omega}\right)^2 + \left(P(Y(X_A),\mu_t)\frac{s_\mu}{\mu_t}\right)^2 \\ &+ \left(\frac{s_b}{b_{A,X(K)}}\right)^2 + \left(\frac{s_\omega}{\omega_{A,K}}\right)^2 + \left(P(Y_P(X_A),\sigma)\frac{Y_P(X_A)}{Y(X_A)}\frac{s_\sigma}{\sigma^{ion}_{A,K}}\right)^2 \\ &+ \left(P(Y(X_A),S_t)\frac{s_S}{S_t}\right)^2 + \left(P(Y(X_A),E_{P,0})\frac{s_E}{E_{P,0}}\right)^2 \end{aligned}$$

$$+\sum_{X_B}\left\{\left(P(Y_{SF}(X_A,X_B),\sigma)\frac{Y_{SF}(X_A,X_B)}{Y(X_A)}\frac{s_\sigma}{\sigma^{ion}_{B,K}}\right)^2\right.$$

$$\left.+\left(\frac{Y_{SF}(X_A,X_B)}{Y(X_A)}\frac{s_b}{b_{B,X(K)}}\right)^2+\left(\frac{Y_{SF}(X_A,X_B)}{Y(X_A)}\frac{s_\omega}{\omega_{B,K}}\right)^2\right\} \qquad (3.18)$$

Notice that the error propagation factors to three different yields are used. Again, the term $\frac{s_c}{c_A}$ should only be added when element A is not a matrix element, otherwise it is included in the term $\frac{s_{Y,c}}{Y(X_A)}$.

The uncertainty in the concentration determined from Eq. 3.17 can be calculated in a similar way as for the total yield.

3.4.2 Energy Dependence of the SF Yield

The proton-beam energy $E_{P,0}$ is the initial value of the integral over E_P as can be seen from Eq. 2.39. The proton energy E_P corresponds to the depth x where the primary X-rays of element B are produced (see Fig. 2.3). The dependence of the SF yield on $E_{P,0}$ is illustrated in Fig. 3.6 for a $Pd_{0.01}Sn_{0.99}$ matrix and several proton energies. Sn is element B and Pd is element A that produces the secondary X-rays under ionization by the primary X-rays of element B. The target thickness t is assumed to be infinite. The calculated values for the SF yield are given in Table 3.1. Changing $E_{P,0}$ has two effects. On the one hand, it changes

Table 3.1: Table of the secondary yield for a $Pd_{0.01}Sn_{0.99}$ matrix as a function of energy. Sn is the element producing the primary X-rays that enhance the X-ray lines of Pd. The thickness is taken infinite.

$E_{P,0}$ MeV	$Y_{SF}(K\alpha_{Pd},K\alpha_{Sn})$ /(μC 10 mst)	$\frac{Y_{SF}(K\alpha_{Pd},K\alpha_{Sn})}{Y_P(K\alpha_{Pd})}$
1	10.51	0.267
2	446.4	0.346
3	3195	0.419
4	11443	0.491

the energy for which the cross section $\sigma^{ion}_{B,K}(E_P)$ and the stopping power $S_t(E_P)$ have to be calculated. For most elements, except elements with $Z \leq 12$, the cross section increases with increasing E_P. Thus, the SF yield increases for an increase in $E_{P,0}$. For elements with $Z \leq 12$, the cross section reaches a maximum below $E_P = 3$ MeV. The stopping power and the cross section are the only terms in Eq. 2.39 directly depending on the proton energy. The dependence of these two

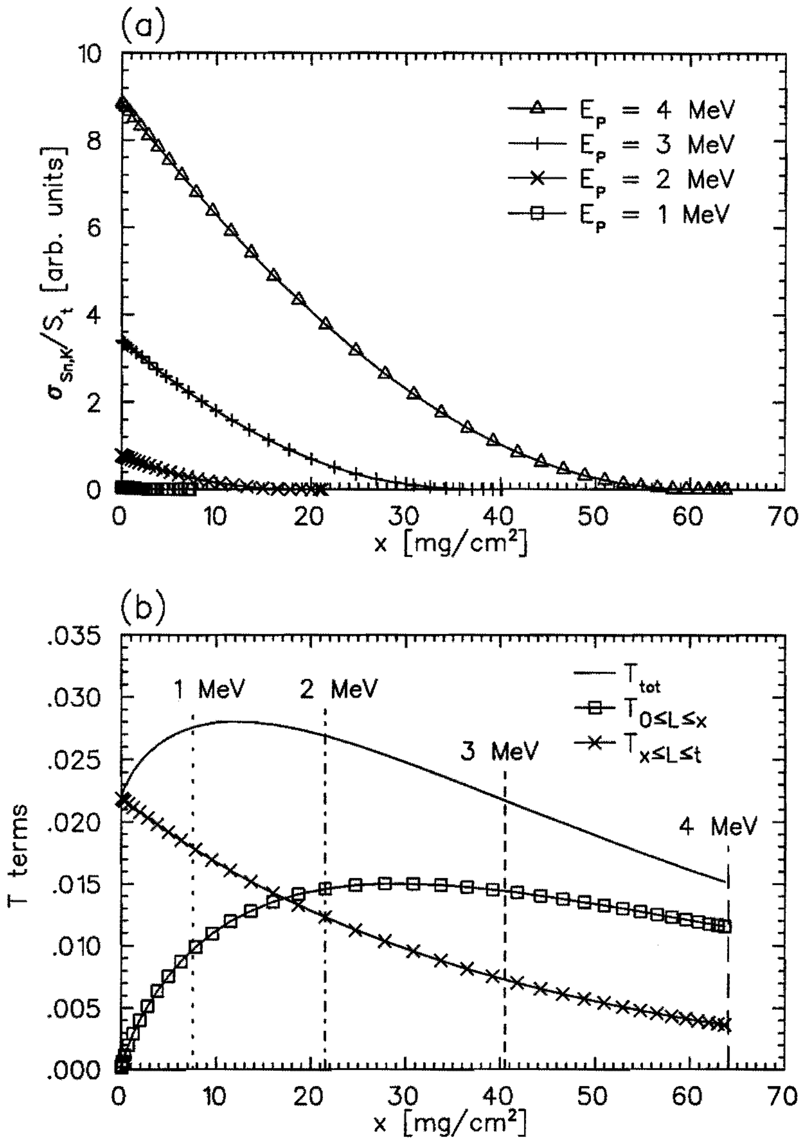

Fig. 3.6: Influence of the proton beam energy $E_{P,0}$ on the various terms of the SF yield for a $Pd_{0.01}Sn_{0.99}$ matrix. In Fig. (a), $\sigma^{ion}_{Sn,K}(E_P)/S_t(E_P)$ is given as a function of the depth x in the sample, at which the primary X-rays (of element Sn) are produced. In Fig. (b), the transmission correction terms are given as a function of x. The transmission correction terms T represent the transmission of the A and B X-rays integrated over all angles β and layers L. The range for a given $E_{P,0}$ is given by the vertical lines in fig. (b).

terms together on the proton beam energy $E_{P,0}$ is illustrated for a $Pd_{0.01}Sn_{0.99}$ matrix in Fig. 3.6(a).

On the other hand, the change in $E_{P,0}$ has no influence on the value of the two transmission correction terms in Eq. 2.39 for the same value of the depth x, although the proton energy E_P is different at the same depth x when $E_{P,0}$ changes. The change in $E_{P,0}$, however, changes the range of the protons and thus the interval of x needed for the integration. This is illustrated in Fig. 3.6(b) where the two transmission correction terms are displayed as a function of x. The curves are identical for all energies $E_{P,0}$, only the range changes.

The two transmission correction terms are given by eqs. 2.42 and 2.43. They represent the transmission of the A and B X-rays integrated over all angles β and all layers L, the layer where the secondary X-rays of element A are produced. For the transmission correction term $T_{0\leq L\leq x}$, the primary X-rays go towards the surface and subsequently produce the secondary X-rays and for $T_{x\leq L\leq t}$ the primary X-rays go deeper in the sample before producing the secondary X-rays. The transmission correction term $T_{x\leq L\leq t}(x)$ decreases monotonically with increasing x because the path lenghts increase. The other quantity, $T_{0\leq L\leq x}(x)$, has a maximum as a function of the depth x. The initial increase of the transmission correction term is caused by the increase of the amount of material between the depth x and the surface, leading to a higher integration boundery. Note that the dimension of the transmission correction terms is cm. The eventual decrease of $T_{0\leq L\leq x}(x)$ is caused by the increased path lengths. The maximum in the total transmission correction term as a function of depth x is caused by a balance of amount of material above and below the depth x and the path lenghts. The position of this maximum is determined by the X-ray transmission of X-rays of elements A and B. For heavy elements, the maximum in the two transmission correction terms together, T_{tot}, is found at larger depths since the X-ray transmission is high. This is the case for Fig. 3.6b where a $Pd_{0.01}Sn_{0.99}$ matrix is used. For lighter elements, the maximum shifts to lower depths because of a decrease in transmission. From Fig. 3.6(a) and (b), it can be concluded that the variation of the cross section dominates the variation of the SF yield when the proton beam energy varies.

Next, the propagation factor $P(Y_{SF}(K\alpha_A, K\alpha_B), E_{P,0})$ is discussed. It can be concluded from the above and Section 3.3.6 that the propagation factor to the SF yield is similar to the error propagation factor to the primary yield. This conclusion is confirmed by Fig. 3.7 where the propagation factor is plotted as a function of atomic number for several proton energies. As discussed in Section 3.3.6, the cross section has a maximum that is below 4 MeV for $Z \leq 14$. Near this maximum the cross section does not vary drastically and the propagation factor to the SF yield also is small. The propagation factor is very large for low proton energies because the cross section increases rapidly with increasing E_P, see also Fig. 3.6. Finally, it can be said that the proton beam energy must be high to reduce the influence of $E_{P,0}$.

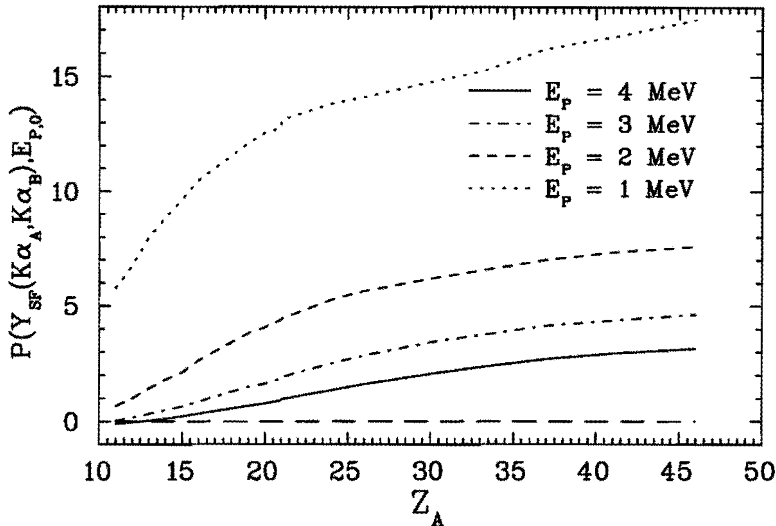

Fig. 3.7: Dependence of $P(Y_{SF}(K\alpha_A, K\alpha_B), E_{P,0})$ on the atomic number Z_A. Z_B is chosen as close as possible above the absorption edge of element A, see Fig. 3.13. $c_A = 0.01$ and $c_B = 0.99$.

3.4.3 Depth Dependence of the SF Yield

First, the contribution to the total SF yield as a function of depth is investigated. As in the previous section, the depth x is used at which the primary X-rays (of element B) are produced. For the calculation, the target thickness is taken to be infinite. For the depth x, there is a corresponding proton energy E_P. As for the primary yield, 99% of the contribution to the total SF yield comes from depths where the proton energy is larger than 1 MeV when $E_{P,0} = 3$ MeV. This is illustrated in Fig. 3.8 where the cumulative SF yield is shown as a function of proton energy for several matrices. The cumulative SF yield remains within the extremities of Fig. 3.8 when the matrix elements are between Na and Pd . The depths, where the proton energy is below 1 MeV, do not contribute significantly to the total yield because of the decrease of the ionization cross section of element B. In contrast with the primary yield, the SF yield for light elements is not strictly confined to the top layers (see Fig. 3.4).

The total sample thickness t also is a depth that may be varied. By changing the thickness t of the sample, the amount of material contributing to the SF yield can be changed without changing the proton energy E_P. In this case, the values for the proton energy E_P are constant for given x. When t changes, the integration bounderies in Eq. 2.39 are changed, resulting in different transmission correction terms. In Fig. 3.9, the transmission correction terms are shown for several thicknesses t for a $Pd_{0.01}Sn_{0.99}$ matrix at $E_{P,0} = 3$ MeV. The values of the SF yield are given in Table 3.2. The transmission correction term for layers between the top and depth x, $T_{0 \leq L \leq x}(x)$, remains identical for identical x and

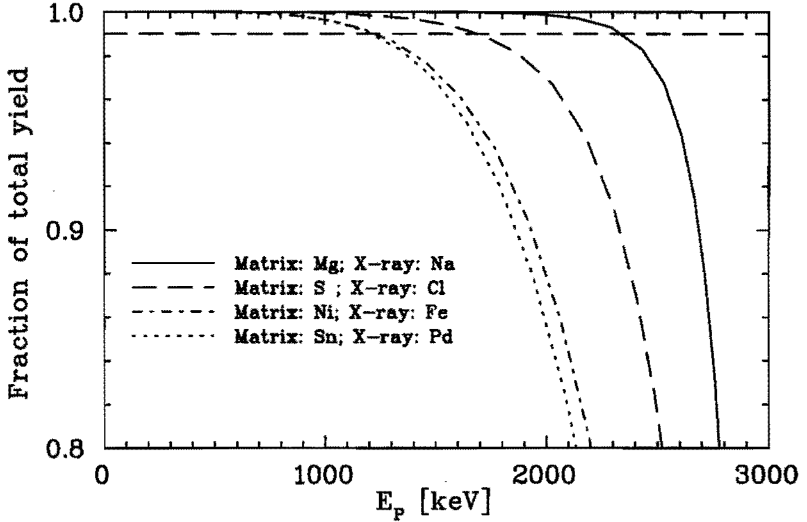

Fig. 3.8: The cumulative fraction of the SF yield as a function of the proton energy for four matrices. The mass fraction of the matrix element B is 0.99 and the mass fraction of element A is 0.01. $E_{P,0}$ = 3 MeV and the target thickness t is infinite. The dashed line represents 99% of the total SF yield.

different thickness. But the transmission correction term for deeper layers than x, $T_{x\leq L\leq t}(x)$, decreases at given depth x for decreasing sample thickness t. This effect is more pronounced for high energy X-rays. The high transmission of these X-rays makes it possible that a large fraction of the secondary X-rays produced in deep layers L in the sample can still reach the detector. To illustrate this fact, the matrix $Pd_{0.01}Sn_{0.99}$ is used in Fig. 3.9. For this matrix, the SF yield extends beyond the range of the protons. A sample thickness of 2.5× the range results in a SF yield that is 10% more than the SF yield of a sample having a thickness equal

Table 3.2: Table of the secondary yield for a $Pd_{0.01}Sn_{0.99}$ matrix as a function of thickness; $E_{P,0}$ = 3 MeV. The X-rays of Sn enhance the X-ray lines of Pd.

t mg/cm^2	$Y_{SF}(K\alpha_{Pd}, K\alpha_{Sn})$ /μC /10 mst	$\frac{Y_{SF}(K\alpha_{Pd},K\alpha_{Sn})}{Y_P(K\alpha_{Pd})}$
10	933	0.191
20	2014	0.289
30	2631	0.346
40	2889	0.379
100	3195	0.419

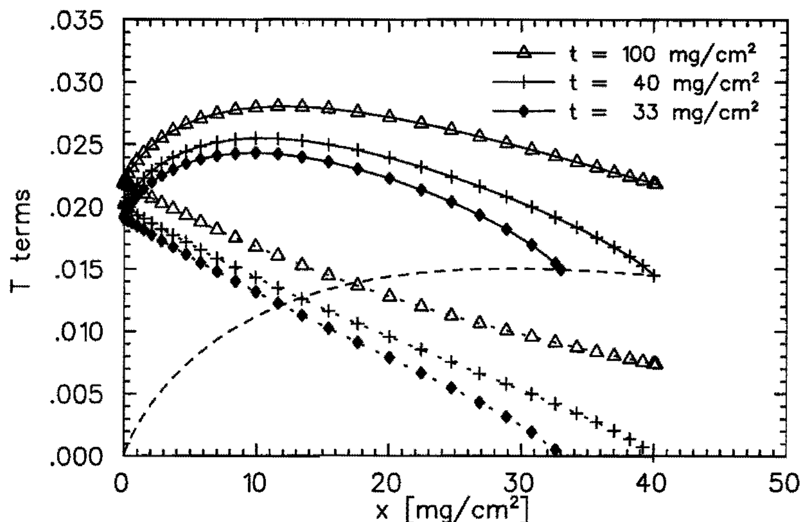

Fig. 3.9: Influence of the target thickness t on the transmission correction terms in the SF yield for a $Pd_{0.01}Sn_{0.99}$ matrix and 3 MeV protons. The dashed curve represents the term $T_{0\leq L\leq x}$, the dashed curves with symbols the term $T_{x\leq L\leq t}$ and the solid lines both terms together. The thickness $t = 40$ mg/cm^2 corresponds to the range of 3 MeV protons and $t = 33$ mg/cm^2 to an energy loss of 2 MeV.

to the range.

3.4.4 Concentration Dependence of the SF Yield

Another point of interest is the variation of the concentrations of the two elements A and B. These two concentrations are related because the total mass fraction is one. The effect of the variation of the concentrations on the yield is illustrated with a two element sample A_cNi_{1-c}, where A is Ca, V or Fe. Ni then is the element B that produces the primary X-rays which in turn can ionize element A. The SF yield for these matrices is given as a function of the concentration, c_A, in Fig. 3.10. In first order, the SF yield depends on the concentration as $c \times (1 - c)$, see eqs. 2.39, 2.40 and 2.41.

In full, the concentrations also influence the total stopping power S_t and the total X-ray attenuation coefficient μ_t. For the Fe_cNi_{1-c} matrix, this leads to an asymmetric dependence with a shift of the maximum SF yield to lower Fe concentrations. This is caused by the fact that the energy of the Ni X-rays is larger than the K-shell electron binding energy of Fe. Therefore, the attenuation coefficient $\mu_Z(E_{X_{Ni}})$ is much larger for Z = Fe than for Z = Ni. This results in a much larger absorption of Ni X-rays in a sample with high Fe concentration. This, in turn, leads to lower values for the transmission correction terms (eqs. 2.42 and 2.43) and so to a lower SF yield. For a Ca_cNi_{1-c} matrix, the SF yield is much more symmetric. This is explained by two reasons. First, the difference between the Ni

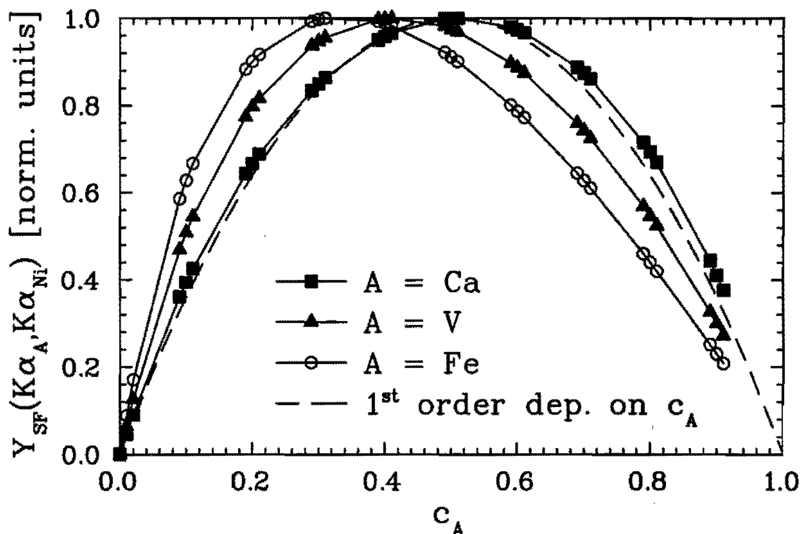

Fig. 3.10: Dependence of the secondary fluorescence yield on c_A for several elements A for a binary matrix with Ni as the element (B) which produces the primary X-rays. The beam energy is 3 MeV and the target thickness is 100 mg/cm^2. The curves are normalized to their maximum values.

X-ray energy and the K-shell electron binding energy is much larger for Ca than for Fe. This reduces the difference in transmission of Ni X-rays in a Ni dominated matrix and in a Ca dominated matrix, compared with the case of Fe. Secondly, the reduction in transmission of Ni X-rays is counterbalanced by an increase in transmission of Ca X-rays when c_{Ca} increases. This last effect is more pronounced for Ca than for Fe. The concentration dependence for a V_cNi_{1-c} matrix is between these two extremes.

For the discussion of the propagation factor for the concentration, we also consider a binary matrix to simplify the reasoning. The propagation factor for several A_cNi_{1-c} matrices is calculated and displayed in Fig. 3.11. In this figure, the absolute value of the error in the concentration is used for the same reason as explained in Section 3.3.4. Thus, $\frac{s_Y}{Y_{SF}} = |P'(Y_{SF}(K\alpha_A, K\alpha_B), c_A)| s_{c_x}$ where s_{c_x} is min (s_{c_A}, s_{c_B}). Using the first order dependence of the yield on the concentration ($Y_{SF} \sim c_A \times (1 - c_A)$), it is possible to calculate the error propagation factor:

$$P'(Y_{SF}(K\alpha_A, K\alpha_B), c_A) = \frac{s_{Y_{SF},c_A}}{Y_{SF}(K\alpha_A, K\alpha_B)} / s_{c_A} \approx \frac{(1 - 2c_A)}{c_A(1 - c_A)} \tag{3.19}$$

This equation is used to calculate the first order dependence on c_A in Fig. 3.11. It can be concluded that the propagation factor is smallest when both concentrations are more or less the same. In this case, the SF yield also reaches a maximum (see Fig. 3.10). Note that

$$P(Y_{SF}(K\alpha_A, K\alpha_B), c_A) = c_A \; P'(Y_{SF}(K\alpha_A, K\alpha_B), c_A) \approx 1 - \frac{c_A}{1 - c_A} \tag{3.20}$$

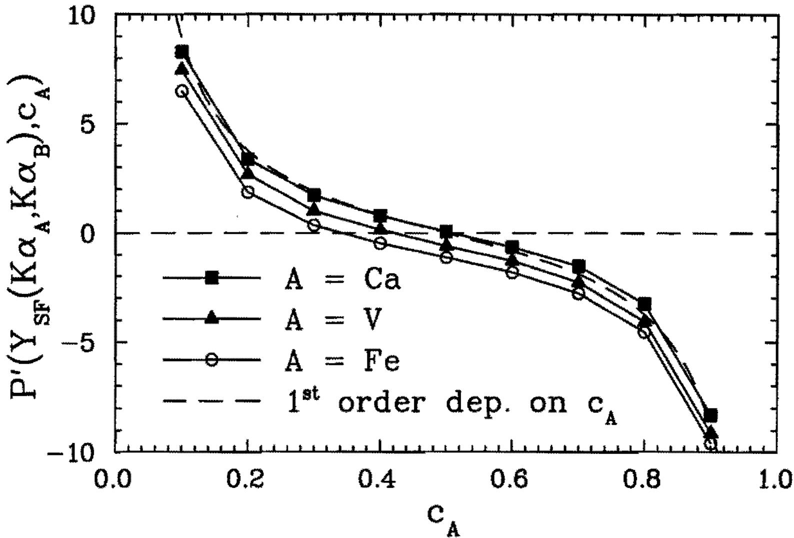

Fig. 3.11: The propagation factor for the concentration c_A. The results are displayed for three binary matrices with Ni as element B. The beam energy is 3 MeV and the target thickness is 100 mg/cm^2. The dashed line represents the first order dependence of the error propagation factor according to Eq. 3.19.

Form Eq. 3.20 it is clear that the relative error in the SF yield is always smaller than or equal to the relative error in c_A, provided that $c_A \leq 2/3$.

For small values of the concentration c_A, below a few percent, Eq. 3.20 can be simplified further. In this region, the influence of c_A on S_t and μ_t can be neglected and so the error in c_A can be ignored for the error estimate. The SF yield then depends linearly on c_A and the propagation factor according to Eq. 3.4 becomes:

$$P(Y_{SF}(K\alpha_A, K\alpha_B), c_A) = \frac{s_{Y_{SF},c_A}}{Y_{SF}(K\alpha_A, K\alpha_B)} / \frac{s_{c_A}}{c_A} \approx 1. \tag{3.21}$$

3.4.5 Atomic Number Dependence of the SF Yield

A further quantity to be investigated is the atomic number Z. A simple case is the variation of Z_A while keeping Z_B the same. Element B produces the primary X-rays under proton bombardment which, in turn, produce the secondary X-rays of element A. This case is demonstrated in Fig. 3.12 for a $A_{0.01}$ $Ni_{0.99}$ matrix with the Z_A ranging from 20 to 26. In this case only the mass absorbtion coefficient for element A, $\mu_t(E_{X_A})$, and f_A (Eq. 2.40), containing the production cross section for X-rays of element A by X-rays of element B, are changed. The $\mu_t(E_{X_B})$ is hardly effected by the change of element A since element A constitutes only a small part of the total sample. The transmission of X-rays of element A increases for higher Z_A values and so does the term f_A which contains $\tau_{A,tot}(E_{X_B})$, $\omega_{A,K}$, both increasing with increasing Z_A, and $b_{A,K}$, $(1 - \frac{1}{r_{A,K}})$, both terms slightly

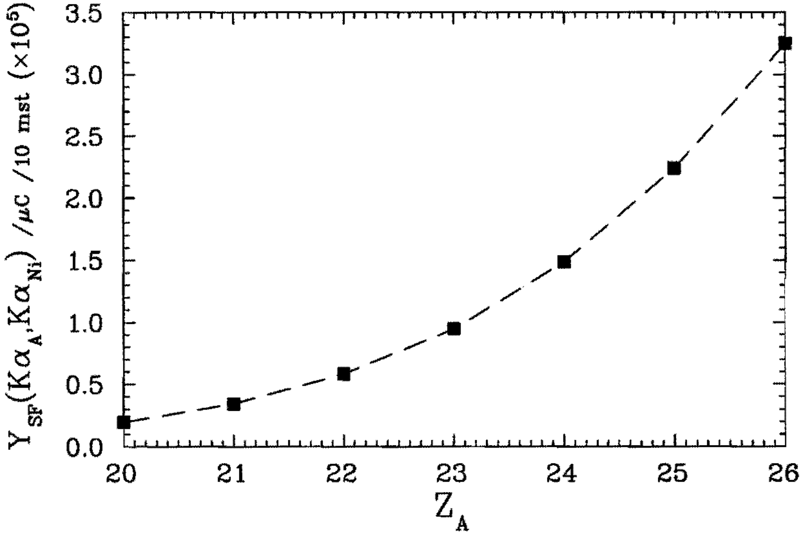

Fig. 3.12: Secondary yield as function of Z_A and for Ni as element B. $E_{P,0} = 3.0$ MeV, $c_A = 0.01$ and $c_{Ni} = 0.99$.

decreasing with increasing Z_A. The result is an increasing secondary yield as displayed in Fig. 3.12.

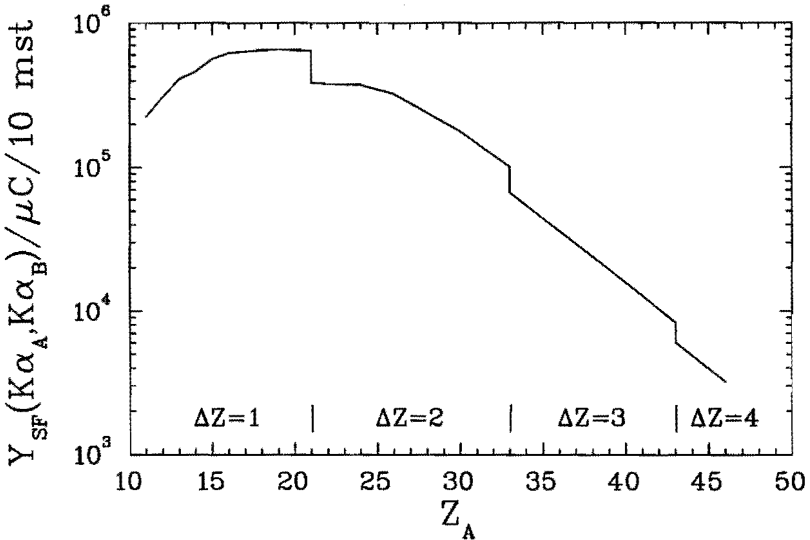

Fig. 3.13: Secondary yield as function of Z_A with Z_B as close above Z_A as possible (see text). The difference ΔZ between Z_A and Z_B is given in the figure. $E_{P,0} =$ 3 MeV, $c_A = 0.01$ and $c_B = 0.99$.

A more complicated case is the variation of Z of both elements. The Z value of element B is chosen in such a way that the Kα X-ray of this element is as close as possible above the K-shell absorption edge of the element A. This results in a

maximum secondary yield for a specified element A. The dependence of this SF yield as a function of the atomic number of element A is displayed in Fig. 3.13. From this figure, it can be seen that the yield has a maximum at around $Z_A = 18$. This maximum originates from a complexity of factors. The ionization cross section for element B decreases drastically with increasing Z. Also, $\tau_{A,tot}(E_{X_B})$ decreases with increasing Z. This effect is counterbalanced by the increase with increasing Z of the fluorescence yields of elements A and B and the two transmission correction terms. The steps in Fig. 3.13 at $Z_A = 21$, 33 and 43 are caused by a step in Z_B resulting in a step in $\tau_{A,tot}(E_{X_B})$.

3.4.6 Propagation Factor for the Stopping Power and the X-ray Attenuation Coefficient

The propagation factors for these two variables are calculated according to Eq. 3.4. The same assumptions as formulated in Section 3.3.3 have also to be made. Although the formulas for the secondary yield (eqs. 2.39, 2.40, 2.41, 2.42 and 2.43) are more complicated than for the primary yield, the resulting propagation factors for the stopping power and the X-ray attenuation coefficient look much the same. Examples for several matrices are given in Fig. 3.14 for $E_{P,0} = 3$ MeV. The dependence of the SF yield on the stopping power $S_t(E_P)$ is identical as for the primary yield (Eq. 2.41). The dependence of the SF yield on the X-ray attenuation coefficient is more complicated since there are more quantities: $\mu_t(E_{X_A})$, $\mu_t(E_{X_B})$

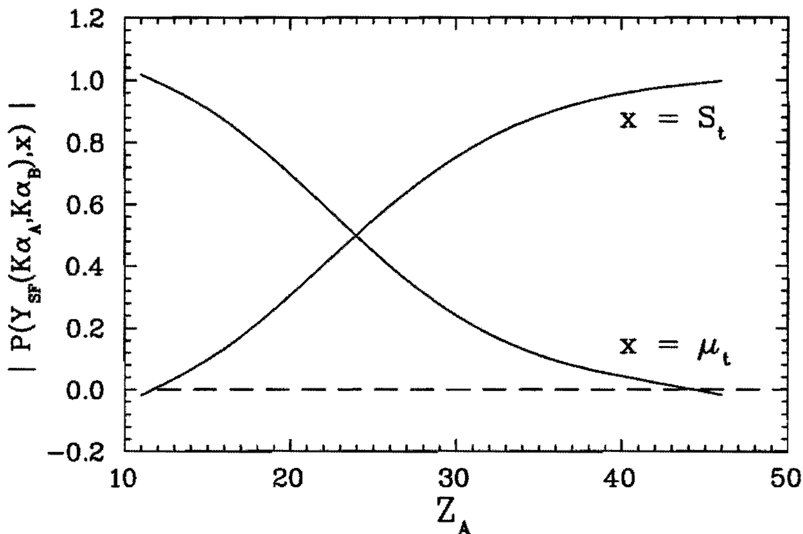

Fig. 3.14: The propagation factor for the stopping power and the X-ray attenuation coefficient as a function of Z_A with Z_B as close as possible above Z_A (see fig. 14). $E_{P,0} = 3$ MeV,$c_A = 0.01$ and $c_B = 0.99$.

and $\tau_{A,tot}(E_{X_B})$. Also, $r_{A,K}$ is dependent on the X-ray attenuation coefficient but, since it is a fraction, equal errors counterbalance each other. Most errors in μ cancel out. What remains is an exponential term, just as for the primary yield. In this case, this may lead to an underestimation of the importance of the X-ray attenuation coefficient. This is caused by the fact that $\tau_{A,tot}(E_{X_B})$, the photo-electric absorption coefficient (see Eq. 2.9), is a quantity in the numerator (see Eq. 2.40) while $\mu_t(E_{X_A})$ is a quantity in the denominator (see Eq. 2.42 and Eq. 2.43). In our error assessment, the uncertainties in these two quantities cancel each other. In practice, the two uncertainties may enhance each other because the X-ray attenuation coefficients are needed for different sides of the absorption edge of element A and around absorption edges the uncertainty in the X-ray attenuation coefficient is largest (see Section 2.3.6). Although no direct information is available about the deviations of the values of the X-ray attenuation coefficients around absorption edges, the comparison of different databases can give some clues. The comparison done in Fig. 2.7 shows that variations of tens of percents are possible over absorption edges.

The propagation factor $P(Y_{SF}(X_A, X_B), \mu_t) \approx 1$ for light elements because the X-ray transmission is small and it decreases to zero for heavier elements when the X-ray transmission increases. The dependence on Z_A of $P(Y_{SF}(X_A, X_B), S_t)$ is just opposite. The sum of both propagation factors equals one, all in agreement with the propagation factor to the primary yield.

3.4.7 Conclusion

In this section, we have discussed the propagation factors for the various quantities to the SF yield. These error propagation factors can be combined with the error estimates of Section 2.3 to arrive at the partial errors in the SF yield for these quantities. This leads to the following results:

$\frac{s_\sigma}{\sigma} \approx 5\%$ $\quad P(Y_{SF}(X_A, X_B), \sigma) \approx 1$
The partial error in the yield for the cross section is about 5%. This error can be reduced further by using external standards.

$\frac{s_{S_t}}{S_t} \approx 1-2\%$ $\quad |P(Y_{SF}(X_A, X_B), S_t) + P(Y_{SF}(X_A, X_B), \mu_t)| \approx 1$
The partial error in the yield for the stopping power always is smaller than 2%.

$\frac{s_\mu}{\mu} \approx 10\%$
The partial error in the yield for the X-ray attenuation coefficient can be as high as 10% for low Z elements.

$s_{c_A} \approx$ 2-5% $\quad P'(Y_{SF}(X_A, X_B), c_A) \approx \frac{(1-2c_A)}{c_A(1-c_A)}$
in first order approximation for a binary matrix.

The error in the matrix composition is an experimental error. For a two element matrix both concentrations can be calculated with PIXE. The error in the smallest concentration, usually element A, determines the partial error in the yield. This last error is thus determined by the precision of the PIXE measurements, including SF correction, but it is smaller than or equal to the relative error in c_A for $c_A < \frac{2}{3}$.

$\frac{s_{E_{P,0}}}{E_{P,0}} \approx 1\%$ $\quad P(Y_{SF}(X_A, X_B), E_{P,0}) \approx 0 - 15$

The partial error in the yield for the proton beam energy is in most cases below 4%, for beam energies of 3 MeV and higher. For lower beam energies the partial error can increase drastically.

3.5 Conclusions

In this chapter, the dependence of the uncertainty in the calculated yield on the uncertainty of various quantities is investigated for the primary PIXE yield and the SF yield. To be able to undertake this study, we have derived a formula (Eq. 3.4) that makes it possible to calculate numerically the influence of the uncertainty in quantity x on the uncertainty in the yield. We have introduced the propagation factor $P_Z(Y, x) = \frac{s_{Y,x}}{Y} / \frac{s_x}{x}$. This quantity makes it possible to say something about the influence of the uncertainty in x without actually knowing how large the uncertainty in x really is. A complex dependence on the matrix composition and on the proton and X-ray energies is found for the propagation factors of some quantities. The results of the investigation for the primary yield are summarized in Section 3.3.7 and the results for the SF yield are summarized in Section 3.4.7. Several interesting features have been found: The propagation factors for the stopping power and the X-ray attenuation coefficient are found to be interrelated and their sum must equal unity. This is derived mathematically for the primary yield and it is also found via numerical calculations for the SF yield. The uncertainty in the matrix composition plays an important role in the uncertainty in the primary yield for light elements ($11 < Z < 17$) in even lighter matrices (e.g. a C_cO_{1-c} matrix). In general, it is important when changes in matrix composition lead to large changes in the X-ray attenuation coefficient, i.e. for Cu and Ni X-rays in a Fe_cNi_{1-c} matrix. The propagation factor $P_Z(Y, E_{P,0})$ can be very large (up to 5 for $E_{P,0} = 3$ MeV) for large values of Z, becoming larger when the matrix becomes lighter and $E_{P,0}$ becomes smaller. This dependence is found for the primary as well as for the SF yield. The uncertainty in the yield due to the uncertainty in the various quantities can undergo large changes when the matrix composition or the proton energy is varied. To get an accurate error estimate it is therefore necessary to make a separate evaluation for every type of sample and element of interest.

4 Experimental Setup

The experimental PIXE setup is described in this chapter. The emphasis is placed on the measurements of the experimental quantities needed for the absolute calibration. The quantities determined are the beam energy $E_{P,0}$, the absorber thicknesses, the detector solid angle Ω, and the detector efficiency $\varepsilon(E_{X_Z})$. New aspects are the methods used for the beam-energy determination and the calculation of the uncertainties in the detector efficiency and the absorber transmission.

4.1 General description

All experiments described in this thesis have been performed with the PIXE setup of the Eindhoven University of Technology (E.U.T.). In recent years, this setup has been modernized in the scope of this study. In this section, the new setup is described with its features. In the rest of this chapter, the values of the experimental quantities needed for the absolute calibration method are determined. The treatments of the subjects in this chapter are of different lengths because some subjects are already treated extensively in literature whereas other discussions yield more new information, such as the beam energy calibration for a cyclotron. The aim of the modernization is to create a user-friendly and versatile setup, suitable for the measurement of a variety of samples, especially thick ones.

The source of the ion beam is the AVF (Azimuthal Varying Field) cyclotron of the E.U.T., suitable for the acceleration of protons, deuterons, ^{3}He, and alpha-particles with energies in the range of 2.8-26 MeV. After extraction, the beam passes through a Beam Guidance System (BGS). The beam transport has been calculated by P.H.A. Mutsaers [1]. Settings for the quadrupoles have been calculated in such a way that the particle beam is divergent in the last segment of the BGS. The layout of the last segment of the BGS is given in Fig. 4.1. In this last segment, the beam passes through four diaphragms, three of which have a diameter of 12 mm. The diameter of the last one is selectable without breaking the vacuum; the possibilities are 4, 8, or 12 mm. The diaphragms together with the divergence of the beam insure a reasonably uniform beam. A remotely controlled quartz plate can be moved into the beam line to view the shape and intensity of the beam. This enables a fast optimalization of the settings of the dipoles and quadrupoles of the BGS and a qualitative check on the beam uniformity. To obtain a better beam uniformity, a diffuser foil can be inserted without breaking the vacuum. For more information about beam uniformity, see [Joh 88] and for more information about diffuser foils, see [Kiv 80, Coe 90]. A fifth diaphragm of 12 mm in diameter

[1] Private communication

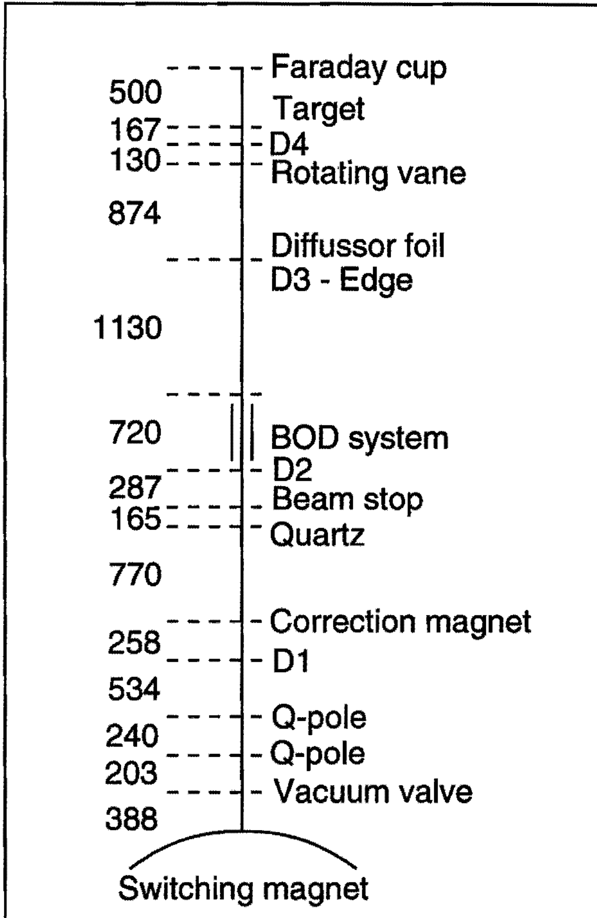

Fig. 4.1: Schematic layout of the last beam line segment.

is included in the chamber to remove ions scattered on the diaphragms upstream in the beam line. Other elements in this beam line are the deflection plates for the Beam On Demand (BOD) system, described in Section 4.4, and a rotating vane, described in Section 4.3.

The PIXE chamber is evacuated by a 170 l Turbo Molecular Pump (TMP) preceded by a rotation pump. All the vacuum equipment is controlled by PLC (Programmable Logic Control) to insure the safe operation of the equipment. Up to 80 samples can be contained in a modified slide projector that is also PLC controlled. Other equipment in the chamber are a Faraday cup (FC, see Section 4.3), an electron gun (EG), an absorber holder with absorbers (see Section 4.5), an X-ray detector (see Section 4.6), and a particle detector (PD, see Section 4.7). The electron gun is used to prevent charge build-up on thick insulating samples. The charge build-up results in a high Bremsstrahlung background in the X-ray spec-

trum. This process is described by Kivits [Kiv 80] who ascribed the background in the spectrum to the Bremsstrahlung between voltage breakdowns. The time of the breakdown itself is too short to explain the background. There are several methods to prevent charge build-up that work equally well altough each method has its own drawbacks [Goc 83]. We have chosen to install an electron gun, in view of its ease of use and flexibility. The design is according to ref. [Ahl 75].

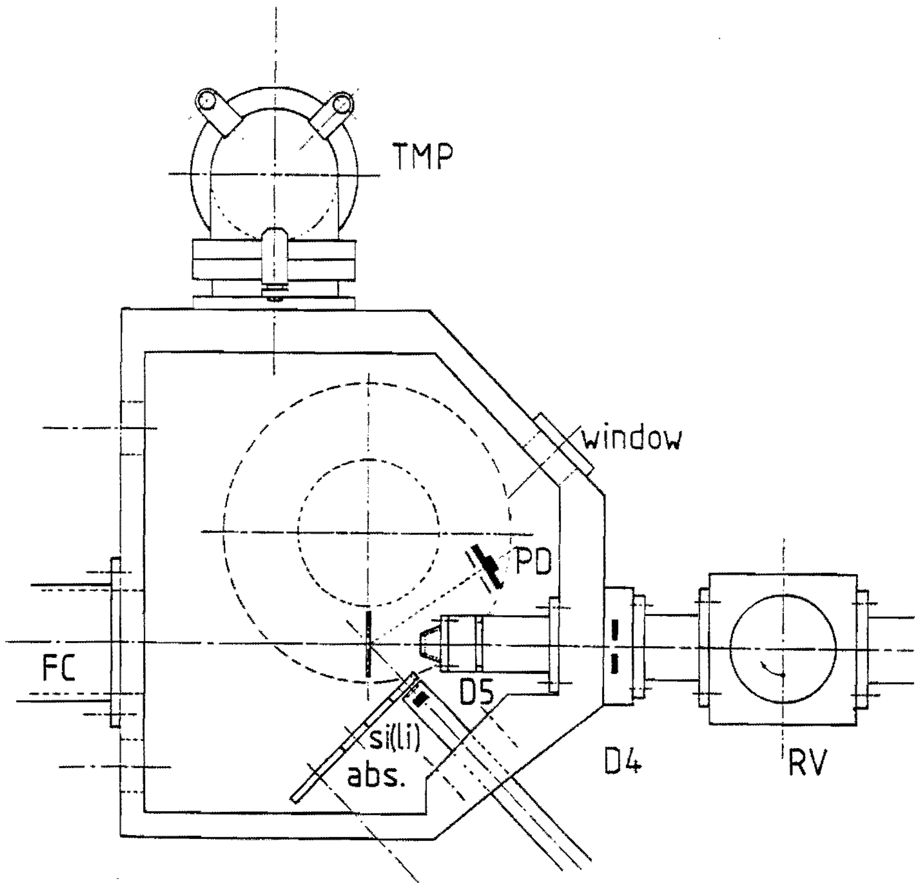

Fig. 4.2: Layout of the PIXE chamber. The abbreviations are: FC - Faraday cup, abs - absorber holder with absorbers, Si(Li) - Si(Li) X-ray detector, D4 and D5 - diaphragms, RV - Rotating Vane, PD - Particle Detector, TMP - Turbo Molecular Pump. The electron gun, not depicted, is situated under diaphragm D5. The two dashed circles give the outline of the slide caroussel.

Apart from the sections describing the equipment in the beam-line and the setup, other sections are devoted to the beam-energy calibration (Section 4.2), and to the data analysis, including the NBS analysis (Section 4.7). In the final

section (Section 4.8), conclusions and a summary of the results obtained in this chapter are presented.

4.2 Beam energy calibration[2]

Two new methods for the determination of the beam energy are described. Since these are rather new methods, the discussion is extensive in comparison with other subjects. The beam energy thus determined is found to be 70 keV lower then the nominal value.

4.2.1 Introduction

The beam energy is an important quantity for the PIXE analysis, as is shown in Section 3.3.6. In many cases, the error propagation (defined in Section 3.3.1) is larger than 1, so even a small uncertainty in the value of the beam energy can have a large effect on the uncertainty in the calculated concentration. A limiting factor on the accuracy with which the beam energy is known, is the energy spread of the beam. For a cyclotron, this energy spread is worse than for a linear accelerator, such as a Van de Graaff accelerator. For our cyclotron , the energy profile is a near Gaussian one, with a standard deviation of about 0.3% for a proton energy of around 3 MeV [3]. There are several methods to measure the beam energy, but some are less suited for a cyclotron because these methods need many different beam energies and energy adjustement with a cyclotron is a cumbersome procedure. In this section, two methods are described, each in a seperate subsection, for the beam energy determination between 3 and 4 MeV. The final subsection (4.2.4) is devoted to a discussion and conclusions.

4.2.2 Measurements using elastic and inelastic scattering of protons

In general, if one can measure the energy of a scattered proton from a known target, it is easy to calculate the proton beam energy E_1. However, there is no way to calibrate the spectrum of scattered protons and thus to measure the energy of scattered protons directly because there are no proton sources available for the calibration of the detector. Alpha sources are available but cannot be used because the response of the detector to alpha particles is different from that to protons, leading to a different calibration. It is, however, possible to determine the energy of the incoming protons E_1 by combining elastic and inelastic scattering.

At certain angles, the energies of the elastically and inelastically scattered protons are equal. If these angles are measured and the reaction Q value for the

[2]This section is based on an article by N. Uzunov, F. Munnik and M.J.A. de Voigt [Uzu 93].

[3]Private communication H.L. Hagedoorn

inelastic scattering is known, the proton beam energy E_1 can be determined. The energy E_1 is calculated from first principles [Uzu 93] according to

$$E_1 = \frac{M_I(M_I + m_P)Q}{m_P^2 A(\theta_I, \theta_E) - M_I^2} \tag{4.1}$$

where

$$A(\theta_I, \theta_E) = \left\{ \left(\frac{m_P + M_I}{m_P + M_E} \right) \left(\cos\theta_E + \sqrt{\frac{M_E^2}{m_P^2} - \sin^2\theta_E} \right) - \cos\theta_I \right\}^2 + \sin^2\theta_I \tag{4.2}$$

Here, M_E and M_I are the masses of the target atoms for the cases of elastic and inelastic scattering, respectively; θ_I and θ_E are the angles of the detector at which the inelastic and elastic scattered protons have equal energies and m_P is the proton mass.

The energy E_1 can even be determined using only one element with an appropriate excited state. In certain cases, the angles θ_I and θ_E can be identical. This results in a more simplified method than described above and is called the 'cross-over' method [Hey 63, Smy 64].

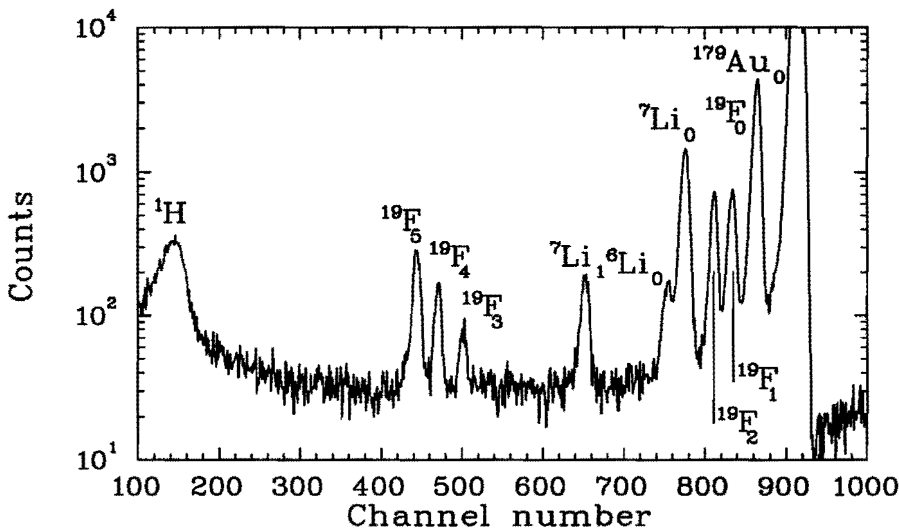

Fig. 4.3: Proton scattering spectrum of the LiF target bombarded with 3.5 MeV protons (nominal value). The angle of the detector is 65° . The backing of the target is a thin Au layer. The notation of the symbols is described in the text.

For this method, we have used a conventional scattering-spectrometry setup. The detector is a Passivated Implanted Planar Silicon Detector (PIPS) Canberra PD100-12-500AM with a resolution of 15 keV. A target consisting of a LiF layer

(0.189 mg/cm^2) evaporated onto a gold backing (0.523 mg/cm^2) is used. ^{7}Li and ^{19}F are a very suitable combination for the experiments using elastic and inelastic scattering because of their high cross sections for the (p,p') reaction. The nominal beam energy of the cyclotron is set to 3.5 MeV. The measurements are made at forward scattering angles between 40° and 90° .

A typical proton spectrum from the scattering experiment is shown in Fig. 4.3. In this spectrum, we observe the peaks corresponding to elastically scattered protons from lithium, fluorine and gold, denoted by Li_0, F_0 and Au_0. The symbol $^{19}F_1$ denotes the reaction ^{19}F(p,p')^{19}F leading to the excited state at 110 keV, $^{19}F_2$ - the reaction ^{19}F(p,p')^{19}F with Q=197 keV and $^7Li_1$ denotes the reaction ^{7}Li(p,p')^{7}Li with Q=478 keV. Another group of three closely situated peaks and a broadened peak are observed in the low energy region of the scattering spectra (Fig. 4.3). It is found that the three peaks are due to the reactions [Pol 69]: ^{19}F(p,p')^{19}F at an excitation energy of 1.346 MeV denoted according the indications above as $^{19}F_3$; ^{19}F(p,p')^{19}F at 1.459 MeV denoted as $^{19}F_4$ and ^{19}F(p,p')^{19}F at 1.554 MeV denoted as $^{19}F_5$. The broadened peak is due to the elastic scattering from hydrogen (^{1}H), which is also present in the target. Fig. 4.4 shows a plot of the positions of the different proton peaks versus the angle between 40° and 90° .

For the calculation of the beam energy according to Eq. 4.1, we used the curves for $^7Li_0$ and $^{19}F_2$, $^{19}F_0$ and $^{19}F_1$, $^{19}F_0$ and $^{19}F_2$ and from the second set of peaks the curves for H and $^{19}F_3$, H and $^{19}F_4$, H and $^{19}F_5$. First, a least squares fit is applied to the elastic and inelastic scattering data to determine the angles θ_I and θ_E. Secondly, a correction of +0.3° for the angle of the unscattered beam is made. This correction is experimentally determined using the small angle elastic scattering of the protons from the gold backing at ± 16° , ± 18° and ± 20° . A plot is made of the Au_0 peakarea, normalized to the beam charge, versus the angular position of the detector. The angle of the unscattered proton beam can

Table 4.1: The calculated proton beam energy for different lines. The nominal beam energy is 3.5 MeV.

Lines used for calibration	θ_E (deg.)	θ_I (deg.)	Calculated beam energy (MeV)
$^7Li_0$,$^{19}F_2$	65.02	88.57	3.42±0.03
$^{19}F_0$,$^{19}F_1$	88.75	69.97	3.45±0.03
$^{19}F_0$,$^{19}F_2$	88.75	53.21	3.43±0.06
H,$^{19}F_3$	42.29	71.67	3.430±0.016
H,$^{19}F_4$	42.29	44.60	3.436±0.014
H,$^{19}F_5$	45.06	65.31	3.428±0.018

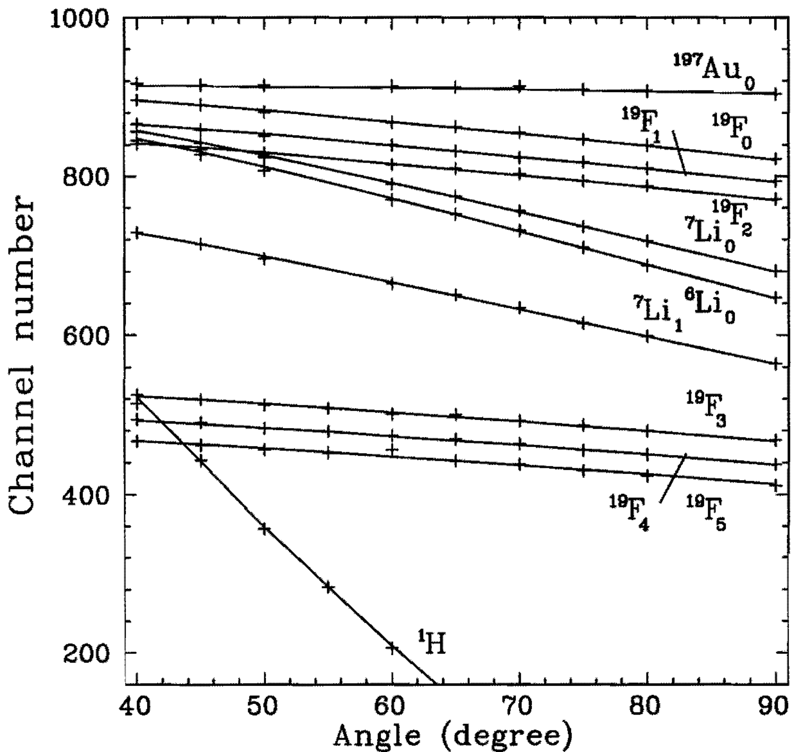

Fig. 4.4: Plot of the measured peak positions of several elements as a function of the scattering angle θ. The drawn lines are fitted lines using standard kinematics calculation [Chu 78]. The notation of the symbols is explained in the text.

be found by taking the average centre of the two curves at negative and positive angles. Thirdly, corrections for the energy loss of the protons in the target have to be made using the stopping power for the sample. The so found values for the beam energy are given in Table 4.1. From this table, it is seen that the nominal energy of the cyclotron proton beam is about 70 keV too high.

The uncertainties in Table 4.1 are determined from individual uncertainties according to standard error calculations (see Section 3.2). The main uncertainties in our experiment are the statistical uncertainties in the fitted data, in the determination of the positions of the peaks, in the stopping power (about 3%, see Section 2.3.2) and in locating the detector angles (about 0.08°). It should be noted that the beam energy spread (about 10 keV) and the detector resolution influence the uncertainty in the determination of the peak position by peak broadening. The peak broadening caused by the thickness of the sample ranges from a few to 20 keV. This broadening is so small because all the particles have to travel through the complete sample, whether scattered at the front or at the back of the

sample. The sample is rotated for larger scattering angles to minimize the difference in energy loss between protons scattered at different depths in the sample. The only peak for which the broadening is much larger, is the peak of hydrogen. Here, the broadening is caused by the fact that the stopping power of scattered and not scattered protons is very different because the energy of the scattered protons is much lower than the beam energy. Nevertheless, the uncertainty for the case of scattering from hydrogen and the three groups $^{19}F_3$, $^{19}F_4$ and $^{19}F_5$ is less than for the other cases, which is due to the smaller statistical error in the least squares fit.

4.2.3 Measurements using (p,α) reactions

Reactions of the type (p,α) can be used to determine the proton beam energy using the same experimental setup and sample as used for Subsection 4.2.2 and an alpha source for the energy calibration of the detector.

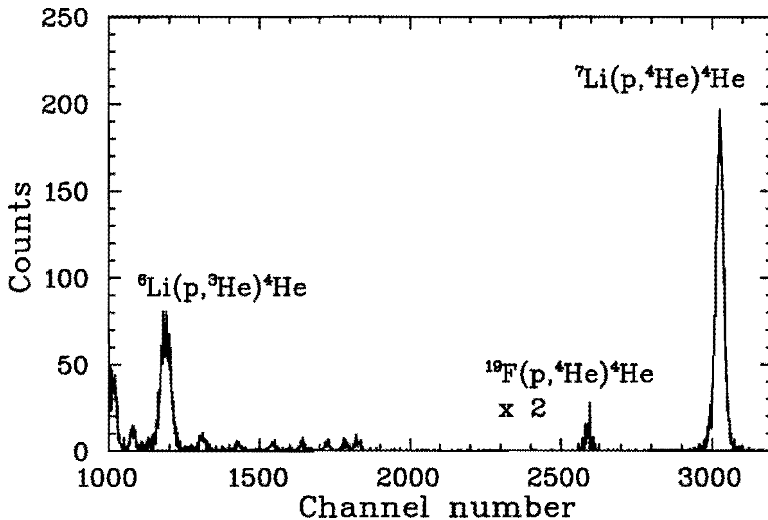

Fig. 4.5: High energy part of the (p,α) spectrum of the LiF target. The detector angle is 70° and the nominal proton beam energy is 3.5 MeV. The number of counts of the $^{19}F_3$ peak is multiplied by a factor of two to make it better visible.

Three peaks are observed in the high-energy region of the spectra from the scattering experiment described in the previous subsection (Fig. 4.5). They are due to the alpha particles from the reaction $^{19}F(p,^4He)^{16}O$ with ground-state Q-value of 8.110 MeV [Squ 56]; to alpha particles from the reaction $^7Li(p,^4He)^4He$ with ground-state Q-value of 17.347 MeV and to ^3He particles from $^6Li(p,^3He)^4He$ with ground-state Q-value of 4.021 MeV [Lau 66]. The alpha particles from the reaction $^6Li(p,^3He)^4He$ appear in the region of the elastically scattered protons because of the low kinematical factor and the peak is therefore difficult to observe

for some angles. Moreover, the detector calibration made for alpha particles could not be used for the ^{3}He because the different masses for ^{3}He and ^{4}He result in different detector responses. The peak from the reaction ^{19}F(p,^{4}He)^{16}O is also omitted since it had a low alpha yield. The analysis has been carried out only for the ground state alpha particle group from the ^{7}Li(p,^{4}He)^{4}He reaction.

The PIPS detector is calibrated using a standard Am/Cm alpha source with energies of 5.486 MeV and 5.805 MeV for the main alpha lines. The resolution of the detector is 20 keV at 5.486 MeV. For a given angle of the detector position, the energy of the alpha particle peak can be measured. The energy of the incoming protons can be calculated from these energies using standard calculation of the kinematics [Chu 78] after corrections for the energy losses of the protons and the alpha particles in the target material. The angle of the target is rotated for larger scattering angles to minimize the energy loss of the particles. The results for the calculated beam energy are given in Table 4.2. To calculate the proton beam energy from the reaction, we have used a program for simulation and evaluation of nuclear reactions, SENRAS V2.11 [Viz 90].

Table 4.2: Table of the calculated beam energy using the ^{7}Li(p,α)^{4}He reaction for several angles. The calculation is described in Section 4.2.3. The nominal beam energy is 3.5 MeV.

Detector angle (deg.)	Rotation of the target (deg.)	Energy of the α group (MeV)	Beam energy (MeV)
50.3	0	11.851	3.44±0.03
55.3	23	11.661	3.44±0.03
60.3	35	11.427	3.45±0.03
65.3	35	11.154	3.46±0.03

The uncertainty in the energy of the proton beam determined from the alpha particles of the reaction ^{7}Li(p,^{4}He)^{4}He is due to the uncertainties in the determination of the position of the alpha peaks. Because the energy of the alpha particles produced by the reaction ^{7}Li(p,^{4}He)^{4}He is much larger than the energy of the alpha particles from the Am/Cm source, a large extrapolation of the energy calibration is needed. Therefore, these results are only an example of this method and cannot be used on their own account.

4.2.4 Discussion and conclusions

Two methods for the energy determination of the proton beam in the range between 3 and 4 MeV have been applied: energy determination from experiments with elastic and inelastic proton scattering and from (p,α) reactions. The reliabil-

ity of the results varies from method to method and it is assessed below.

The scattering method used in Subsection 4.2.2 is an extension of the so-called 'cross-over' technique and provides a very convenient way of determining the energy of the proton beam. From the error analysis made for the measurements with the LiF target, it follows that the uncertainties in determining the proton beam energy are less than 18 keV in the case of the inelastic groups of lines $^{19}F_3$, $^{19}F_4$ and $^{19}F_5$ and the elastic group for H. The only external data needed are the Q-values for the inelastic scatterings, which are accurately known.

From a point of view of the time needed for the experiments, the method using (p,α) reactions, described in Subsection 4.2.3, is favourable. However, the energies of the alpha particles from the reaction ^{7}Li(p,^{4}He)^{4}He are much larger than the energies of the calibration source. The use of this method can only be justifiably when both energies are more closely matched. The external data needed for this method are the Q-values for the (p,α) reactions and the energy of the alpha particles emitted by the alpha-source. More than anything else, the results of Subsection 4.2.3 in combination with the results of Subsection 4.2.2 prove that the energy calibration of the particle detector is very linear as is expected of this type of detector [Kno 79].

On the basis of the above arguments, we have decided to use the results of the second method (Subsection 4.2.2) as the best estimate of the proton beam energy. The results of Table 4.1 lead to an averaged systematic shift of 70 ± 10 keV below the nominal value of AVF cyclotron for the investigated energy range.

4.3 Measurement of the number of bombarding particles

The accurate measurement of the number of bombarding ions is vital for the calculation of the concentration of elements in the sample (see Section 2.1). In this section, two methods for the measurement of the number of bombarding particles are described.

There are several ways to determine the number of ions passing through the sample [Joh 88, Chapter 3] and [Hol 72, Sta 86]. The choice of the method also depends on the type of sample to be analyzed. The main criterium for this choice of measurement is the thickness of the samples compared to the range of the ions. Three types of samples can be discerned: i - thin samples, that is the thickness is small compared to the ion range, ii - thick samples, the ion beam is stopped in the sample and iii - samples of intermediate thickness. The conduction of the sample can also play a role in the choice of the method. Our specifications for the beam current measurement are: The integrated beam current has to be measured for thin, thick and intermediate thick samples alike. The current to be measured ranges from 10 pA to 100 nA. We have chosen two systems to answer

the specifications: (1) A device using a rotating vane for the measurement of the beam current for thick and intermediate thick samples. (2) A Faraday cup for the measurement of the beam current for thin samples and for the calibration of the rotating vane measurement.

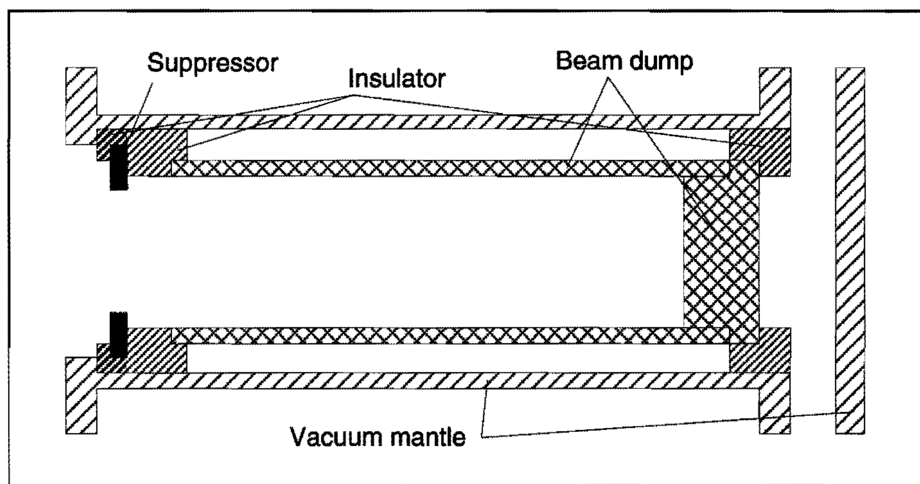

Fig. 4.6: Design of the Faraday cup used in the PIXE setup.

The design of the Faraday cup is given in Fig. 4.6. Particular emphasis has been put on preventing secondary and tertiary currents from escaping the Faraday cup. Such currents are e.g. backscattered beam particles and electrons freed in the beam dump or in the sample. The transport of electrons in and out the Faraday cup can be limited by applying a negative voltage on the suppressor ring in front of the Faraday cup. The effect of the suppressor was tested by measuring the yield per unit charge for a thin Ni layer evaporated on a polycarbonate foil as a function of the suppressor voltage. No effect was found for voltages between zero and -1000 V. The beam charge measured with the Faraday cup is digitized with a standard Ortec digitizer (model 439) for beam currents larger than 0.5 nA. The resulting pulses are then counted with a scaler. For lower currents, a Keithley K617 is used to measure the total charge. Leakage currents measured with this device are typically between -1 and +1 pA.

For intemediate thick samples, an extra problem is caused by multiple scattering. If the angular spread caused by multiple scattering exceeds 5.4°, some of the ions do not enter the Faraday cup. Using multiple scattering theory [Nig 59], it can be calculated for which thickness 98% of the scattered particles enters the Faraday cup. The thicknesses for a Al, Cu or Au sample leading to a 2% error in the charge measurement, are respectively 6.5 mg/cm^2, 3.8 mg/cm^2 and 1.9 mg/cm^2. The thicknesses are upper values since the dimension of the beamspot on the

sample is not taken into account. For thicker samples, the ratio of charge in the Faraday cup versus total charge decreases. As an example, the charge has been measured using both the Faraday cup and the rotating vane device for two samples. From the measurements, a ratio of 67% was found for a 9.8 mg/cm^2 thick Cu foil and 84% for a 5.9 mg/cm^2 Fe foil. Calculations using the multiple scattering theory yield 69% and 90% respectively, in reasonable agreement with experiment.

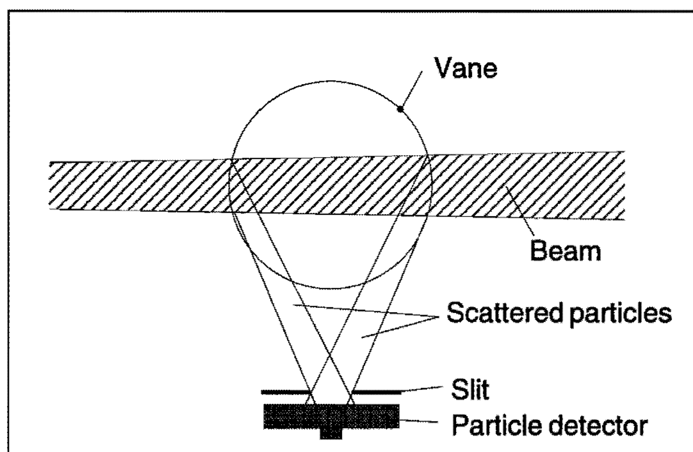

Fig. 4.7: Layout of the rotating vane device as used for the measurement of the number of particles in the beam.

The layout of the device using the rotating vane is given in Fig. 4.7. The rotating vane itself is made of tungsten that has a high Rutherford backscattering cross section. The vane rotates with a frequency of about 3-4 Hz. The part of the beam intercepted by the vane is only 0.32%, thus hardly influencing the passing beam. The scattered particles are detected at an angle of 90° where the cross section is relatively high compared to more backward angles. A part of the measured particles is selected with a Single Channel Analyzer (SCA). The rotating vane makes the monitoring of beam currents down to 20 pA possible because it produces a high counting-rate. A disadvantage is its position at some distance from the sample with a diaphragm in between. This makes the device sensitive to changes in the beam position, angle and divergence. Periodic calibrations with the Faraday cup are therefore required. It is, however, not possible to place the diaphragm before the rotating vane since it will have a negative effect on the use of the diffussor foil. The main uncertainty in this type of measurement is caused by the counting statistics. The beam fluctuations are another source of error. The total uncertainty ranges from less than 1% to 5% depending on the charge and the stability of the cyclotron.

4.4 The Beam-On-Demand System

A new state-of-the-art system for the prevention of pile-up is described.

Pile-up occurs when two X-rays enter the detector in such a short time interval that they are processed as a single event. The resulting pulse has a height somewhere between the height of a single pulse and the height of both pulses together. In the spectrum, this results in a continuum beyond an X-ray peak followed by a sum peak (see Fig. 4.8). The energy of the pile-up depends on the time interval between the X-rays entering the detector. If this interval is very short compared to the shaping time of the main amplifier, the energy of the pile-up is the sum of the individual energies; if this interval is longer, the energy corresponds to the continuum between the single and sum peaks. Pile-up makes it more difficult to fit the spectrum and it can obscure weaker X-ray lines of other elements.

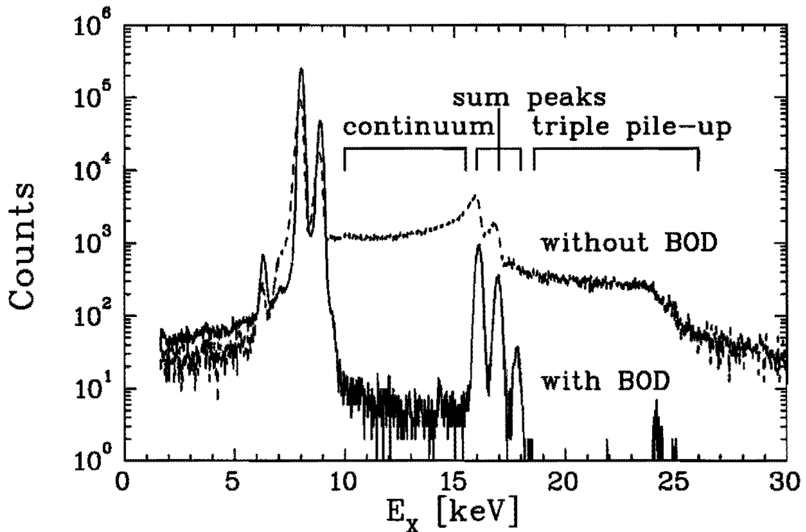

Fig. 4.8: Spectra of a Cu sample, with and without the BOD system. The spectra are normalized on the same charge; for the spectrum without BOD system this is the charge corrected for dead time. The reduction of the twofold pile-up in the BOD spectrum is 28.

There are two methods to reduce the pile-up [Joh 88]. We have chosen the Beam-On-Demand (BOD) system for this purpose. The use of a BOD system also eliminates the correction for dead time. Dead time is the processing time of the measurement system. Part of the X-rays entering the detector during the processing time results in pile-up (see above) and part is not processed and is therefore not found in the spectrum. The idea of a BOD system is not new [Jak 72] but progress in the development of electronics has made improvements in the system possible [Zen 87]. The design of the new system is given in Fig. 4.9

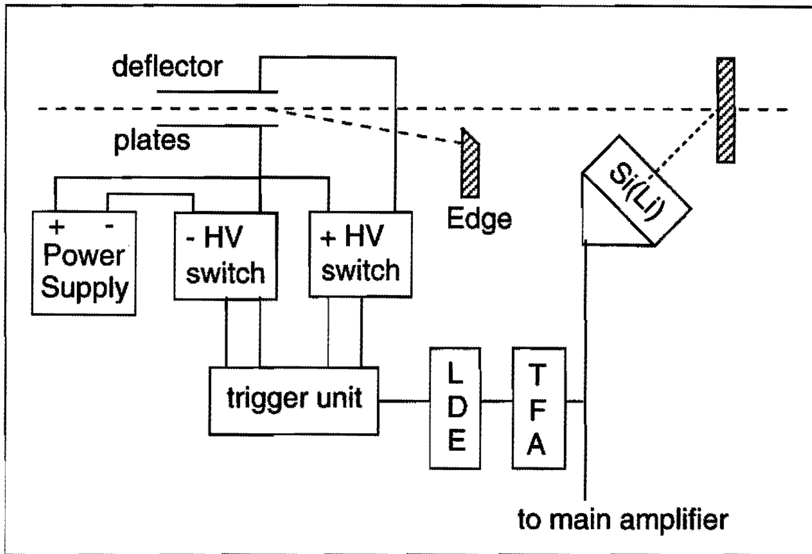

Fig. 4.9: Layout of the beam-on-demand system used for the prevention of pile-up in the X-ray spectrum. Here, TFA stands for timing filter amplifier, LDA stands for leading edge discriminator, and HV stands for high voltage.

and in an internal report [Cre 91].

An electrostatic field between two plates is used to deflect the beam. The ion beam reaches the target when the plates are grounded. To deflect the beam, both plates are given an equal, but opposite voltage. In this way, only half of the voltage has to be applied compared with the old situation where one plate is grounded and the other is charged. Futhermore, the low voltages allow the use of faster switching semi-conductor electronics, whereas previously capacitors where used. When an X-ray enters the detector, a pulse is generated by the preamplifier. To trigger the BOD system, this signal is transformed into a logic pulse by a fast amplifier (a timing filter amplifier, model Ortec 474) and a leading edge discriminator (Ortec 584). With a gate and delay generator (Phillips 794), the time width of this pulse is increased to match the processing time of the measuring system. This signal is used to trigger the high voltage (HV) switches, which connect the deflection plates with the HV power supply. The heart of the HV switches are two mosfets (Metal Oxide Semiconductor Field Effect Transistor) with a maximum switching voltage of 1000 V. This and the geometry of the system limits its use to proton beams with a maximum energy of 3 MeV. The maximum energy can be increased when improved mosfets become available, able to switch higher voltages, or by the use of a cascade of mosfets. To reduce power consumption, the mosfets are operated periodically with a frequency of 25 kHz. This frequency is sufficiently large to reduce the voltage leakage from the plates to several Volts on a operating voltage

of 800 V. The periodic triggers for the HV switch are produced in a separate trigger unit. The electronic system is described in an internal report [Tin 91].

The system is placed rather far from the sample (1200 mm) but that was unavoidable since it would otherwise interfere with the operation of the diffussor foil (see Fig. 4.1). The long distance between the BOD system and the sample increases the reaction time but it still is not the most dominating factor. The reaction time of the BOD system is the time between the absorption of an X-ray in the detector and the completion of the switch to beam off target. Several components contribute to this reaction time: (i) The time needed for the generation of a pulse in the detector and the amplification in the preamplifier. The collection time for a 3 mm thick detector at 77 K is of the order of 100 ns. This value is estimated on the speed of electrons and holes in Si [Ott 75]. (ii) The time needed to generate a logic pulse of the correct length; it is 250 ns. (iii) The time used by the trigger unit and the HV switches; it is 100 ns. (iv) The time of flight of 3 MeV protons to the target; it is 125 ns. At the moment, the pulse discrimination is the limiting factor resulting in an overall reaction time of minimal 575 ns. Because a cyclotron is used, the ion beam has a pulse structure. For our cyclotron and 3 MeV protons, the period of the bunches is 136 ns. Therefore, at least four more bunches will reach the target after an X-ray has been absorbed in the detector and before the beam is switched off. Without BOD system, around 230 bunches can contribute to pile-up.

4.5 The Use and Calibration of Absorbers

The analysis can be optimized by the use of a specific absorber in front of the detector. The application of an absorber introduces an extra quantity in the quantitative analysis (see Eq. 2.8). The absorbers and the measurement of their thickness are discussed. A new aspect is the uncertainty calculation for the transmission through the absorbers.

An absorber in front of the detector is used to optimize the experimental conditions. In its simplest and commonly used form, it is a thin foil or disk of a single light element. Its use results in a reduction of the low energy X-rays. Since the background is highest at low energy, the use of an absorber reduces the overall counting-rate, thereby resulting in less dead time and/or enabling the beam current to be increased.

In front of the detector, a rotatable wheel is positioned containing up to five absorbers. For standard use, a thin Be and two thick C absorbers are included. The Be absorber is thick enough to stop most backscattered protons. Only 3 MeV protons backscattered on heavy atoms have enough energy to enter the detector but the energy left after passing the absorber is small. The Be absorber is still thin enough to measure all but the lightest elements like Na and Mg. The carbon

absorbers can be used for the measurement of high-energy X-rays (above about 6 keV).

The thickness of the absorbers can be determined with several methods. The easiest method is weighing the absorber and measuring its area. Other methods use either X-ray sources or samples bombarded by protons. These two methods have the advantage that the absorber is measured in the same way as it is used, i.e. the thickness is measured through the X-ray absorption in the absorber and, therefore, systematic errors cancel each other out. This is especially important for absorbers containing contaminants. These contaminants may have very little effect on the total mass of the absober and still have a large effect on the total X-ray absorption coefficient for the absorber because the elemental X-ray absorption coefficients are very different. If the precise concentrations of the contaminants are not known, the use of the absorber thickness, as found by weighing and measuring its area, results in larger errors than the use of the thickness found by transmission measurements. The exception is for X-ray energies where the transmission is very low ($T < 0.01$). The measurements using X-ray sources can be normalized on time, while the measurements using a proton beam have to be normalized on charge, which is not as precise. Also, the absorberless measurements with the proton beam introduce additional uncertainties because of the backscattered protons. Therefore, the measurements with X-ray sources are preferred when possible.

From the number of counts measured with and without the absorber, the thickness can be determined according to Eq. 2.7. For the measurements, a ^{55}Fe source emitting Mn K X-rays is used. If the ratio of the number of counts with and without absorber is near to one, small errors in this ratio can lead to large errors in the determined mass thickness of the absorber. Because this is the case for the Mn K X-rays emitted by the source and the Be absorber, the thickness determination of the Be absorber is supplemented by PIXE measurements of an Al sample with and without absorber [Win 91]. The following results have been obtained: for the Be absorber: $\rho t = 9.8 \pm 0.6$ mg/cm^2, the first C absorber: $\rho t = 250 \pm 6$ mg/cm^2 and the second C absorber: $\rho t = 360 \pm 7$ mg/cm^2. In the rest of this work, the first C absorber is called C250 and the second C360.

For PIXE experiments, these thicknesses are used to calculate the transmission for the X-rays of interest. The uncertainty in the transmission, resulting from the uncertainty in the thickness of the absorber, varies greatly with X-ray energy. Also, the uncertainty in the X-ray absorption coefficient influences the uncertainty in the transmission. The uncertainties in the thicknesses of the absorbers and the uncertainties in the X-ray absorption coefficients are not independent because the latter are used to obtain the former values. Nevertheless, for use in the error calculation, it is assumed that the quantities are independent. This is justified when the X-ray energy for which the transmission is calculated, differs greatly from the X-ray energy for which the calibration is done. In other cases, the uncertainties

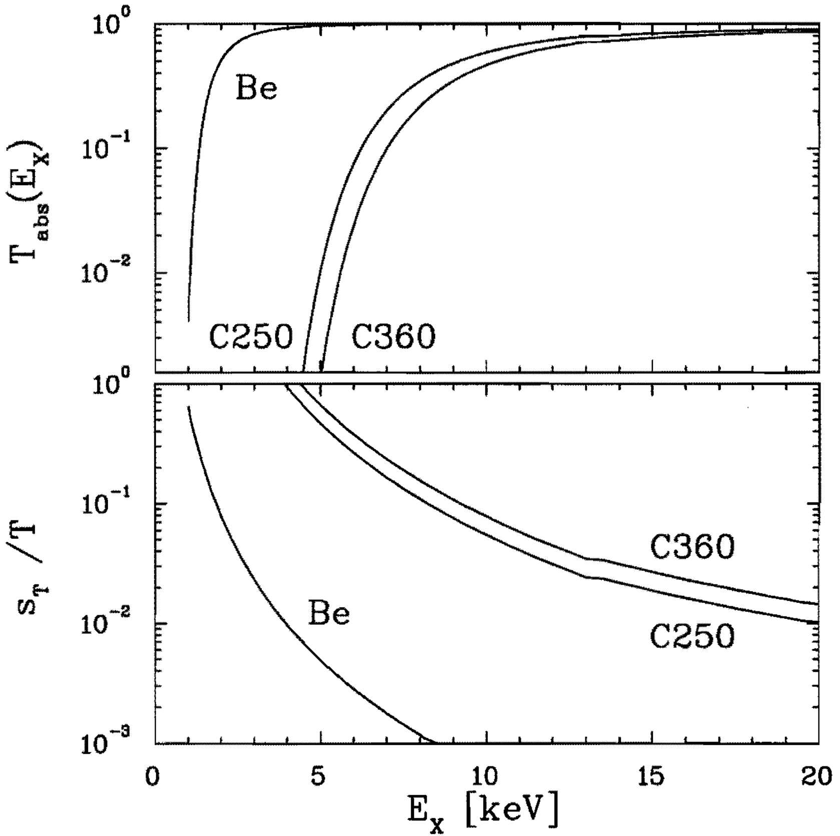

Fig. 4.10: Transmission and uncertainty in the transmission for the various absorbers as functions of energy. Here, Be stands for the Be absorber and C250 and C360 for the two C absorbers with different thicknesses.

stated below are maximum values. The uncertainty in the transmission can be calculated as:

$$s_T^2 = \left(\frac{\partial T}{\partial(\rho t)} s_{\rho t}\right)^2 + \left(\frac{\partial T}{\partial(\mu/\rho)} s_{\mu/\rho}\right)^2 \tag{4.3}$$

with s_T, $s_{\rho t}$ and $s_{\mu/\rho}$ the uncertainties in the transmission, the mass thickness and the mass absorption coefficient, respectively. The relative uncertainty in the transmission is then

$$\frac{s_T}{T} = -\ln(T)\sqrt{(\frac{s_{\rho t}}{\rho t})^2 + (\frac{s_{\mu/\rho}}{\mu/\rho})^2} \tag{4.4}$$

For Be and C, there are no absorption edges in the X-ray energy region of interest so the uncertainty $\frac{s_{\mu/\rho}}{\mu/\rho}$ is estimated to be 10% for all X-ray energies(see Section 2.3.6). In Fig. 4.10, the transmission curve and the uncertainty for the transmission

are given as a function of X-ray energy for all three absorbers. From this figure, it can be concluded that the absorbers should not be used for the measurement of elements that have a transmission of less then 0.3 since the uncertainty for lower X-ray energies is too large (> 10%).

4.6 Detector Calibration

A geometrical method for the determination of the detector solid angle is described. The detector efficiency $\varepsilon(E_{X_Z})$ is established for all X-ray energies of interest (1-40 keV). The quantities needed for the calculation of $\varepsilon(E_{X_Z})$ are determined.

The detector solid angle

A geometrical method is used to determine the solid angle. The solid angle can be found by determining the crystal surface area A_{det} and the distance r between sample and the average interaction depth of the X-rays in the crystal: $\Omega = A_{\text{det}}/r^2$.

The problems in determining the distance r are the localization of the crystal behind the window, which is only approximately known, and the average penetration depth of the X-rays in the crystal. The total distance r, however, can be determined by measuring the yield of an X-ray source at two different positions and the distance d between these positions [Win 91]. One distance is the normal distance r between detector and sample and the other distance is $r + d$. Then, r can be calculated from the ratio of the yields at these positions and the distance d:

$$r = d\left(1 + \sqrt{\frac{Y_r}{Y_{r+d}}}\right) / \left(\frac{Y_r}{Y_{r+d}} - 1\right) \tag{4.5}$$

with Y_r the X-ray yield at position r and Y_{r+d} the yield at position $r + d$. Both yields have to be normalized on the measuring time. Using this formula for a number of distances and a ^{55}Fe source, r is found: $r = 50.4 \pm 0.4$ mm for Mn K-α X-rays emitted by a ^{55}Fe source. The average penetration depth for Mn K-α X-rays is 29 μm (calculated according to [Han 73]). The average penetration depth is a function of the X-ray energy but for energies up to 14 keV, the distance r remains within the estimated uncertainty. For higher X-ray energies, the average penetration depth increases asymptotically to half the crystal thickness of 3 mm. The solid angle can therefore vary by about 6% for low- and high-energy X-rays.

Next, the detector surface area can also be determined with an X-ray source [Cam 84a, Kor 92]. The source, a ^{55}Fe source, is collimated with two diaphragms with a diameter of 1 mm. One diaphragm is situated close in front of the source, the other close to the detector. Diaphragms and source are mounted on a traversable table. With this apparatus, horizontal and vertical scans of the detector have been

made. From these scans, the surface dimensions of the crystal are determined: vertical width $= 5.68 \pm 0.09$ mm; horizontal width $= 5.22 \pm 0.12$ mm. Since these widths are not equal, the surface area is calculated under the assumption that the surface shape can be approximated by an ellipsoid: $A_{\text{det}} = 23.3 \pm 0.8$ mm^2. This yields a solid angle of $\Omega = 9.2 \pm 0.3$ msr for Mn K-α X-rays.

A serious problem for the value of the solid angle is the dimension of the beam spot on the sample. The solid angle varies as a function of the position on the sample. For inhomogeneous samples, this can lead to errors in the calculated concentration even if a uniform beam is used. However, the variation of the solid angle averages out for homogeneous samples. The variation is aggravated by the fact that the sample surface and the detector surface are not parallel but make an angle of 45° with each other. To keep the influence of this variance small, it is advisable to keep the beam spot on the sample small. The best method to keep the solid-angle variation small is to place the sample surface parallel to the detector crystal. In the current setup, the variation of the solid angle over a spot size of 12 mm is 34 %. This reduces to 1.4 % for the parallel configuration. However, this configuration is not possible in the current vacuum chamber. Therefore, the minimal beam spot area of 4 mm is used for all measurements in this thesis. The variation of the solid angle over the beam spot area is 11.5% in this case and it remains advisable to use homogeneous targets.

Detector efficiency calibration

One way to obtain the detector efficiency is by developing a model of the detector. The detector efficiencies are then determined experimentally for a number of X-ray energies. The values of the parameters of the model can be obtained from a fit of the model to detector efficiencies that are experimentally determined. The parameters of the model can then be used to calculate the detector efficiency for every X-ray energy needed. There are many articles on this procedure [Cam 86a, Cam 90, Cam 91, Coh 80, Han 73, Ina 87, Paj 89, Shi 79, Shi 83]. The difficulty of this method is obtaining good experimental values for the detector efficiency, especially for low X-ray energies (below 5 keV). Another problem is that the functioning of the X-ray detector is still not fully understood. In the simplest model, the detector is described by several dead layers through which the X-rays have to pass and one layer where they have to be absorbed. The dead layers are first the detector window, in our case made of Be, secondly the electrical contact, in our case of Au, and finally an ineffective first part of the detector crystal, in our case Si. This last layer consists of two parts, the first part is a very thin layer where the detection efficiency is zero and the second part is a thicker layer with a reduced detection efficiency, this is called the layer of Incomplete Charge Collection (ICC). Later models include a possible layer of ice in front of the crystal [Coh 82]. This layer may be produced by condensation of vapour on the crystal, which is kept at 77 K, the temperature of liquid nitrogen. For use in the model,

the layer of ice can be incorporated in the Be window layer since the energy dependence of the attenuation coefficients of Be and ice are very similar [Bak 87]. Behind the dead layer is situated the active layer where the absorption of X-rays result in valid signals. An extra term f_{esc} has to be included for the escape of Si-K X-rays. These X-rays are produced through inner shell ionization of Si atoms by fluorescence. The term f_{esc} is calculated according to [Ree 72].

The detector efficiency can now be described as:

$$\begin{aligned} \varepsilon(E_{X_Z}) &= f_{esc}(E_{X_Z}) \sum_{i=1}^{3} \exp\left\{-\left(\frac{\mu(E_{X_Z})}{\rho}\right)_i (\rho x)_i\right\} \\ & \left(1-\exp\left\{-\left(\frac{\mu(E_{X_Z})}{\rho}\right)_{Si} (\rho x)_{Si}^{act}\right\}\right) \end{aligned} \tag{4.6}$$

where i represents three layers: the window (Be), the contact (Au), and the dead crystal layer (Si) respectively, and $(\rho x)_{Si}^{act}$ the thickness of the active layer. For low energy X-rays, the last term, which is the absorption probability in the active part of the crystal, is one. Therefore, the determination of the parameters can be split into two parts. The three parameters $(\rho x)_i$ can be determined with low-energy X-rays and the crystal thickness can be determined with high-energy X-rays.

First, the calibration for low-energy X-rays (below 6 keV) is discussed. Because the average absorption depth in the crystal for these X-rays is very small, the detector solid angle is independent of the X-ray energy. Calibrated sources can be used to measure the detector efficiency; however, for low-energy X-rays (below 5 keV) there are no calibrated sources available. Our approach to this problem has been to select pure chemical compounds containing both light ($11 \leq Z \leq 20$) and heavier elements (such as Fe). From these compounds, solutions have been made using distilled water that were, in turn, deposited on AE 98 filter papers (Schleicher & Schuell) and dried. Because the only variable of interest is the yield ratio of the light and heavy elements, it is not necessary to know the exact quantities of the compound deposited on the paper as long as the deposited quantities are much smaller than the mass of the paper. The measured yield has to be corrected for the self absorption of the X-rays in the paper since the paper is rather thick (4.7 mg/cm^2) and the X-ray energies are low. For this kind of sample, Condition 16 (Section 2.1.2) is valid and Eq. 2.21 (Section 2.1.2) can be used for the calculations. For these calculations, the mass thickness and the composition of the paper have been determined with NBS. To measure all the mass deposited on the paper the beam spot is made larger than the spot on the paper. The detector efficiencies found in this way have been used to calculate the parameters in Eq. 4.6 using a least squares fit.

In a preliminary experiment, the following chemical compounds have been used: $NaSO_4$, $MgSO_4$, $Al_2(SO_4)_3$, $CaSO_4$, and $FeSO_4$, [Kof 91]. All the detector efficiencies are relative values to the efficiency for Fe. Because the detector efficiency cannot be larger then one, it is possible to multiply Eq. 4.6 by an extra

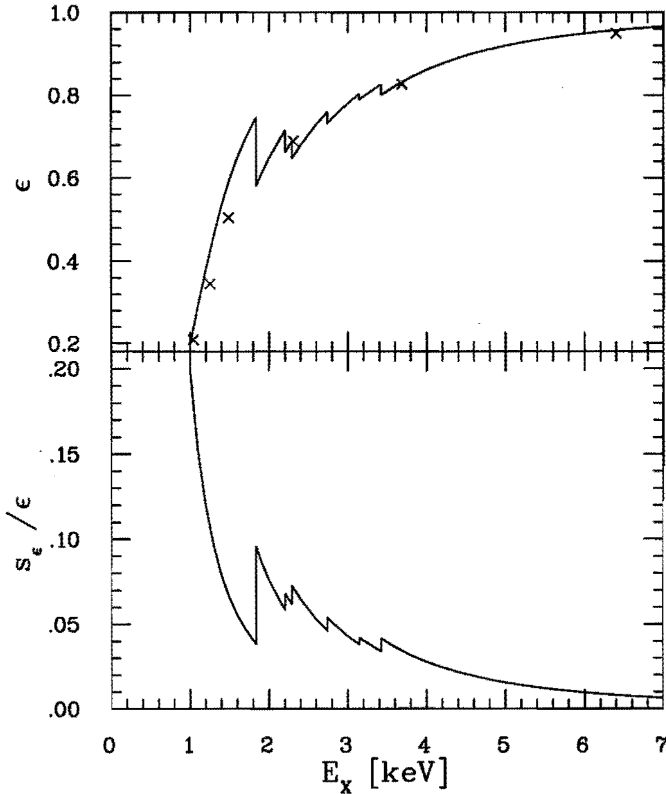

Fig. 4.11: Top: the detector efficiency as a function of the X-ray energy. The × are the measurement points and the line is calculated from the layer thicknesses found from the fit. Bottom: uncertainty in the detector efficiency calculated from the layer thicknesses.

factor for use in the fit. This factor is a correction for the fact that the detector efficiency for Fe is not one. The results of the measurements and the least squares fit are displayed in Fig. 4.11. The resulting values for the layer thicknesses are: Be window: $10 \pm 1\mu m$; Au contact: $0.04 \pm 0.01\mu m$; Si dead layer: $0.3 \pm 0.1\mu m$. The Si dead layer includes the ICC layer because only the Gaussian component of the peak is used. The ICC layer results in a low energy tail (see the next section), which is added to the background during the fit. This should always be done during later measurements to obtain consistent results. The manufacturers value for the Be window thickness is 8 μm. From a comparison of the measured value with the manufacturers value, no definite conclusion can be made about the existence of a layer of ice on the crystal since the two values are close together and there is no information about the accuracy of the manufacturers value. Because this detector was relatively new during calibration, it is still possible that a layer

of ice develops over longer periods of time. There is also no information from the manufacturer about the thickness of the other two layers but the stated crystal thickness is 3 mm. For each layer the uncertainty in the transmission through this layer is calculated according to Eq. 4.4. These uncertainties are added according to standard error calculation rules (see Section 3.2) to obtain the total uncertainty in the detector efficiency, shown in Fig. 4.11 bottom. As for the absorbers, the uncertainty is a maximum value since the layer thicknesses and the X-ray absorption coefficients are dependent variables for this type of calibration. From these measurements, it can be concluded that this is a useful method for the efficiency calibration but further work is needed to develop the method and to be able to use more sophisticated detector models.

The thickness of the crystal is not accurately determined. Therefore, we use a thickness of 3 mm as stated by the manufacturer. An uncertainty of 0.5 mm is used because nothing is known about the accuracy of the value for the thickness.

4.7 Data Analysis

The first step in the analysis is finding the areas of the X-ray peaks in the spectrum. For this purpose, the fitting program AXIL is used. Next, the thickness and/or concentrations of the light elements ($Z \leq 10$) are obtained using NBS. A new program has been developed for the calculation of the concentrations using the data acquired in the first two steps. This program can also calculate the uncertainties according to the method described in Chapter 3.

Spectrum evaluation

From the PIXE measurement, a spectrum is obtained in which the x-axis represents the energies of the detected X-rays, often given in channel numbers, and the y-axis the number of detected counts of given energy. From this spectrum, the yield $Y(X_Z)$ for a certain X-ray line has to be found. This yield is the area of an X-ray peak in the spectrum. The determination of the peak area is complicated by the fact that the peak is situated on top of a background and that it may overlap with other peaks. There are several computer programs, based on different methods, available to find the peak areas. Reviews evaluating some of these programs are presented in [Cam 86, Wat 87]. Notwithstanding great differences in methods and data bases used in these programs, the results for the peak areas of thin targets do not diverge more than 3% [Cam 86]. For intermediate-thick and thick targets, the results for the peak areas are slightly worse mainly because some programs did not include thick target corrections. To find the peak areas in the spectrum, we use the program AXIL [Esp 77, Mae 86].

The program uses the data of Thinh and Leroux [Thi 79] for the X-ray absorption coefficients. In the program, a model describing the spectrum is build

and then the parameters of this model (including the peak areas) are found by a non-linear least-squares fit (NL-LSF) of the model to the real spectrum. The peak shape is represented by a Gaussian. In reality, the X-ray peaks do not have perfect Gaussian shapes but they contain a low energy tail. This tail is attributed mostly to incomplete charge collection in the first layer of the detector crystal (see Section 4.6). To obtain accurate areas of X-ray peaks situated on a low energy tail, the shape of the tail must be known. There are many articles presenting models of the tail and comparing it with experiments [Cam 85a, Cam 91, He 90, Ina 87, Shi 83] but the models are semi-empirical and the process leading to the low energy tail is still not fully understood. The program AXIL uses a data base of shapes for the low energy tail of the K X-ray lines of the elements with $12 \leq Z \leq 35$. During the fit, this shape is scaled on the peak height and added to the background. For our detector, the peak shape data base of AXIL gives good results for the elements with $Z \geq 26$ (Fe) but for low Z elements (especially $Z \leq 17$, Cl), the peak shape of the data base differs from the measured peak shape. Ideally, there should be a tailshape data base for every detector since individual characteristics of the detector and its fabrication might influence the shape of the low energy tail [Joh 88].

The uncertainty in the peak area can be dealt with in several ways. First, there is the uncertainty given by the program AXIL. This uncertainty is based on the error matrix used in the NL-LSF and reflects the error propagation of the statistical error in the number of counts in each channel. This is only correct when the model and the data base are perfect and there is no correlation between the different parameters in the model. The first two conditions are not always true (e.g. for the peak shape corrections). The last condition is also not true in many cases, e.g. for overlapping peaks. A second possibility to acquire an insight in the uncertainty is the χ^2 value. AXIL gives this value per peak area. Normally, χ^2 is used to check if the used model is correct. If the fit is perfect, χ^2 is one. If χ^2 is large, the model or the values for its parameters are probably not good, e.g. the background is not chosen correctly. Alternatively, it can be argued that the uncertainty used for the fit, the statistical error in the number of counts per channel, is too small. Than, χ^2 can be used to correct the uncertainty in the peak area by multiplying this uncertainty with χ.

A last method of estimating the uncertainty is a simple recipe adopted by Clayton [Joh 88]. For this method, the calculation of the peak area Y_P is assumed to be a substitute for the subtraction of a background area Y_B under the peak from the total area $Y_T = Y_B + Y_P$. For this operation, the uncertainty is easy to calculate using Poisson statistics and it is $\sqrt{(Y_P + 2Y_B)}$. To obtain the background area Y_B, it is necessary to determine the X-ray energy width of the background. Clayton used an interval of $\pm 3\sigma$ around the peak centroid with σ the standard deviation defined by a Gaussian distribution. The uncertainty in the peak area is sometimes changed to account for the fact that the background under the peak

has to be determined from adjoining parts of the spectrum: $s_Y = \sqrt{(Y_T + FY_B)}$, with $F > 1$, a factor determined by the uncertainty in Y_B. We assume that $F = 1$ for a fit with the program AXIL because the background is determined taking into account the whole spectrum.

Actual uncertainties can be larger in specific cases, e.g. if there are overlapping peaks. Values obtained with the above methods have been compared for a number of fits. It was found that the last method almost always results in larger uncertainties except when χ^2 is very high. In view of the above discussion, it appears reasonable to use the last method described above to obtain uncertainties for the peak area. Nevertheless, the uncertainty determined with any of the above methods can be misleading because changes in the fit such as a different background model or another fitting region can lead to much larger differences in the peak area than expected on the bases of the the calculated uncertainty. Therefore, it remains essential to visually compare the fit and the measured spectrum.

NBS analysis

In many cases, the matrix elements are mainly light elements with $Z < 10$. The concentrations of these elements are needed for the calculation of the total stopping power and the total mass absorption coefficients of the sample (see Section 2.1.1). Also, the thickness of the sample is needed to determine $E_{P,f}$, unless the thickness is larger than the proton range. When secondary fluorescence (SF) can play a role, the value of the thickness is not needed when the thickness is considerably larger than the proton range (see Section 2.2). The values for these quantities cannot be obtained with PIXE. We have chosen to use NBS as a technique for obtaining these values. NBS can be used to obtain both the sample thickness and the concentration of the light elements. However, NBS cannot be used for samples thicker than about half the proton range because protons scattered at the back of the sample must have sufficient energy to leave the sample at the front end. In some cases, the mass thickness (in g/cm^2) can also be found by weighing the sample and measuring its area, especially for thicker samples. However, for biological samples, it is often impossible to determine the area of the sample. The advantage of NBS is that a NBS measurement can be done simultaneously with the PIXE measurement, except when the electron gun is used. A spectrum can be obtained using a particle detector placed at a backward angle. An extensive treatment of NBS is given in [Chu 78]. In this section, the emphasis is placed on some practical problems and on the uncertainty arising from this method.

There are several methods to extract the desired information from a NBS spectrum. The most comprehensive method is making a simulation and fit this to the spectrum. This can be done with the program RUMP [Doo 85, Doo 86]. Because the collision of 3.0 MeV protons on light elements is not elastic, the Rutherford formula for the scattering cross section cannot be used. Instead, experimentally determined cross sections have to be used. The choice of the data and the uncer-

tainty in it are discussed in Section 2.3.3. Since the scattering cross section has to be integrated over all proton energies in the sample, the error propagation has to be treated in the same way as the ionization cross section for PIXE (see Section 3.3.2). The stopping power is calculated using the data of Ziegler *et al.* (see Section 2.3.2). An additional error is introduced by the energy straggling. This makes it more difficult to determine the mass thickness of all but the thinnest samples. The program RUMP can, however, take into account the energy straggling when making a simulation. Also, it can consider the broadening of the peak of mono-energetic particles due to the energy spread of the beam and the resolution of the detector.

Because of the availability of the data for the scattering cross section (see Section 2.3.7), the detector angle is fixed at $147° \pm 1°$. The solid angle of the detector is limited by a slit of dimensions 3×10 mm^2. The width is chosen small (3 mm) to limit the energy spread. This energy spread is caused by a difference in the kinematic factor due to the variation in the back scattering angle. By measuring the distance between the detector and the sample, the solid angle is found: $\Omega_{\mathrm{NBS}} = 2.98 \pm 0.11$ msr. To arrive at an overall uncertainty for the thickness and the concentration of the light elements, also the uncertainties in the counts per channel and the charge measurement have to be taken into account. This method is described in more detail in Section 5.4, where it is applied to a practical problem.

Concentration calculations

From the peak areas in the PIXE spectrum, the concentrations have to be calculated, if necessary using data from the NBS analysis. For this purpose, the program PANEUT (Pixe ANalysis Eindhoven University of Technology) has been developed. The concentrations of the elements are calculated using eqs. 2.15 and 2.16. If the possibility of SF exists, the concentration is automatically corrected for the SF yield using eqs. 2.39, 2.42 and 2.43. The data base used in this program is discussed in Section 2.3. The integration over E_P is performed numerically by taking energy steps and then calculating $\Delta(Y(X_Z)/c_Z)$ from eqs. 2.15 and 2.16 and the thickness $\rho_S x(E_P)$ from Eq. 2.5 until the total thickness is reached or $E_P = 100$ keV. The value of 100 keV is the lowest value for which the cross section can be calculated (see Section 2.3.3) but contributions from the sample where $E_P < 100$ keV can be neglected (see Section 3.3.5). For the calculation of $\rho_S x(E_P)$, a fixed step size is used of 10 keV but the step size for the calculation of $\Delta(Y(X_Z)/c_Z)$ is increased to speed up the calculation. The step size of the i-th step is calculated in such a way that the maximum error in $\Delta(Y(X_Z)/c_Z)_i$ is smaller then 2% of $\sum_{j=1}^{i-1} \Delta(Y(X_Z)/c_Z)_j$. The maximum step size is restricted to 150 keV. In total, the numerical calculation of the integral results in an error smaller than 1%. The calculation of the SF yield can be fitted in easily by calculating eqs. 2.42 and 2.43 for every energy step. This involves solving extra

integrals, so it takes more time. A problem that can arise when the extra integrals are solved numerically, is discussed in Appendix B. Another difficulty is the term $\tau_{A,tot}$, the photo-electric absorption coefficient, in Eq. 2.40. In our data base, only the total X-ray attenuation coefficient μ_A is available and therefore this quantity is used instead of τ. However, τ_A is the main component of μ_A especially for SF where the X-ray energy, for which τ is needed, is always above the absorption edge of element A. Therefore, for K-lines below 40 keV, the error made by using μ_A instead of τ_A is no more than 3%. The uncertainty in the concentration is calculated according to the methods described in Chapter 3 and the uncertainty estimates for the data base are discussed in Section 2.3.

A final point of interest is the detection limit. If an element is not visible in the spectrum or if the peak in the spectrum is very small, the value of the detection limit can be of interest. Two types of detection limit can be distinguished: first, the limit of detection (LOD) and secondly, the limit of quantification (LOQ). The distinction is made because quantitative results near the detection limit (LOD) can be unreliable. The LOD is defined as $3\sqrt{(Y_B)}$ and the LOQ as $10\sqrt{(Y_B)}$, with Y_B determined in the same way as for the uncertainty in Y_P. PANEUT uses these definitions to calculate both detection limits and it marks measured concentrations that are below one or both detection limits.

Conclusion

In conclusion, it can be said that the data analysis is an important part of the total analysis of a sample. If the determination of the peak areas in the PIXE spectrum is not executed carefully, it can lead to serious errors in the values of $Y(X_Z)$. However, these errors do not always show up in the uncertainty estimate using one of the methods described in this section. The thickness of the sample and the concentration of the light elements can be determined using NBS. The uncertainty in the thickness depends largely on the sample itself. The uncertainty is larger when the sample becomes thicker because of more energy straggling. Also, the uncertainty increases when the sample contains more elements because of an increased complexity of the spectrum. The uncertainties in the concentrations of the light elements depend mainly on the uncertainties in the Non-Rutherford scattering cross sections but the complexity of the sample can also play a role. The error propagation of various uncertainties to the calculated concentration using the PIXE formula is discussed in Chapter 3.

4.8 Conclusions

The experimental setup and its features are described in detail in this chapter. A number of systems has been introduced to facilitate the measurement of a variety of samples. These systems include an electron gun to prevent charge build-up on

thick, insulating targets; a beam-on-demand system to reduce pile-up and eliminate the need for dead-time corrections; a new Faraday cup for the charge measurements for thin samples and a rotating vane for the charge measurements for thick samples.

To calculate the concentrations of the elements in a sample, the values of a number experimental quantities are needed. These values have also been determined together with an estimate of their uncertainty. The experimental quantities include:

- the beam energy $E_{P,0}$, for protons in the energy range 3-4 MeV a shift of 70 ± 10 keV below the nominal value of the AVF cyclotron has been found;
- the number of bombarding particles, N_P, which has to be determined for every measurement individually; the uncertainty varies from less than 0.5% for the measurements with the Faraday cup to a few % for the rotating vane measurements;
- the X-ray detector solid angle $\Omega = 9.2 \pm 0.3$ msr for Mn-Kα X-rays;
- the X-ray detector efficiency $\varepsilon(E_{X_z})$, calculated according to Eq. 4.6 and depicted in Fig. 4.11 ;
- the absorber thicknesses:
  Be: $\rho t = 9.8 \pm 0.6$ mg/cm^2,
  C250: $\rho t = 250 \pm 6$ mg/cm^2,
  C360: $\rho t = 360 \pm 7$ mg/cm^2;
- the particle detector angle, 147° ± 1° and
- the particle detector solid angle $\Omega_{NBS} = 2.98 \pm 0.11$msr.

An overall picture of the data needed for a complete analysis and the data flows and programs is given in Fig. 4.12.

Further improvements of the measurements are possible but they will need a new vacuum chamber. There are two main points of improvement:

1. The sample has to be rotated 45° to reduce the spread in the detector solid angle. This is especially important for inhomogeneous samples.
2. A thick lead shielding around the X-ray detector is needed to reduce the background in the X-ray spectrum. This is important for reducing the detection limit.

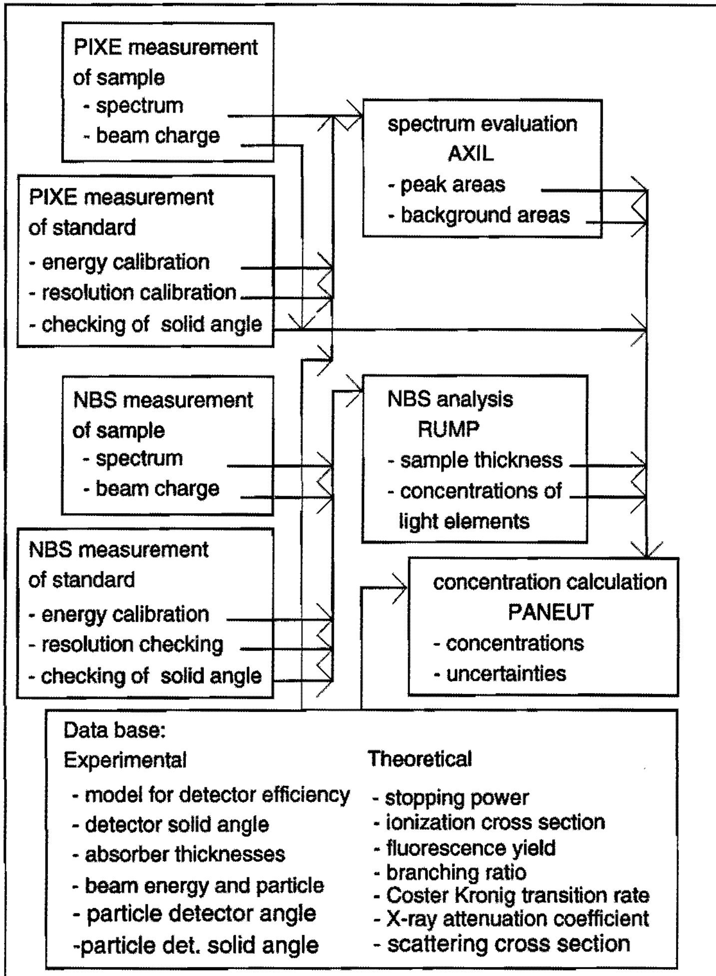

Fig. 4.12: Schematic overview of the data and data-flows needed for a complete PIXE analysis.

5 Evaluation of the absolute calibration method in TT-PIXE

The absolute calibration method is evaluated. This is done both by discussing some theoretical aspects of the procedure and by performing some experiments. The samples for the experiments include thick metal foils in the range of $Z = 13 - 50$ and some biological reference materials.

5.1 Introduction

In the previous chapters, the procedure of absolute calibration for the PIXE analysis, including a formalism for the uncertainty calculation, is developed. In this chapter, we make an evaluation of this procedure. The evaluation contains some theoretical considerations and some experiments. In the first section, the absolute calibration procedure is evaluated on theoretical grounds. This is done in two parts. First, the models as described in Chapter 2 and Chapter 3 are discussed. This discussion includes an evaluation of the conditions made in Chapter 2. Next, the influences of the uncertainties in the quantities needed for the absolute calibration and in the experimental procedure are discussed. It is done very briefly because this has been done extensively in the previous chapters. In the following sections, some experiments are presented. Special emphasis is placed on the calculation of the uncertainties in the concentrations according to the formalism described in Chapter 3. The samples used for the experiments are of increasing complexity, starting with a series of thin Ni foils for the calibration of the setup, analysed in Section 5.3. In the next section (Section 5.4), a set of thick monoelemental metal foils is analysed and in Section 5.5 two reference alloys are used. These analyses include the SF yield that is analysed further in Section 5.6. The last of the experimental sections (Section 5.7) is devoted to the measurement of biological reference samples.

5.2 Models and uncertainties

The physical model needed for TT-PIXE can be divided in two parts: the model for the primary production of X-rays and the models for the secondary productions. To calculate the primary production, two thick-target effects have to be taken into account: (1) The slowing down of protons in matter and (2) the absorption of X-rays in matter. To obtain the total X-ray yield of a tick target, the X-ray production in a small volume has to be integrated over the whole sample

under proton bombardment taking into account both tick-target effects (see Section 2.1.1). In principle, this model is capable of dealing with all sorts of targets, also inhomogeneous targets. However, in practice often insufficient information is available to describe the inhomogeneous targets. Therefore, this study has mainly been restricted to targets with a homogeneous matrix composition. The general theory of Section 2.1.1 is simplified for a number of relevant cases in Section 2.1.2. Trace elements may still be distributed inhomogeneously since they do not determine the two thick-target effects (see Condition 12 on page 18).

There are a number of conditions and assumptions underlying the formulas used for TT-PIXE. Some general discussion of these conditions and assumptions is already presented in Section 2.1. Here, some additional discussion specific for our setup is presented. There are four effects that influence the unambiguous relation between the depth x in the sample and the proton energy E_P at this depth (Eq. 2.5). These are energy straggling, spread in the proton energy $E_{P,0}$, variation in the direction of the protons and multiple scattering (Assumption 1 - Assumption 4). In first order, energy straggling (see [Chu 78]) and the spread in $E_{P,0}$ are symmetric around an average value, so Assumption 1 is valid and the fact that $E_{P,0}$ is not mono-energetic (Condition 2) does not introduce additional errors. Variation in the direction of the protons leads to spread in the beam angle α. The influence of the spread in α is minimal because $\cos\alpha$ is used in the equations for TT-PIXE and $\alpha = 0$ for our setup. Therefore, a standard deviation in α of 8° leads to a standard deviation of 1% in $\cos\alpha$. Multiple scattering causes an angular distribution of the protons after they have traversed a certain amount of material. This distribution broadens when the protons have reached deeper parts of the sample. The effect of this distribution on the yield or the calculated concentration is again minimal because $\alpha = 0$ and there is no shift in the centre of the distribution.

Condition 5 states that there is no variation in $\cos\theta$. The angle θ between sample normal and the direction of the detector is 45° for our setup. Due to the solid angle of the detector, there is a variation of ±3° in θ leading to a maximum spread of ± 5.2% in $\cos\theta$. If the beam diameter is 4 mm, this leads to a maximum spread of ±0.7% in $\cos\theta$ and this can be neglected in comparison with the spread due to the solid angle. Since the detector surface is a circular disk, the influence of the outer edges is smaller than the influence of the center. Taking this into account, the standard deviation in $\cos\theta$ is 2.9%. The term $\cos\theta$ is used in the equation Eq. 2.7 for the transmission through the target together with the X-ray attenuation coefficient μ_t. The assumption that Condition 5 is valid, does not introduce additional errors, because the uncertainty in μ_t (10%) is much larger than the uncertainty in $\cos\theta$.

Assumption 9 states that large-angle scattering of particles in the target can be neglected, that is over all angles except small angles where multiple scattering is dominant. To estimate this effect, the Rutherford scattering cross section is

integrated over all scattering angles larger than 8° and all proton energies between 1 and 3 MeV. The upper limit is the proton beam energy $E_{P,0}$. The lower limit of 1 MeV is chosen because 99% of the contribution to the yield comes from the part of the target where the proton energy is still above this value (see Section 3.3.5).The fraction of scattered protons to the total number of protons is then found by multiplying this integrated value with the number of atoms/cm^2 in the sample. In an extreme case of a thick Sn foil, this fraction is about 0.5%; that is at the depth in the sample where the proton energy is 1 MeV, the total number of protons is about 0.995 of the number at the surface of the sample. In most other cases, the fraction of scattered protons is much smaller and the use of Assumption 9 is justified.

A last condition to be discussed is Condition 11, which states that the individual stopping powers and mass absorption coefficients can be added according to their mass fraction. In Section 2.3.2, it is concluded that Bragg's rule for the stopping power is valid for proton energies above 1 MeV within a few percent. The validity of the summation of the mass absorption coefficients is much less clear (see Section 2.3.6). However, systematic errors introduced when this rule is not valid, only become important when these errors are comparable to or larger than the uncertainties in the individual values.

There are several secondary processes able to create additional characteristic X-rays. These processes rely on different mechanism to ionize the sample atoms. There are four possibilities: (1) ionization by other characteristic X-rays, (2) ionization by secondary electrons, (3) ionization by Auger electrons and (4) ionization by Bremsstrahlungs X-rays. As explained in Section 2.2, the ionization by characteristic X-rays, called Secondary Fluorescence (SF), is the only process with a sufficiently high yield that correction for it is necessary. The process of SF is similar to the primary PIXE production and can be treated in much the same way. The formulas involved are only valid for targets with spatially homogeneous matrix compositions. The formulas are however more complicated because SF is a secondary process (see Section 2.2). The quantities for this process are the same as the quantities for the primary PIXE process. There are a few extra conditions for SF which are discussed in Section 2.2.

We have used a mathematical model for the uncertainty assessment. This model is applied for the calculation of the uncertainty in the concentration. For this calculation, all effects influencing the uncertainty in the concentration are treated separately. It is assumed that all these effects are independent and that the uncertainties associated with these effects can be treated as standard deviations of a Gaussian distribution (see Section 3.2). Standard statistical mathematics can then be used for the uncertainty calculation. In practice, however, not all quantities are independent. In some cases, the dependency of the quantities reduces their

influence on the uncertainty in the concentration, see for example Section 4.6 on the calibration of absorbers. In other cases, however, the dependency may increase the overall uncertainty (see Section 3.4.6).

The equations for TT-PIXE and SF contain many quantities. Part of the quantities are physical quantities contained in the data base, such as the stopping power, the production cross section, and the X-ray attenuation coefficient, and they are discussed in Section 2.3 together with their uncertainties. Part of the quantities are experimental quantities, such as N_P, Ω, ε, T_{abs}, Y, $E_{P,0}$, $E_{P,f}$, the angles θ and α and the matric composition. These quantities except θ and α are determined or discussed together with their uncertainties in Chapter 4. The uncertainties in the angles θ and α stem from the determination of the values and from other processes. These processes are discussed above and their effect is generally much larger then the uncertainty caused by the determination of the angle. The addition of all uncertainties to obtain the total uncertainty in the yield or the concentration is described in Chapter 3.

A source for errors not previously discussed is the sample preparation. The preparation of targets for TT-PIXE is often minimal, which reduces the risk of introducing contaminants during the preparation. There are two problems in particular that have to be considered for the PIXE analysis: One is the surface roughness [Cam 85] that can reduce the PIXE yield by a few percent to more than 10%. The other problem is the sample homogeneity. Samples taken from a material to be investigated are often representative of the composition down to a certain mass. The amount of material investigated by PIXE is often less than this mass. This problem can be countered by measuring several targets of the same material. Sample inhomogeneities can, however, also be introduced by the sample preparation. The sample preparation always plays a role in the analysis, no matter what calibration method is used. Therefore, it is not investigated in this study. However, both problems described above make it possible that the total uncertainties in the concentrations are larger than the calculated values presented in this thesis.

The total uncertainty, as calculated in Chapter 3, is an absolute uncertainty. This means that it is an estimate of the deviation from the true value of the yield or the concentration. The uncertainties contributing to the total uncertainty can be divided into two groups: statistical uncertainties and systematic uncertainties. The uncertainties in N_P and in the yield Y are the main statistical uncertainties. The variations that occur when the experiments are repeated, are defined by these uncertainties. This is notwithstanding the fact that part of the uncertainty in these two quantities can be caused by systematic errors, e.g. the calculation of the background during the peak fitting procedure can introduce systematic errors in the peak area Y. Part of the uncertainty in the solid angle is also a statistical uncertainty since the solid angle can vary slightly from day to day because the

detector is sometimes removed. Generally, these statistical fluctuations are smaller than the systematical uncertainty in the determination of the solid angle. All other quantities have systematic uncertainties, thus these uncertainties do not influence the reproducibility of the measurements. That does not imply that these uncertainties are not standard deviations of a Gaussian distribution. If these uncertainties are caused by a large number of smaller contributions, e.g. as is usually the case when the values are measured, the underlying distribution can be assumed to be Gaussian (see Section 3.2).

5.3 Measurements of thin targets

Before measurements can be done to verify thick target effects, the setup has to be checked with simple targets. One aspect to be checked is the reproducibility, which is done below. Another aspect is the measurement of thin targets, which is discussed next. For thin targets, the PIXE yield has to increase linear with the thickness or concentration. The same applies for the NBS analysis. The linearity of the experimental setup is illustrated by the measurement of a series of thin Ni samples. The samples are made by evaporating Ni on polycarbonate foils. The series consist of ten different thicknesses with three samples per thickness. The samples were analyzed using both PIXE and NBS with a 3 MeV proton beam (nominal value). The samples are so thin that the PIXE formula for thin homogeneous targets (Eq. 2.17) can be used to determine the mass thickness of the samples. There are some contaminations of Cr, Mn, Fe and Cu in the Ni layer with concentrations between 0.1% and 5% and the total mass thickness is the summation of the thicknesses of all elements. The uncertainty in the thickness is found by adding all the experimental errors and the error in the production cross section according to standard error calculation rules (see Section 3.2). The error in the production cross section is itself a function of the errors in the ionization cross section, the fluorescence yield and the branching ratio and it is about 6% for Ni (see Section 2.3). The total uncertainty in the thickness is about 7%.

For the NBS analysis the Rutherford cross sections can be used with an error margin of about 5% [Boz 90]. The mass thickness is calculated using the approximation that the beam energy in the layer is constant and thus that the scattering cross section is constant. For this calculation it is assumed that there is only Ni present in the sample because the contaminations could not be distinguished in the NBS spectrum. Again the error is the summation of the experimental errors and the error in the scattering cross section according to standard error calculation rules and it is about 6%.

In Fig. 5.1 the thicknesses determined with PIXE and NBS are compared. The full line in the figure is a fit of $y = ax + b$ to the data points. The uncertainty in the thickness is used as a weighing factor for the fit. The coefficients are found to be $a = 1.03 \pm 0.01$ and $b = -0.08 \pm 0.02$. The results from the PIXE and

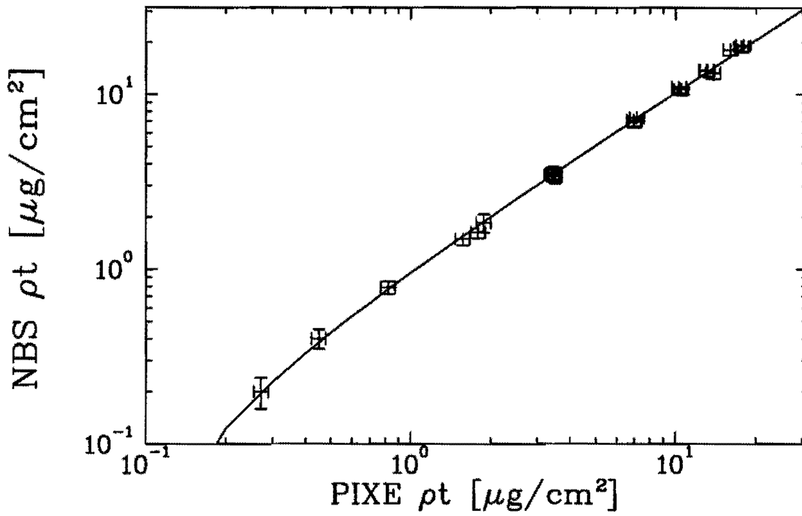

Fig. 5.1: Thicknesses measured by NBS versus thicknesses measured by PIXE for a set of Ni foils. The Ni is evaporated in different thicknesses on Nuclepore foils.

the NBS measurements are in good agreement which means that the experimental quantities, such as the detector efficiency of the X-ray detector, the solid angles of both detectors are determined with suitable accuracy. This statement cannot be made about the charge measurement since the NBS and PIXE measurements were made simultaneously with the same charge.

In addition to the linearity of the setup, the reproducibility is another impor-

Table 5.1: Reproducibility of the setup, demonstrated by two samples. The thicknesses are determined from PIXE measurements.

Al 300Å		Ni 100Å	
date	t μg/cm^2	date	t μg/cm^2
2-12-92	8.32	12-12-92	7.01
12-12-92	8.55	11-3-93 a	6.56
23-12-92	8.53	11-3-93 b	6.64
6-1-93	8.59	11-3-93 c	6.64
8-1-93	8.43	11-3-93 d	6.75
24-7-93	8.51	18-3-93	7.43
31-7-93	8.07	8-4-93	6.95
		22-4-93	7.27
		31-7-93	6.92
total	8.43 ± 0.18	total	6.91 ± 0.30

tant factor. To check the reproducibility, a thin Ni sample, from the above set, and/or a thin Al sample, also evaporated on polycarbonate, are analysed every measuring day. The results are given in Table 5.1. The standard deviations are 2% for the Al sample and 4% for the Ni sample. This spread is caused by the statistical uncertainties in the peak-area determination (usually $< 1\%$), variations in the solid angle of the detector, which is sometimes removed and the uncertainty in the beam charge. Another cause can be degradation of the foils due to radiation damage. There is no obvious explanation for the fact that the spread in the measurements of the Al foil is smaller than the spread for the Ni foil.

5.4 Measurements of thick mono-elemental foils

In this section, the measurements of a set of mono-elemental metal foils with atomic numbers ranging from 13 (Al) to 50 (Sn) are described. For these reference materials, no a-priori knowledge of the matrix composition is needed. Also, there is no possibility of secondary fluorescence. All the samples are homogeneous so that the TT-PIXE formula (Eq. 2.15 with Eq. 2.16) can be used for the calculations. The set of metal foils consists of ten different elements with thicknesses ranging from 10 μm to a value much thicker than the proton range. As a reference, the mass thicknesses have been determined by weighing the foils and measuring the areas; the results are called reference values. The foils have been measured using a 3 MeV proton beam. NBS measurements have also been done to determine the thickness. Even if the proton beam is not stopped in the sample, the charge has been measured with the rotating-vane device because multiple scattering made the use of the Faraday cup impossible (see Section 4.3). Typical beam currents were as low as 30-50 pA, selected to limit the PIXE count rate to a maximum of 2000-3000 counts per second. The BOD system was used to eliminate pile-up and the need for dead-time correction (see Section 4.4). There was no diaphragm in front of the detector. The spectrum fitting was done using peak-shape corrections where possible (see Section 4.7). For the elements heavier than Br no peak-shape correction is available. Typically, the use of peak-shape corrections in the fit reduces the peak area with 1-3%. The concentration of the main element in the foils is calculated using the mass thickness determined by weighing and measuring the area. This is done for both the K-α and the K-β lines except for Al and Si, where the K-α and the K-β lines do not result in separate peaks in the spectrum. The results of the measurements are presented in Fig. 5.2. From these results a clear jump in the calculated concentrations can be noticed resulting in an increase of about 25% for concentrations of elements with $Z > 40$. Further investigations revealed that this jump is caused by an energy dependence of the solid angle. The results of these investigations are presented next.

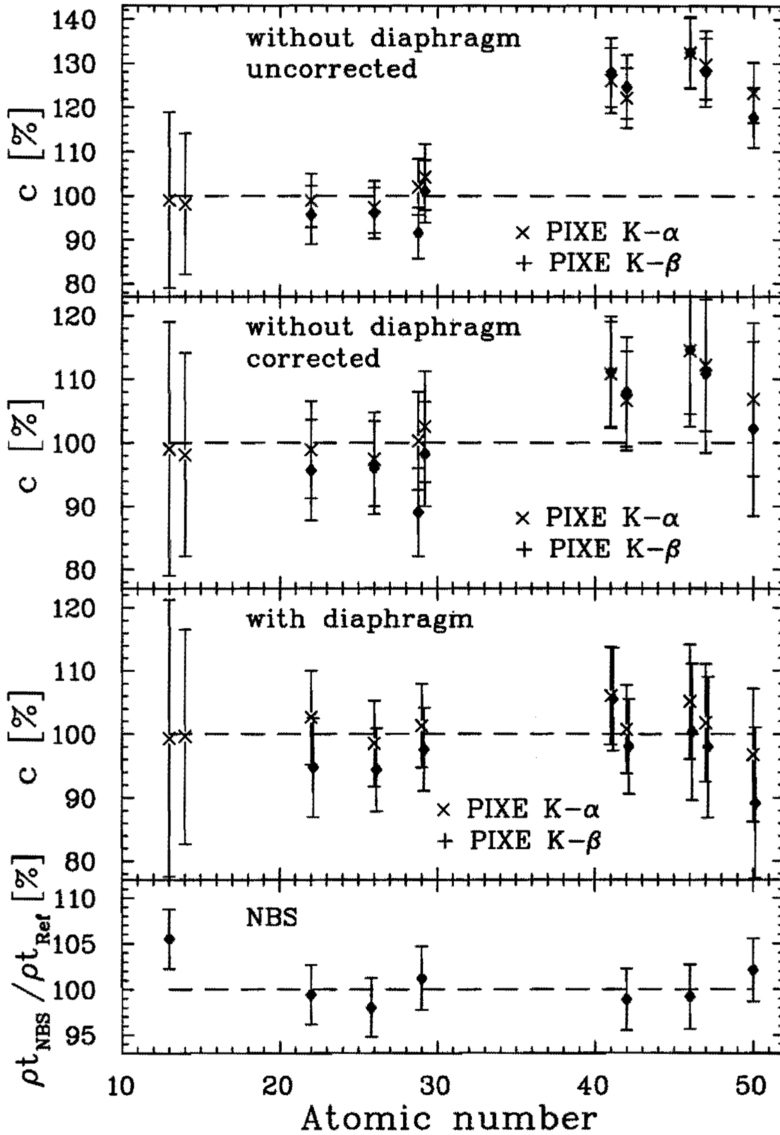

Fig. 5.2: Concentration of the main element in several metal foils as a function of the atomic number. The nominal proton beam energy is 3 MeV. The top figure shows the results for the PIXE measurements without diaphragm in front of the detector and without correction for the energy dependence of the solid angle. The upper middle figure shows the same measurements corrected for the energy dependence of the solid angle. The lower middle figure shows the PIXE results with diaphragm and the bottom figure the results for the NBS measurements. When more than one measurement is done for the same sample, the results are averaged. The reference thicknesses are given in Table 5.2.

New solid angle measurements

To obtain more information about the detector solid angle and its energy dependence, the measurements described in Section 4.6 have been repeated with a ^{55}Fe source and a ^{241}Am source. The ^{241}Am source emits Np L-lines with energies of 13.9 keV (Lα), 17.8 keV (main Lβ line), and 20.8 keV (main Lγ line) and a γ-line of 26.35 keV. The results of these measurements indicate that the effective detector area depends on the X-ray energy (see Fig. 5.3). This effect has also been reported in literature [Paj 89] and is attributed to the fact that the Si dead layer increases near the edges (see Section 4.6 for dead layer and detector model). The data points have been fitted to obtain a relation between detector area and X-ray energy. If we assume that there is a dead layer at the sides of the crystal that is radially symmetric and that decreases exponentially as a function of depth d in the crystal, than the radius r of the effective crystal at depth d is

$$r(d) = r_0(1 - r_1 exp\{-ad\}) \tag{5.1}$$

with a a positive constant, r_0 the total radius for the crystal, and r_1 the fraction of the total radius taken by the dead layer at the surface of the crystal. Using this equation, it is possible to obtain a fitting function for interpolation of the detector area to all X-ray energies that is in first order:

$$A_{\text{det}}(E_{X_Z}) = a_0(1 - a_1 exp\{a_2 d_{av}(E_{X_Z})\}) \tag{5.2}$$

with d_{av} the average absorption depth of X-rays with energy E_X and a_0, a_1, and a_2 the fitting parameters. The quantity d_{av} is used to relate the depth in the crystal to the X-ray energy. The result of the fit and the data points are displayed in Fig. 5.3. The parameter a_0 represents the total detector area including dead layer and it is 26.9 ± 0.9 mm^2. The detector area stated by the manufacturer is 30 mm^2, which is about 10% larger. The value of a_1 is 0.19 ± 0.03. This indicates that the dead layer occupies about 20% of the total detector area at the surface of the crystal. It should be remembered that $A_{\text{det}}(E_{X_Z})$ obtained from this fit is not really a function of depth in the crystal but it is an average of detector areas weighted according to the transmission of X-rays with energy E_X. It is therefore not possible to make a statement about the dead layer area at the backside of the crystal. The newly found area for the Mn-Kα line is smaller than the old value (21.7 ± 0.6 mm^2 compared to 23.3 ± 0.8 mm^2). This suggests that the detector area can be influenced by the history of the detector, like ageing or temperature cycles of warming up to room temperature and cooling down again.

The new values for the solid angle are now energy dependent:
$\Omega(E_X) = A_{\text{det}}(E_X)/r(E_X)$. Initially, the value increases with X-ray energy since A_{det} increases and then it slightly decreases after about 20 keV because of the increase of average absorption depth. For the quantity A_{det}, the fitting function (Eq. 5.2) is used multiplied by a constant so that A_{det} is 23.3 mm^2 for Mn-Kα. This is done because checking measurements on a thin Ni foil did not indicate

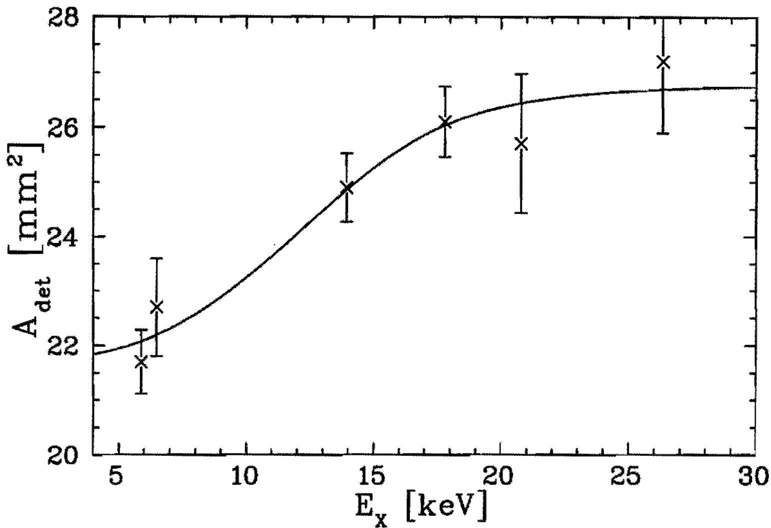

Fig. 5.3: Detector area determined by scans with a collimated X-ray beam for several X-ray energies. The solid line is a fit to the data points (see text). The old value of A_{det} for 6 keV is 23.3 mm^2.

a decrease of the solid angle during the period when the measurements without diaphragm in front of the detector were performed (see Section 5.3). The scans of the detector area with different X-ray energies were performed some time after these measurements. The uncertainty in this detector solid angle is about 5.5% mainly due to the uncertainty in A_{det}.

The X-ray energy dependence of both the distance r (see Section 4.6) and the effective detector area A_{det} makes it advisable to use a diaphragm in front of the detector. The opening of the diaphragm has to be smaller than the smallest effective detector area including increases caused by the distance between diaphragm and detector crystal. This makes the solid angle independent of the X-ray energy and the determination also becomes more simple. A drawback is that it reduces the solid angle, which is a disadvantage for obtaining low detection limits. Some measurements have been done with a diaphragm in front of the detector. However, most measurements have been done without diaphragm.

Revised and new measurements

The measurements, presented in the first part of this section, have been analyzed again using the results of the new measurements of the solid angle. The results are also displayed in Fig. 5.2 and they are presented in Table 5.2.

The uncertainty in the concentration is calculated according to Eq. 3.5. The partial uncertainty in the concentration due to the matrix composition, $\frac{s_{c_Z,c}}{c_Z}$, is zero since there is only one matrix element. The experimental uncertainties $\frac{s_E}{E_{P,0}}$,

Table 5.2: Results of the PIXE and NBS measurements of ten mono-elemental foils. If the reference thicknesses are lacking, the sample is thicker than the proton range. The PIXE measurements are performed without diaphragm in front of the detector but they are corrected for the energy dependence of the solid angle. The NBS values r ($= \rho t_{NBS}/\rho t_{Ref}$) are left open if the sample is too thick to determine the thickness with NBS.

	Reference			PIXE				NBS		
				K-α		K-β				
Z	ρt	$s_{\rho t}$	absorber	c_Z	s_c	c_Z	s_c	r	s_r	sample
	mg/cm^2			%	%	%	%	%	%	
13	3.52	0.02	Be	97	20			107	3.5	Al 15 a
			Be	101	20			104	3.3	b
13			Be	100	22					Al 100
14			Be	98	16					Si thick
22	3.83	0.06	Be	95	7	88	8	100	3.3	Ti 10 a
			Be	99.4	8	93	8			b
			C250	102	75	98	55	98	3.3	c
26	6.03	0.12	Be	97	7	96	7	99	3.2	Fe 10 a
			Be	91	7	90	7	98	3.1	b
			Be	101	7	99	7			c
			C250	100	26	99	19	97	3.1	d
29	10.4	0.2	Be	102	7	92	7	101	3.5	Cu 12
29			Be	102	8	98	8			Cu 125 a
			Be	107	9	104	8			b
			C250	103	15	101	11			c
41	22.79	0.09	Be	110	8	109	9			Nb 25 a
			C250	112	9	113	9			b
42	12.98	0.05	Be	105	8	107	8	99	3.4	Mo 12.5 a
			C250	108	8	109	8	99	3.4	b
46	13.0	0.4	C250	115	10	115	12			Pd 40
47	26.7	0.2	C250	112	10	111	13			Ag 25
50	9.13	0.02						102	3.6	Sn 12.5 a
			C250	107	12	102	14	102	3.6	b

$\frac{s_\varepsilon}{\varepsilon(E_{X_Z})}$, $\frac{s_T}{T_{abs}(E_{X_Z})}$, and $\frac{s_\Omega}{\Omega}$ are given in Chapter 4 and $\frac{s_Y}{Y(X_Z)}$, and $\frac{s_Q}{Q}$ are calculated as described in Chapter 4. The error propagation factors have been determined according to the methods described in Chapter 3 and the uncertainties in the data base are given in Section 2.3. All the partial uncertainties and the error propagation factors are given in Table 5.3.

The PIXE measurements have also been repeated with a 4 mm diaphragm in

Table 5.3: Partial uncertainties and error propagation factors for the K-α lines of the main elements in the foils. The letters a,b,c and d refer to the same measurements as in Table 5.1. Here, A stands for $P(c_Z, \mu_t)$ and B stands for $P(c_Z, E_{P,0})$. The uncertainties identical for all samples are $\frac{s_S}{S_t} = 3\%$, $\frac{s_\mu}{\mu_t} = 10\%$, $\frac{s_E}{E_{P,0}} = 0.6\%$, $\frac{s_\sigma}{\sigma^{ion}_{Z,K}} = 5\%$, $\frac{s_\Omega}{\Omega} \approx 5.5\%$. $P(c_Z, \sigma) = 1$ for all samples and $P(c_Z, S_t) = 1 - P(c_Z, \mu_t)$.

Z	$\frac{s_Y}{Y(X_Z)}$	$\frac{s_Q}{Q}$	$\frac{s_\varepsilon}{\varepsilon}$	$\frac{s_T}{T_{abs}}$	$\frac{s_b}{b_{Z,X(K)}}$	$\frac{s_\omega}{\omega_{Z,K}}$	A	B	$\frac{s_c}{c_Z}$	sample
13	0.2	2.3	6.7	17	0.1	4	0.68	0.16	21	Al 15 a
13	0.1	2.2	6.7	17	0.1	4	0.67	0.14	21	b
13	0.2	2.2	6.7	17	0.1	4	0.98	0.18	22	Al 100
14	0.1	2.2	4.4	11	0.1	4	0.97	0.35	17	Si thick
22	0.1	2.2	2.0	0.6	0.6	2	0.26	1.3	7.9	Ti 10 a
22	0.5	0.7	2.0	73	0.6	2	0.26	1.3	74	Ti 10 d
26	0.1	1.1	0.8	0.2	0.2	2	0.26	1.8	7.6	Fe 10 a
26	0.2	2.2	0.8	0.2	0.2	2	0.25	1.8	7.6	b
26	0.1	0.7	0.8	25	0.2	2	0.26	1.8	26	c
29	0.2	2.2	0.4	0.1	0.2	2	0.30	2.3	7.8	Cu 12
29	0.2	2.2	0.4	0.1	0.2	2	0.44	2.9	8.5	Cu 125 a
29	< 0.1	0.7	0.4	12	0.2	2	0.44	2.9	15	Cu 125 c
41	0.4	1.7	0.7	< 0.1	0.3	0.5	0.20	3.8	7.5	Nb 25 a
41	0.1	0.7	0.7	1.7	0.3	0.5	0.20	3.8	7.6	b
42	0.5	1.7	1.2	< 0.1	0.3	0.5	0.14	3.2	7.3	Mo a
42	0.1	0.7	1.2	1.5	0.3	0.5	0.14	3.2	7.5	b
46	0.1	0.7	4.5	1.1	0.3	0.5	0.16	4.2	8.8	Pd 40
47	0.2	0.7	5.5	1.0	0.4	0.5	0.16	4.1	9.3	Ag 25
50	0.4	0.7	8.6	0.9	0.4	0.5	0.07	3.3	11	Sn 12.5

front of the detector. The results are displayed in Fig. 5.2. For these measurements, the solid angle is independent of the X-ray energy and it is determined by the diaphragm. Comparing the PIXE measurements with and without diaphragm, it can be noted that the concentrations for elements with $Z > 40$ are systematically higher for the measurements without diaphragm. It is not clear what causes this deviation but a reason could be that the dead layer in the detector crystal is not radially symmetric as is assumed above. A complete 2-dimensional scan of the detector surface using the method described in Section 4.6 can precisely quantify this effect.

For the light elements (Al and Si), the dominating factor in the total uncertainty is the uncertainty in the transmission through the Be absorber. The partial uncertainty from the X-ray attenuation coefficient is the next largest factor. For

the other elements, the partial uncertainties are more evenly matched. In all cases, except for Al and Si, the error propagation for the X-ray attenuation coefficient is small so that the large uncertainty in μ (10 %) has no large effect on the uncertainty in the concentration.

From the measurements (Fig. 5.2), one other aspect can be noticed, that in some cases the concentration from the K-β line is lower than the concentration from the K-α line. It is possible that a systematic error is introduced during the spectrum fitting. The K-β line is much smaller than the K-α line. Therefore, it is much more sensitive to variations in the background. Variations in the calculated background can lead to a difference of as much as 7% in the area of the K-β peak whereas the difference in the K-α peak does not exceed 3%.

The accuracy of the uncertainty calculation can be tested with the so-called chi-squared test. For this test, the reduced χ_R^2 can be used that is given by

$$\chi_R^2 = \frac{1}{N-1}\sum_{i=1}^{N}\left(\frac{c_{\text{meas}} - c_{\text{ref}}}{s_{\text{tot}}}\right)_i^2 \tag{5.3}$$

with N the total number of X-ray lines used for the analysis. The term $1/(N-1)$ is the normalization factor for the number of degrees of freedom, which is the total number elements in the summation minus the number of parameters to be determined (one in this case). The terms $1/s_{\text{tot}}$ are used as weighting factors, with $s_{\text{tot}} = \sqrt{(s_{\text{meas}}^2 + s_{\text{ref}}^2)}$. The quantity χ_R^2 is about one if the uncertainty s_{tot} is calculated correctly and if the underlying statistical distribution is a Gaussian or a Poisson distribution. For the measurements with diaphragm, $\chi_R^2 = 0.23$ which is an indication that the calculated uncertainty is overestimated (see also Section 5.8).

The results of the NBS experiments are also given in Table 5.2 and in Fig. 5.2. The NBS measurements can only be used for samples that are so thin that particles scattered at the backside of the sample can still exit the sample in the direction of the detector. The NBS spectrum is a block where the width of the block is the energy difference of particles backscattered at the front and at the backside of the sample. The width is converted to a mass thickness using the program RUMP (see Section 4.7). This is done by comparing a simulation with the measured spectrum and adjusting the thickness to obtain a good fit. This method allows for the correction for straggling and the detector resolution. The main uncertainties in this procedure are the uncertainty in the fit and the uncertainty in the stopping power. Both uncertainties are added according to standard error calculation rules to obtain the uncertainty in the mass thickness. This method gives good results for all samples except for Al. The only reason can be that the stopping power is too small, exceeding the estimated uncertainty.

5.5 NIST reference materials

The complete calculation for both the concentration and the uncertainty, including SF, has been applied to two alloy samples. The samples are the reference materials ST 644 and ST 1223 from the NIST. The sample ST 1223 was chosen because it contains the right conditions for SF: the elements V ($Z = 23$) and Cr ($Z = 24$) are present in a predominantly Fe ($Z = 26$) matrix. As a comparison, also an alloy was obtained that does not show SF: this is a sample with a Ti ($Z = 22$) matrix and heavier minor elements (concentrations from 0.1% to several percent). Both samples are thick disks. The measurements have been done using a 3 MeV proton beam (nominal value, see Section 4.2) and a Be absorber in front of the X-ray detector but without a diaphragm. The values determined in the previous section are used for the solid angle. The rotating-vane device has been used for the measurement of the number of protons N_p and of course the BOD system has been used to reduce pile-up and eliminate the dead-time correction. The beam current was about 30 pA, selected to limit the count rate to 1000-2000 counts s^{-1}. Spectra of both samples are displayed in Fig. 5.4.

The concentrations are calculated using the absolute calibration method and the results are given in Table 5.4. The deviation of the measured concentrations from the reference concentrations is displayed in Fig. 5.5. For these two samples, the reduced chi-squared is $\chi_R^2 = 2.43$. This is an indication that the calculated uncertainty is too small. On the other hand, the total concentration for the two samples is about 100%. The deviation from 100% is smaller than the uncertainty in the total concentration (see Table 5.4). An important reason for the large spread in the deviation is the spectrum fitting. The spectrum of sample ST 644 is still not very complicated, although there is already some overlap of X-ray lines (see top figure in Fig. 5.4). The spectrum of sample ST 1223, on the other hand, is quite complicated with many overlapping lines, i.e. Mo-L and S-K, V-K and Cr-Kα and Fe-esc, Mn-K and Cr-Kβ and Fe-Kα, and Ni-K and Cu-K. From this point of view, ST 1223 is not an ideal sample for checking the SF yield, mainly because it contains too many elements. Our uncertainty estimation is based on a simple model, only taking into account the height of the background (see Section 4.7). The complications of peak overlap and difficulties with the background model, e.g. low-energy tailing, are not taken into account, which may lead to an underestimation of the uncertainty in the peak area. It is especially for the Mo-Lα, the Mo-Lβ, and the Mn-Kα peaks that the value of $(c_{\text{meas}} - c_{\text{ref}})/s_{\text{tot}}$ is large (> 2) due to the overlap of peaks. If on ground of the above discussion the three largest values of $(c_{\text{meas}} - c_{\text{ref}})/s_{\text{tot}}$ are omitted from the chi-squared calculation, the new value is $\chi_R^2 = 1.29$, which is much closer to one.

The results of the SF calculations for Cr are good, especially for the Kα line. This can be explained by the fact that the fitting of the Kα line is not much influenced by the spectrum overlap because the overlapping lines are small compared

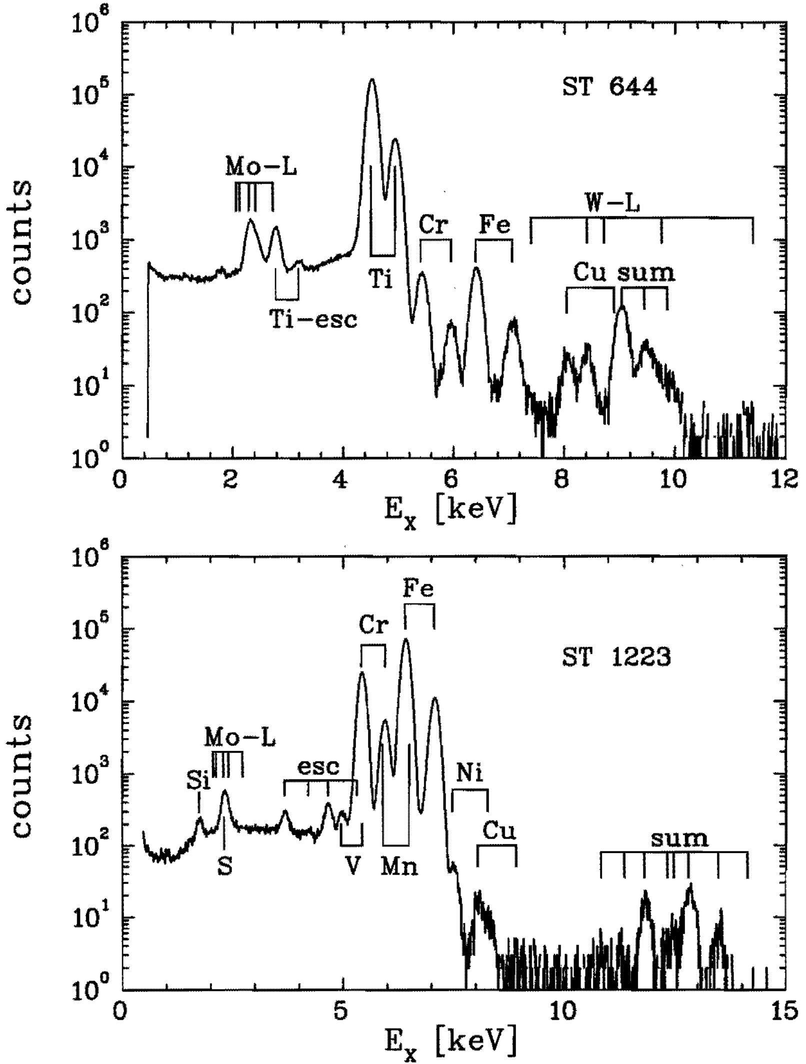

Fig. 5.4: Spectra of the two NIST reference samples measured with 3 MeV protons. The X-ray lines in the figures are K-lines unless otherwise noted. The term esc stands for escape-lines, see Section 4.7. Top figure: sample ST 644, without SF, charge: 44.2 μC. The Mo-K lines (at 17-20 keV) are not displayed in this figure to allow better detail in the rest of the spectrum. Bottom figure: sample ST 1223, with SF for V and Cr, charge: 48.1 μC. The Mo-K lines (not displayed in the figure) are still below the detection limits because the statistics are too low.

Table 5.4: Comparison of certified and measured concentrations for two NIST samples. Sample ST 1223 is the sample where SF occurs for Cr and V. The results for the Kβ lines are only given if the number of counts in the Kβ peak is large enough for the determination of the peak area to be sufficiently accurate and if this peak does not overlap with larger X-ray peaks. The total concentration is the summation of the Kα peaks only.

		ST 644			ST 1223				
Z		c_{ref} %	c_{meas} %	s_c/c %	c_{ref} %	s_c/c_{ref} %	c_{meas} %	s_c/c %	$R(SF/P)$ %
14	Si				0.327	2	0.42	19	
16	S				0.329	3	0.48	18	
22	Ti Kα		94	12					
	Kβ		87	12					
23	V				0.068	3	0.056	13	24
24	Cr Kα	1.03	1.17	14	12.64	0.2	12.7	10	37
	Kβ		1.04	14			11.5	9.9	31
25	Mn				1.08	0.9	1.44	10	
26	Fe Kα	1.36	1.37	13			87	11	
	Kβ		1.56	13			86	11	
28	Ni				0.232	2	0.22	14	
29	Cu		0.11	13	0.081	5	0.081	14	
42	Mo Kα	3.61	3.6	9.1	0.053	2			
	Lα		4.3	31			0.48	33	1.5
	Lβ		3.5	30			0.39	34	1.6
74	W Lα		0.49	26					
	Lβ		0.58	26					
	Total		102	10			103	8.5	

to the Cr-Kα line. For the Cr-Kβ line, there is a strong Mn-Kα line that overlaps the Cr-Kβ line. The calculated concentration for the Mn-Kα line is too large (see Table 5.4). If the surplus number of counts now contributed to the Mn-Kα line are added to the Cr-Kβ line, then more than the difference between c_{meas} and c_{ref} for this line can be accounted for. The V-Kα line is a small peak on the low energy tail of the Cr-Kα peak, making it difficult to obtain a correct peak area. It is therefore difficult to pass judgement over the accuracy of the SF yield calculation of this line. Other elements are found in our measurements, but not in the NIST list of certified elements, especially for ST 644.

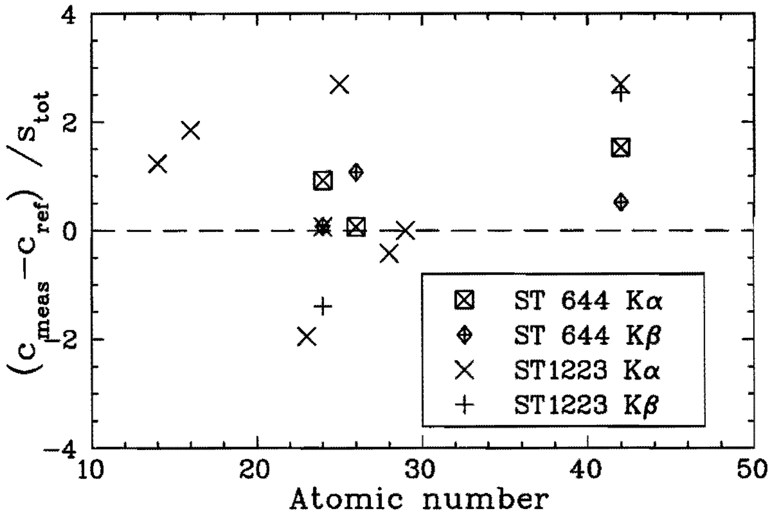

Fig. 5.5: Deviation of the measured concentration from the reference concentration normalized on the calculated total uncertainty for the two NIST samples. The elements V and Cr have an important contribution of the SF yield to the total X-ray yield.

5.6 Double metal foils

To try to obtain a better picture of the effects of SF, the set of metal foils (used in Section 5.4) has been used in combinations of two foils. Two series have been made, each with increasing ratio of SF yield to primary yield. One series is based on Cu ($Z = 29$) as element of which the X-rays enhance the yield of other elements. The other foils are Al ($Z = 13$), Ti ($Z = 22$), and Fe ($Z = 26$). The other series is Nb ($Z = 41$), Mo ($Z = 42$), and Pd ($Z = 46$) enhanced by Sn ($Z = 50$) X-rays. There is one extra combination suitable for this examination: Mo ($Z = 42$) and Pd ($Z = 46$). All other combinations are not useful because they do not result in a sufficiently large ratio of SF yield to primary yield or they are not practical because the foils are too thick. In general, it is better to have the foil first, where the X-rays are enhanced by SF; that is at the side where the proton beam enters. This results in a maximum detected X-ray yield for this element (A in the formulas). The number of detected X-rays of the element (B in the formulas) producing the exciting X-rays is less due to absorption in the first foil. Also, the ionization cross-section increases with decreasing proton energy (in this series Al is the exception) resulting in a higher primary production for element B and a lower primary production for element A. This is advantageous because it increases the ratio $R(SF/P)$. Only when the foil of element A is too thick, the foil order is reversed. The measurements are performed under the same conditions as described above for the NIST samples. The calculations of the concentrations,

however, impose extra problems because now the targets contain two layers and are therefore not homogeneous. A special version of PANEUT (see Section 4.7) is written to cope with this problem. For this purpose, the integration boundaries for x and L in Eq. 2.37 (Section 2.2) have to be changed. A distinction has to be made between the two cases of first the layer with element A and next the layer with element B and the reverse layer order. This results in different final formulas for both cases. The thicknesses of the two layers determine the integration boundaries. For the metal foils, the thicknesses are determined by weighing and measuring the area (see Section 5.4). The error assessment is performed as if the targets are one homogeneous layer, thus using the standard program, because of the complexity of incorporating the uncertainty calculation in the two layer version of PANEUT. The calculated uncertainties are, therefore, only indications of the 'real' uncertainties. The results of the measurements are given in Table 5.5.

The ratio $R(SF/P)$ becomes more important when the difference in Z between the two elements becomes smaller and when the Z of the elements becomes larger. The minimum difference in Z as a function of Z is given in Fig. 3.13. It should be noted, however, that the ratio $R(SF/P)$ is also influenced by the thicknesses of the two layers. Therefore, the values cannot be compared absolutely and they only indicate a general trend (see Section 3.4.5). These results are obtained without a diaphragm in front of the X-ray detector and are corrected for the energy dependence of the solid angle. They are compared with the results of the measurements of the single foils without diaphragm (here called c_{ref}, see Table 5.2) to obtain an impression of the accuracy of the SF calculation. This procedure is followed because the measured concentrations for $40 < Z \leq 50$ are systematically larger for the measurements without diaphragm compared with the measurements done with diaphragm (see Section 5.4). The X-ray lines are divided into two groups: one group with X-ray lines that have no or little SF, $R(SF/P) < 1\%$, and the other group with lines that do have a SF component. The reduced chi-squared for the two groups is: $\chi^2_R = 0.09$ for the group without SF and $\chi^2_R = 1.6$ for the group with SF. It is obvious from these results that the calculations including SF are less accurate than the calculations without SF. In general, the concentrations calculated with SF corrections are too low: $(c_{\text{meas}} - c_{\text{ref}})/s_{\text{tot}} = -0.4$. If the SF calculations are omitted the calculated concentrations are larger: $(c_{\text{meas}} - c_{\text{ref}})/s_{\text{tot}} = 0.5$. From these results is seems that the contribution of the SF to the total yield is overestimated in the calculations. For these measurements of the targets containing heavy elements ($Z > 40$), the validity of Assumption 5 and of the assumption in Section 4.7 is checked. The two assumptions are: the total X-ray attenuation coefficient μ_{tot} can be used instead of μ_{tot} minus the coherent and incoherent absorption coefficients for $\mu_t(E_{X_B})$ and it can be used instead of the photo-electric absorption coefficient $\tau_A(E_{X_B})$. The errors caused by these assumptions are largest for elements with $Z > 3$. For these measurements, it is found that the deviations introduced by these assumptions are less than 1% because the effects for $\mu_t(E_{X_B})$ and $\tau_A(E_{X_B})$ partly

Table 5.5: Results of the measurements to examine the SF yield by using combinations of two mono-elemental metal foils. The first seven columns contain the results for the element (A) of which the X-ray yield is enhanced by SF. The last six columns contain the results for the element (B) of which the X-rays produce the SF for element A. Here, $\Delta c = (c_{meas} - c_{ref})/s_{tot}$, c stands for c_{meas} and R stands for $R(SF/P)$. Note that for the Kα and Kβ lines of element A, both K lines of element B are involved in the SF production.

Z_A		line	c %	$\frac{s_c}{c}$ %	R %	Δc	Z_B		line	c %	$\frac{s_c}{c}$ %	Δc
13	Al	Kα	94	24	0	-0.17	29	Cu	Kα	101	12	-0.17
									Kβ	98	12	-0.05
22	Ti	Kα	93	12	0.4	-0.41	29	Cu	Kα	100	12	-0.24
		Kβ	89	13	0.6	-0.26			Kβ	97	12	-0.12
26	Fe	Kα	98	11	7.3	0.06	29	Cu	Kα	103	12	-0.04
		Kβ	93	11	8.6	-0.23			Kβ	100	12	0.09
42	Mo	Kα	95	8	11	-1.0	46	Pd	Kα	116	10	0.07
		Kβ	95	9	12	-1.1			Kβ	115	12	0.00
41	Nb	Kα	123	9	5.8	0.97	50	Sn	Kα	112	12	0.30
		Kβ	117	9	7.5	0.50			Kβ	103	15	0.05
42	Mo	Kα	102	9	6.1	-0.38	50	Sn	Kα	106	13	-0.06
		Kβ	101	10	7.5	-0.55			Kβ	98	15	-0.20
46	Pd	Kα	96	10	32	-1.3	50	Sn	Kα	106	13	-0.06
		Kβ	94	11	38	-1.3			Kβ	101	14	-0.05

cancel each other. It should be noted that the normalization on s_{tot} results in too small values. This is caused by the fact that that two measurements of the same type are compared. For a better comparison, only statistical uncertainties, such as the uncertainties in the yield and the number of bombarding protons, should be taken into account. For the group with SF, the situation is more complicated because in this case, also the uncertainties in the SF yield have to be taken into account. However, for a comparison of the two groups, the normalization on s_{tot} is acceptable.

5.7 Biological reference materials

As a demonstration of the procedure using NBS for the determination of the matrix composition, a set of biological reference materials, consisting of four powdered samples of biological reference materials from the IAEA, has been used. The matrix composition of biological samples consists mainly of light elements ($Z \leq 10$) and therefore the NBS measurement has to be done but there is also no possibility of secondary fluorescence. These powders are pressed into pellets to obtain thick targets, in which the beam is completely stopped. The values for the sample thickness are therefore not needed but the rotating-vane device has to be used to obtain the charge. A 3 MeV proton beam was used for the measurements. Because of charging of the targets, the electron gun was used during the PIXE measurements. This required a separate NBS measurement because of the interference of the electron gun with the NBS detector. Also, the PIXE measurement had to be done twice to obtain the concentrations of all elements. One measurement was done with the C250 absorber and one without any absorber. All measurements were done without a diaphragm in front of the X-ray detector.

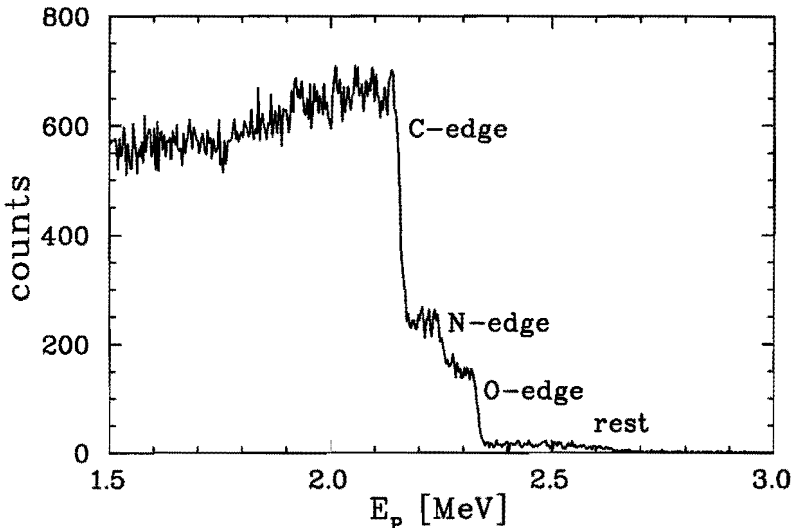

Fig. 5.6: NBS spectrum of the biological sample IAEA-H-8, horse kidney. The spectrum is measured using 3 MeV protons, with the detector at an angle of 147° . The charge is 0.93 μC.

Fig. 5.6 gives an example of a NBS spectrum. The height of the steps in the spectrum gives information on the concentrations of the matrix elements. The first step in the spectrum (rightmost step) results from the combined heavy elements ($Z > 10$) in the sample. All these elements are also measured with PIXE. To simplify the NBS analysis, it is assumed that all the heavy elements can be

approximated by one element, S. Because hydrogen can not be measured in a backwards configuration, the hydrogen concentration is taken as one minus the concentrations of the other matrix elements. The concentrations of the matrix elements are then found by making a simulation with the program RUMP and comparing this with the measured spectrum. The results of this method are presented in Table 5.6. The concentrations in this table are atomic fractions and they have to be converted to weight fractions needed for the PIXE analysis.

Before this conversion is done, it has to be explained how the uncertainty in the atomic fraction is calculated. For this purpose a formula for the calculation of the atomic fraction is needed. This formula is the formula for the number of counts $Y_{Z,i,NBS}$ in channel i of the spectrum from one element [Chu 78, Chapter 3]:

$$Y_{Z,i,NBS} = N_P \frac{\Delta\sigma_Z^{NBS}(E_P)}{\Delta\Omega} \Omega_{NBS} \frac{f_Z \Delta E_{ch}}{\cos\theta_1 [\epsilon]} \tag{5.4}$$

with

$$[\epsilon] = K_Z \frac{\epsilon_t(E_P)}{\cos\theta_1} + \frac{\epsilon_t(K_Z E_P)}{\cos\theta_2}, \tag{5.5}$$

$[\epsilon]$ is called the energy loss factor, and

θ_1	the angle between the sample normal and the proton beam (see Fig. 5.7),
θ_2	the angle between the sample normal and the direction of the NBS detector (see Fig. 5.7),
E_P	the energy of the proton in the sample corresponding to the energy of channel i in the spectrum (keV),
ΔE_{ch}	the energy width of one channel in the spectrum (keV),
K_Z	the kinematic factor for scattering on element Z for an angle of $\pi - \theta_1 - \theta_2$,
$\frac{\Delta\sigma_Z^{NBS}(E_P)}{\Delta\Omega}$	the differential scattering cross section for protons with energy E_P scattering under an angle of $\theta_1 + \theta_2$,
Ω_{NBS}	the solid angle of the NBS detector (sr),
$\epsilon_t(E_P)$	the total atomic stopping power for the sample (keV cm^2/atom); note that it has a different unit as $S_t(E_P)$.

The angles θ_1 and θ_2 are 0° and 33° , respectively. The yield $Y_{Z,i,NBS}$ for a certain element Z is obtained from the part of the spectrum left of the edge for that particular element as the height of the step in counts/channel (see Fig. 5.6). In analogy to the situation in a PIXE spectrum, we assume that the calculation of $Y_{Z,i,NBS}$ is a more complex form of the subtraction $Y_{Z,i,NBS} = Y_{tot,i,NBS} - Y_{B,i,NBS}$ with $Y_{tot,i,NBS}$ the total number of counts in channel i and $Y_{B,i,NBS}$ the number of counts in channel i of elements heavier than element Z. The uncertainty in $Y_{Z,i,NBS}$ can be estimated as $s_Y = \sqrt{Y_{tot,i,NBS} + FY_{B,i,NBS}}$ with F a factor (> 1) determined by the accuracy of the determination of $Y_{B,i,NBS}$. F is taken

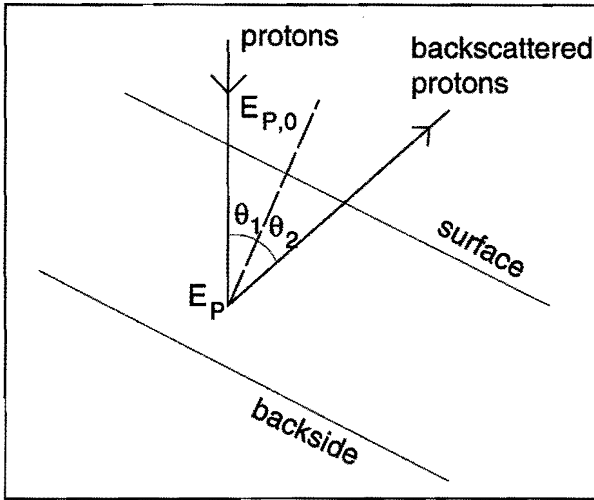

Fig. 5.7: Schematic layout of the scattering of protons in the target at the depth where the proton energy is E_P.

Table 5.6: Results of the NBS analysis of the four biological reference materials. f_Z is the atomic fraction of matrix element Z. The atomic fractions are normalized to one.

sample	f_H	s_f/f %	f_C	s_f/f %	f_N	s_f/f %	f_O	s_f/f %	f_{Rest}	s_f/f %
H-8	0.56	4.9	0.28	8.6	0.055	12	0.09	12	0.015	27
H-4	0.56	4.7	0.28	8.3	0.055	11	0.09	11	0.015	27
V-10	0.58	4.5	0.25	8.7	0.015	12	0.14	10	0.015	24
A-14	0.56	4.2	0.25	7.8	0.02	9.0	0.15	8.7	0.02	16

one because $Y_{B,i,NBS}$ is determined via the simulation taking into account the whole spectrum. From Eq. 5.4 the total uncertainty can be calculated:

$$\left(\frac{s_f}{f_Z}\right)^2 = \left(\frac{s_Y}{Y_{Z,i,NBS}}\right)^2 + \left(\frac{s_Q}{Q}\right)^2 + \left(\frac{s_\Omega}{\Omega_{NBS}}\right)^2 + \left(\frac{s_\sigma}{\Delta\sigma_{Z,NBS}/\Delta\Omega}\right)^2 + \left(\frac{s_{\Delta E}}{\Delta E_{ch}}\right)^2 + \left(\frac{s_{[\epsilon]}}{[\epsilon]}\right)^2 \tag{5.6}$$

with $s_{[\epsilon]}/[\epsilon] < s_{\epsilon_t}/\epsilon_t < s_{S_Z}/S_Z$. The uncertainty in the atomic fraction of H is determined in a different way: $s_{f_H} = \sum_Z s_{f_Z}^2$ because $f_H = 1 - \sum_Z f_Z$. Finally

the weight fractions and their uncertainties can be calculated:

$$c_Z = f_Z \frac{M_Z}{\langle M_Z \rangle} \qquad \text{and} \qquad \left(\frac{s_{c_Z}}{c_Z}\right)^2 = \left(\frac{s_{f_Z}}{f_Z}\right)^2 + \frac{\sum_Z (M_Z^2 s_{f_Z}^2)}{\langle M_Z \rangle^2} \tag{5.7}$$

with $\langle M_Z \rangle = \sum_Z f_Z M_Z$.

Fig. 5.8 gives an example for IAEA-H-8 of the two PIXE spectra measured with and without an absorber. Peak-shape corrections were only used for large peaks, notably P, S, Cl, K, and Ca, during the spectrum fitting because peak-shape corrections do not improve the fit results for smaller peaks. The beam current was again selected in such a way as to limit the count rate. For the measurement with the C absorber, it was about 2 nA resulting in a total charge of 2-3 μC and for the measurement without absorber, it was about 90 pA leading to a total charge between 0.14 and 0.26 μC. The measurements have been done using the BOD system to eliminate pile-up and the dead time correction. The final calculations of the concentrations have been done in an iterative way. In the first step, the matrix composition determined by the NBS experiment is used. In the next step, all elements that have a calculated concentration of more than 0.5%, are added to the matrix composition. The concentrations of all measured elements are then calculated again. This process is repeated until the difference before and after the calculation of the concentrations of the matrix elements measured with PIXE is smaller than 1%. The results of the analysis are presented in Table 5.7 and Fig. 5.9. There are some elements, which have a reference value for the concentration, but which are not certified. The uncertainty in the reference concentration in those cases is therefore left open.

The uncertainty in the measured concentration is calculated in the same way as for the metal foils using Eq. 3.5. In Chapter 3 the error propagation for the matrix composition is treated for a binary matrix. In this practical situation, the matrix can consist of any number of elements. The treatment is identical as for a binary matrix (see Section 3.3.4) except that the square of the total partial uncertainty in the concentration $(\frac{s_{c_Z,c}}{c_Z})^2$ is the quadratic sum of the partial uncertainties for every matrix element:

$$\left(\frac{s_{c_Z,c}}{c_Z}\right)^2 = \sum_i \left(P'(c_Z, c_i) s_{c_i}\right)^2 \tag{5.8}$$

with c_Z the concentration to be determined, c_i the concentration of matrix element i and s_{c_i} the uncertainty in this concentration. The summation is over all matrix elements minus the matrix element with the largest concentration. One matrix element can be skipped since the sum of all concentrations has to be one. Because the matrix concentrations are interdependent, the uncertainties in the concentrations are also interdependent. Therefore, the matrix element with the maximum absolute uncertainty s_{c_i} can be skipped. Generally, this is the matrix element with

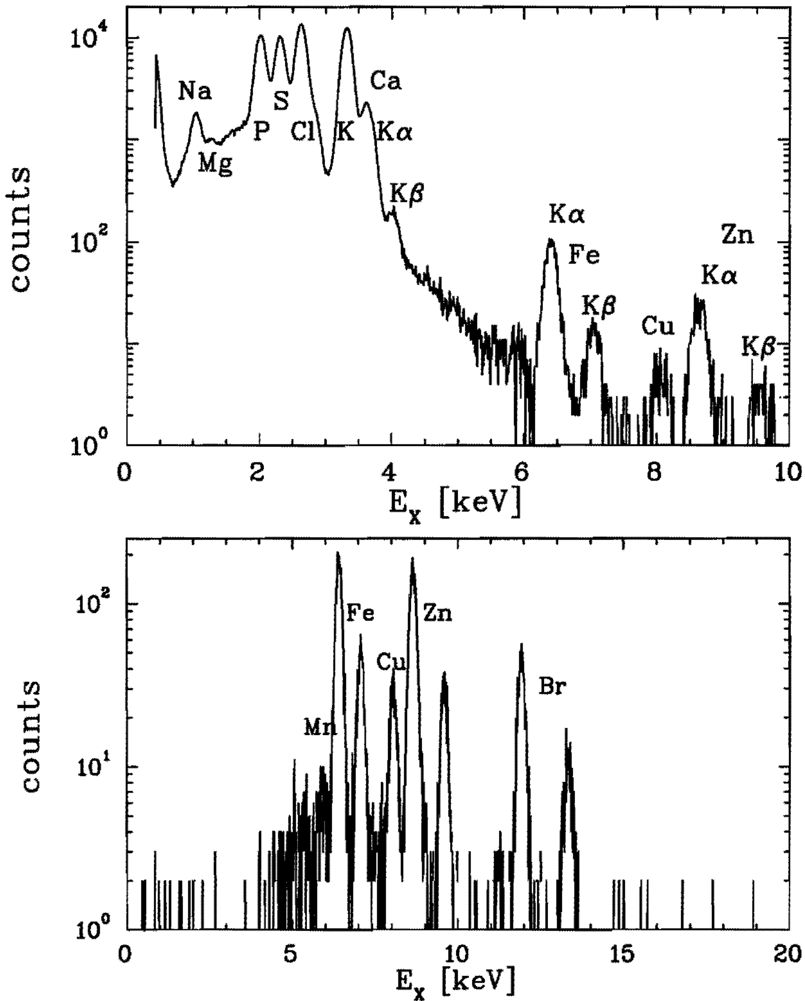

Fig. 5.8: PIXE spectra of the biological sample IAEA-H-8, horse kidney. The spectra are measured using 3 MeV protons. The top figure is the spectrum measured without absorber, charge: 0.14 μC and the bottom figure is the spectrum measured with the C250 absorber, charge 2.33 μC, with a different energy scale to emphasize the heavier elements.

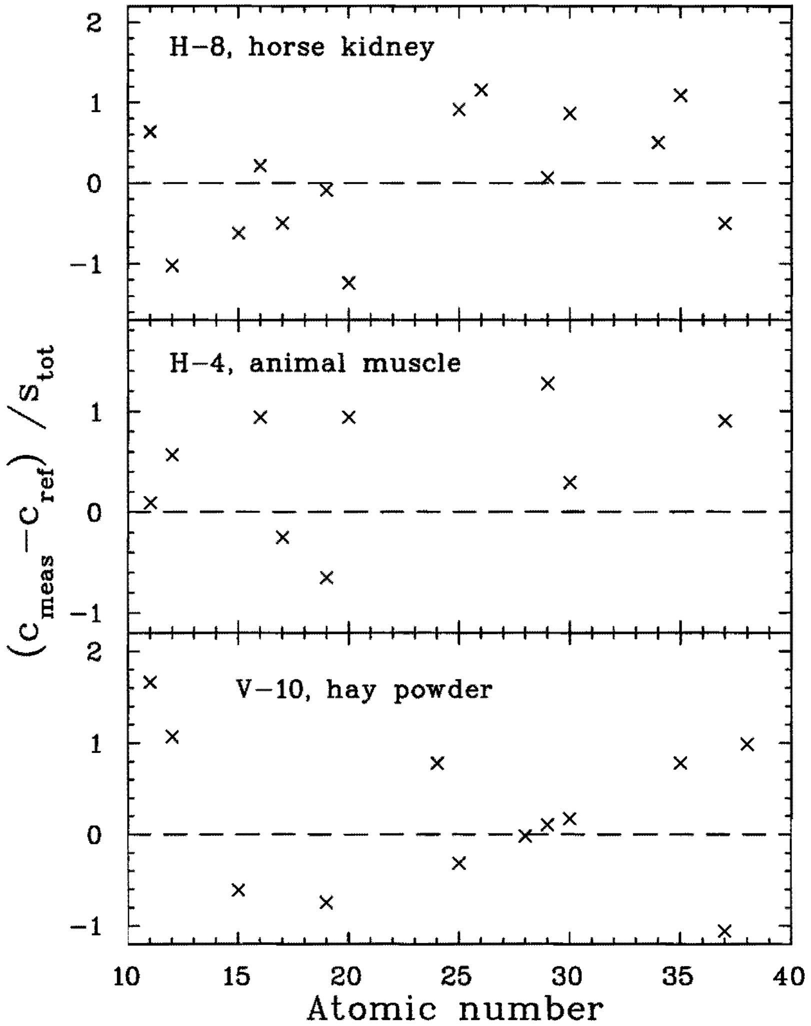

Fig. 5.9: Deviation of the measured concentration from the reference concentration normalized on the total uncertainty $s_{tot} = \sqrt{(s^2_{meas} + s^2_{ref})}$. Some values are not shown because of their large value; they are: 0.9 for $Z = 48$ in H-8; 6.5 for $Z = 26$ and 2.7 for $Z = 35$ in H-4; 5.0 for $Z = 13$ and 5.0 for $Z = 26$ in V-10. The values for A-14 milk powder are 0.43 for $Z = 11$, -0.47 for $Z = 19$ and -0.24 for $Z = 20$.

Table 5.7: Measured and reference concentrations for all four biological samples. The results for the light elements are obtained from the measurements without absorber and the results for the heavy elements from the measurements with absorber. When the uncertainty for c_{ref} is left open, the value of c_{ref} is for information only, it is not certified. Here A stands for s_c/c_{ref} and B stands for s_c/c_{meas}.

		H-8 horse kidney				H-4 animal muscle			
Z		c_{ref} ppm	A %	c_{meas} ppm	B %	c_{ref} ppm	A %	c_{meas} ppm	B %
11	Na	9600	3.1	11200	22	2060	6.1	2110	22
12	Mg	818	9.2	672	18	1050	5.6	1180	18
14	Si							607	14
15	P	11200	5.4	10200	15			8170	15
16	S	9000		9280	14	8000		9220	14
17	Cl	12600	8.4	11700	13	1890	4.4	1830	13
19	K	11700	6.4	11600	11	15800	3.7	14800	10
20	Ca	924	8.3	781	11	188	13	219	10
25	Mn	5.7	4.8	8.9	39				
26	Fe	265	5.7	301	9.0	49	4.2	110	8.3
29	Cu	31.3	5.6	32	17	4.0	8.3	6.4	29
30	Zn	193	3.1	212	10	86	3.9	89	9.3
34	Se	4.7	6.4	5.3[a]	23				
35	Br	104	11	122	9.8	4.1	15	8.6	18
37	Rb	22.2	3.6	21	14	19	7.8	22	13
48	Cd	189	2.4	224	17				

[a]This concentration is between the LOD and the LOQ (see Section 4.7)

the largest concentration. The error propagation $P'(c_Z, c_i)$ can be calculated as described in Section 3.3.1 except that if $c_Z(c_i \pm \delta)$ is calculated, δ has to added respectively subtracted from the matrix element with largest concentration to keep the sum one:

$$P'(c_Z, c_i) \approx \frac{c_Z(c_i + \delta) - c_Z(c_i - \delta)}{2c_Z(c_i)\delta} \tag{5.9}$$

As an example, the partial uncertainties and the error propagation factors are given for all elements present in sample H-8.

The largest uncertainties are either due to poor statistics resulting in large uncertainties in the peak area or are due to the large uncertainty in the detector efficiency (only for low Z values). The first type of uncertainty can be reduced by longer measuring times or for the measurements with absorber, higher beam currents. The second type of uncertainty can only be solved by new measurements

Table 5.7: (continued)

		V-10 hay powder				A-14 milk powder			
Z		c_{ref} ppm	A %	c_{meas} ppm	B %	c_{ref} ppm	A %	c_{meas} ppm	B %
11	Na	500		855	25	4300	11	4800	22
12	Mg	1360	4.4	1690	18			1510	18
13	Al	47		318	17				
14	Si			1500	14				
15	P	2300	8.7	2090	13			9600	15
16	S			2750	14			3260	15
17	Cl			7100	13			8930	13
19	K	21000		19600	10	16600	3.6	15800	10
20	Ca	21600	2.8	19100	10	13100	8.4	12700	10
24	Cr	6.5	12	12[a]	57				
25	Mn	47		45	12				
26	Fe	185	3.5	305	8.0			24	17
28	Ni	4.0	14	4.0	32				
29	Cu	9.4	4.8	9.6	19				
30	Zn	24	13	25	14			42	13
35	Br	8	25	10.0	16			12	16
37	Rb	7.6	3.3	5.8[a]	29			21	15
38	Sr	40	8.8	46	11				

[a]This concentration is between the LOD and the LOQ (see Section 4.7)

to determine the detector efficiency with better accuracy (see Section 4.6). The only remaining large partial uncertainty is the uncertainty in the X-ray absorption coefficient. This uncertainty also has the largest influence for light elements and it can not easily be reduced.

The reduced chi-squared for all four samples is: $\chi_R^2 = 2.84$. If the three largest values of $(c_{\text{meas}} - c_{\text{ref}})/\sqrt{(s_{\text{meas}}^2 + s_{\text{ref}}^2)}$ are omitted, chi-squared becomes $\chi_R^2 = 0.79$. This value may confirm the result obtained in Section 5.4 that the uncertainty calculation overestimates the 'real' uncertainty. This is notwithstanding problems associated with this type of sample. One of these problems is the effect of small-scale sample inhomogeneities. This is a general problem for PIXE measurements. The stated minimum sample size for the IAEA samples is 100 mg. However, the amount of material detected by PIXE is much smaller, in our case typically 1-2 mg. This amount varies depending on the beam size, proton range and X-ray absorption in the sample. So, small scale inhomogeneities in an otherwise homogeneous sample can influence the results of a PIXE analysis. Another problem is the accuracy of the certified values. The certified values are averages

Table 5.8: Partial uncertainties and error propagation factors for all elements in sample H-8, horse kidney. Here, A stands for $P(c_Z, \mu_t)$ and B stands for $P(c_Z, E_{P,0})$. The uncertainties identical for all elements are $\frac{s_S}{S_t} = 3\%$, $\frac{s_\mu}{\mu_t} = 10\%$, $\frac{s_E}{E_{P,0}} = 0.6\%$, $\frac{s_\sigma}{\sigma^{ion}_{Z,K}} = 5\%$, $\frac{s_\Omega}{\Omega} \approx 5.5\%$. $P(c_Z, \sigma) = 1$ for all samples and $P(c_Z, S_t) = 1 - P(c_Z, \mu_t)$.

Z	$\frac{s_Y}{Y(X_Z)}$ %	$\frac{s_Q}{Q}$ %	$\frac{s_\varepsilon}{\varepsilon}$ %	$\frac{s_T}{T_{abs}}$ %	$\frac{s_b}{b_{Z,X}}$ %	$\frac{s_\omega}{\omega_{Z,K}}$ %	A	B	$\frac{s_{c_Z,c}}{c_Z}$ %	$\frac{s_c}{c_Z}$ %
11	1.3	1.3	18	0	0.1	4	1.00	0.14	2.7	22
12	3.9	1.3	11	0	0.1	4	1.00	< 0.01	2.7	18
15	0.4	1.3	7.4	0	0.2	4	0.94	0.53	2.7	15
16	0.4	1.3	7.1	0	0.3	4	0.88	0.79	2.6	14
17	0.3	1.3	5.1	0	0.4	4	0.80	1.09	2.4	13
19	0.2	1.3	3.7	0	0.5	4	0.57	1.78	1.7	11
20	1.3	1.3	3.4	0	0.5	4	0.50	2.04	1.4	11
25	38	1.3	1.0	0	0.2	2	0.15	3.21	0.9	39
26	2.5	1.3	0.8	0	0.2	2	0.12	3.35	0.9	9.0
29	15	1.3	0.4	0	0.2	2	0.06	3.70	0.9	17
30	4.8	1.3	0.4	0	0.2	2	0.05	3.79	0.9	9.9
34	21	0.6	0.2	4.4	0.3	1	0.02	4.08	1.0	23
35	3.2	0.6	0.2	3.6	0.3	1	0.02	4.14	1.0	9.8
37	11	0.6	0.4	2.8	0.3	1	0.01	4.25	1.0	14
48	13	0.6	6.6	1.0	0.4	0.5	< 0.01	4.69	1.0	17

of measurements based on several methods and done by several laboratories. For elements present in very small concentrations (< 1ppm), there is evidence that this method does not result in reliable concentrations [Goe 83, Byr 87]. There is however no analysis of the accuracy for the elements used for our comparison but the stated uncertainty in the reference values is smaller than the calculated uncertainty for our measurements. One other factor, which influence can hardly be underestimated, is the peak fitting procedure. This is a complicated procedure where many factors can influence the results, for instance the background determination and the overlapping of peaks. It is difficult to make an objective estimation of the uncertainty in the peak area determined in this way and it is sometimes possible to obtain larger variations in the peak area by varying parameters than is accounted for on the basis of one of the error-calculation methods described in Section 4.7.

5.8 Discussion and general conclusions

The absolute calibration method for PIXE analysis of elemental concentrations relies on a physical model of all relevant processes and knowledge of the values for all quantities needed to describe these processes. Therefore, in principle no standards for calibration are needed. The aim of this study is the evaluation of the achievable accuracy and the underlying sources of inaccuracy of the absolute calibration method for thick targets (TT-PIXE). To accomplish this aim, the absolute calibration procedure is set up taking into account the present knowledge about all relevant processes and about all relevant data. As a first step, the theory of both the physical processes and the error assessment are described in detail in Chapter 2 and Chapter 3 respectively. A complete formula is given to calculate the total uncertainty in the measured concentration. The experimental setup already present in our group has been renovated to allow the measurement of thick targets needed for the evaluation of the absolute calibration method (Chapter 4). In this section, several topics are discussed, such as the detector calibration, the comparison of the theoretical description with experimental results, the main sources of inaccuracy, and the prospects for the absolute calibration method.

The detector

An important system of the experimental setup is the detector. It is also a very complicated system that influences the analysis in several ways: through the solid angle, the detector efficiency, and through the peak shape (see the item about the X-ray yield on Page 125). Currently, the variations of the solid angle due to the dimensions of the beam spot on the target are very large. These variations can be drastically reduced by rotating the target 45° so that the target surface becomes parallel to the detector surface. This is especially important for spatially inhomogeneous targets. The detector efficiency including the solid angle has to be determined for every X-ray energy of interest. As shown in Section 4.6 and Section 5.4, the effects of the solid angle and the detector efficiency both depend on the X-ray energy. The energy dependence of the solid angle can be avoided by using a diaphragm in front of the detector. In many cases, this is a viable solution, but, since the diaphragm limits the obtainable detection limit for a given charge, this is not always possible.

The most direct method of calibrating the detector is the determination of the detector efficiency with calibrated X-ray sources. However, the number of calibrated X-ray emitting radionuclide sources, particularly below 5 keV, is limited. This makes at least some form of interpolation and even extrapolation necessary. To improve the accuracy of the inter- and extra-polation, a detector model is useful.

Measurements of external standards can be used to augment or replace the measurements with the X-ray sources. The type of target described in Section 4.6

is suitable for the measurement of the detector efficiency. The target consists of a filter paper containing a small amount of a chemical compound. The detector efficiency is calculated relative to one element in the compound. For this calculation, the production cross-sections, the matrix composition, the stopping power, and the X-ray attenuation coefficient are needed, but not the number of bombarding particles and the absolute mass of the compound. However, the uncertainty in the result is reduced because the values are only needed relative to one another. Another possibility is the use of very thin mono-elemental standards. The main problem with these standards is obtaining an accurate mass-thickness (0.1-100 $\mu g/cm^2$). Also, values of the production cross-section and of the number of bombarding particles are needed, resulting in larger uncertainties. If this standard contains the same element as the element of interest, it can even be used to eliminate (for thin targets) or reduce (for thick targets) the influence of the uncertainty in the cross section. However, this modification of the calibration method cannot be considered an absolute calibration anymore. The measurements can be used in two ways for obtaining the efficiency calibration. The first method needs no detector model, but it requires the measurement of the efficiency for all X-ray energies of interest. The second method needs a limited set of measurements and it uses a detector model to interpolate the detector efficiency.

As we have shown, in principle, it is possible to calculate the detector efficiency directly. However, a more detailed detector model is needed and, furthermore, more data about the construction and composition of all detector parts are required. Because these data are not supplied by the manufacturer with sufficient accuracy, they have to be determined. In practice, the second method is most useful. Moreover, since the detector may be susceptible to ageing, regular checks of the detector efficiency are required and this can also be accommodated by the second method. It is this method that has been used in this thesis.

Comparison of the theoretical description with the experimental results

In Section 5.3 through 5.7 the results of the theoretical description of the absolute calibration are compared with some experimental results. The value of this comparison is limited because it is difficult to obtain good reference materials for PIXE analysis with accurately known concentrations. This aspect also underlines the usefulness of absolute calibration because it can do without standards.

In general, the calculated concentrations are within the calculated uncertainties in agreement with the reference values, when no SF is involved. Exceptions are the concentrations for elements with $Z > 40$ measured without diaphragm in front of the detector, which tend to be about 10% too large, even when corrected for the energy dependence of the solid angle. This effect is probably caused by the shape of the dead layer inside the detector crystal that is assumed to be radially symmetric but that may be irregular (see Section 5.4). Therefore, within the uncertainty, no deviations from the physical model are expected.

From the experiments described in sections 5.5 and 5.6, it can be concluded that the correction for SF is necessary for targets where this process can occur. The occurrence of SF depends on c_A, c_B, and on $Z_B - Z_A$. For the elements V, Cr, and Fe in the NIST standards and in the double metal foils, the values for the SF corrections result in accurately determined concentrations. The ratio $R(SF/P)$ is, however, not large compared with uncertainties influencing the accuracy. Therfore, these measurements do not give conclusive evidence about the correctness of the SF calculation. The evidence for the heavier elements Nb, Mo, and Pd, however, is not so conclusive. A correction for SF is necessary but it seems that the calculated corrections for these elements overestimate the SF yield (see Section 5.6). Because of the large scatter of the data points, it is not clear if this is due to a shortcoming in the model or due to experimental problems or due to problems with the values for the quantities needed for the calculation.

To compare the uncertainty calculations with the experimental results, the reduced chi-squared has been calculated for all series of samples. The chi-squared values are: $\chi_R^2 = 0.23$ for the single set of metal foils, $\chi_R^2 = 2.43$ (or 1.29[1]) for the two NIST standards, and $\chi_R^2 = 2.84$ (or 0.79[1]) for the IAEA standards. The measurements of the set of metal foils have the least complications. The χ_R^2 is also smallest. From this value of χ_R^2 it can be concluded that the total uncertainty is about a factor of two overestimated. The IAEA samples are more complicated and the resulting spectrum is also more complex. The analysis is additionally complicated by the fact that the matrix composition has to be determined using NBS. Nevertheless, the results for these samples also indicate that the total uncertainty is too large, although by a smaller factor. This conclusion is not supported by the results from the NIST samples but in this case, the spectrum fitting is especially complicated. In total, it can be concluded that the uncertainty calculation is overestimated, by a factor varying from slightly larger than 1 to about 2.

The total uncertainty in the concentration, determined by absolute calibration, ranges from 8-20% under optimal conditions, depending on the element of interest. Optimal conditions mean that no extra problems arise such as a complex spectrum that complicates the peak-area determination.

Sources of inaccuracy

There are several factors that can contribute to the overestimation of the uncertainty. As explained before (see Section 5.2), the fact that not all quantities are really independent can result in an overestimation of the total uncertainty. An overestimation of the total uncertainty may also be caused by overestimation of individual uncertainties contributing to the total uncertainty. For quantities such as the stopping power, the X-ray attenuation coefficient and the ionization cross-section, the uncertainty is an average over all values of Z and the energy. This

[1] for all X-ray lines minus the three that result in the largest deviations from the reference concentrations

may lead to an overestimation of the uncertainties in individual cases. To resolve this last problem, the uncertainty estimates for these quantities have to be made for smaller intervals or even for individual values. On the other hand, underestimation may occur for the same reasons as presented above. However, in this thesis, more sources of overestimation are found then of underestimation (see also below).

It should be noted that the uncertainties can be divided in two categories: (1) Uncertainties that contribute to the uncertainty in the concentration when the method of absolute calibration is used. (2) Uncertainties that always contribute to the final uncertainty, no matter what method is used for the PIXE analysis. The first group contains the uncertainties in the stopping power, the X-ray attenuation coefficient, the production cross section, the initial proton energy, the angles θ and α, the solid angle, and the detector efficiency. It also contains the systematic parts of the uncertainties in the number of bombarding particles, and in the X-ray yield (see Section 5.2). The second group contains the matrix composition (only for thick targets) and the statistical parts of the uncertainties in the number of bombarding particles N_p, and the X-ray yield $Y(X_Z)$.

The main uncertainties are caused by the X-ray yield, the matrix composition, the X-ray attenuation coefficient, the absorber transmission and by the detector efficiency. These quantities are discussed below.

- The X-ray yield $Y(X_Z)$: This quantity is, in specific cases, very difficult to determine. Problems may be caused by a complicated background, by a complicated peak shape of the X-ray lines, by overlap of X-ray lines originating from the same element (especially for L-lines) and/or by overlap of X-ray lines from different elements. This makes it also difficult to determine a value for the uncertainty. In Section 4.7, an estimate of the uncertainty in the yield is presented based on the determination of the peak area resulting from a subtraction of a background from the total area. This is a good estimate for the statistical part of the uncertainty in the X-ray yield. For many cases, the problems described above can result in systematic errors in the X-ray yield. In these cases, the uncertainties in the peak areas are underestimated. It should be noted that these problems are not specific for the absolute calibration method but can occur for all calibration methods, although, in some cases, the systematic errors may partially cancel out.

- The matrix composition: This quantity is important for all calibration procedures although on different grounds. For the absolute calibration, it is important to know the composition for the calculation of the thick target effects. For the external-standard method, it is important to know the matrix composition to be able to choose the correct standard material. The precise matrix composition is especially important when small changes in it lead to large changes in the total stopping power S_t or the total X-ray attenuation

coefficient μ_t (see Section 2.1.1 and Section 3.3.4).

- The X-ray attenuation coefficient $\mu_t(E_{X_Z})$: Currently, this quantity has a large uncertainty of 10%. Also, the use of the summation rule (Eq. 2.14) may introduce additional errors. The validity of the summation rule needs further investigation, e.g. for C-H-O compounds. The values of the X-ray attenuation coefficient are particularly important for low X-ray energies and above absorption edges since the values in the last case are needed for the SF yield. The X-ray attenuation coefficient also is a quantity that cannot be easily eliminated by using standards. More measurements are needed to determine whether the uncertainty in this quantity is overestimated or not.

- The absorber transmission $T_{\text{abs}}(E_{X_Z})$: In addition to the X-ray attenuation coefficient, the transmission through the absorber is a large contribution to the total uncertainty for low energy X-rays. It is probable that the uncertainty in the transmission is overestimated because this uncertainty consists of two dependent uncertainties that are treated as independent uncertainties (see Section 4.5). This results in an overestimation of the total uncertainty in the concentration. Although the uncertainties for low X-ray energies are largest, the measured concentrations for the Al and Si foils are very good. This also indicates that the uncertainty in the transmission is probably too large.

- The detector efficiency $\varepsilon(E_{X_Z})$: The uncertainty for the detector efficiency for low X-ray energies can be overestimated for the same reason as for the absorber transmission. For high X-ray energies, the uncertainty in the detector efficiency increases rapidly, especially for the elements Ag and Sn. This is caused by the fact that the detector-crystal thickness is not accurately determined and we have, therefore, given a conservative estimate for the uncertainty in the thickness. Taking into account the low values for χ^2_R, indicating an overestimation of the total uncertainty, it is likely that the uncertainty in the detector thickness is a possible source of overestimation.

The first step in the further improvement of the absolute calibration method should the reduction in the uncertainties in the quantities discussed above. It should be noted that the comparison in the present studies only is for K-lines of the elements from Na to Sn. However, the L-lines are important for the analysis of heavy elements ($Z > 57$). The physical model is also valid for L-lines. However, the data base for L-lines is still not satisfactory. The main problem to be solved for the analysis of L-lines is the accuracy of the production cross-section $\sigma^{prod}_{Z,X}(E_P)$ (see Appendix A). Only after this step, it becomes useful to refine the physical model, e.g. by including more secondary processes. Another possible refinement is the incorporation of multiple scattering and/or energy straggling in the equations. All these refinements will probably only result in small improvements of the accuracy.

The improvements of the accuracy of the absolute calibration method have to be tested with measurements. For this purpose, more reliable and relevant reference materials are needed. It should be noticed that the improvement of the model and of the accuracy and precision of the available data on the one hand and the availability of more standard materials on the other hand should be done simultaneously since the results of one of these items are needed for the other items as well.

General conclusions and outlook

The evaluation of the accuracy has shown that the absolute calibration can be used in practice as a calibration method in TT-PIXE. At present, the calculated uncertainty may be quite large, but it can be reduced by determining the quantities discussed above more accurately and by removing the sources of overestimation. As pointed out in the introduction, it can be useful to use a combination of calibration methods, especially for the calibration of the detector. Sofar, for simple targets, especially thin targets, when matching standards are available, the accuracy for the calibration with standards is better than for absolute calibration. However, the availability of accurately determined standards is often a problem. Absolute calibration is a flexible method for the analysis of many different elements in many different matrices. In case of inhomogeneous targets and use of a microbeam, the use of the absolute calibration method is virtually inescapable. For this purpose, we have derived a formula for which the composition of a sample may be variable in two surface dimensions. As the accuracy of the physical quantities improves, the determination of the matrix composition of the target becomes relatively more important. The determination can be refined by an iterative approach for the elements with $Z > 10$, e.g. as applied for the NIST samples in Section 5.5. Although lighter elements cannot be determined with PIXE, they can be determined with NBS simultaneously with the PIXE measurement, as performed in Section 5.7. Although NBS is less sensitive than PIXE, this poses no problem since only the matrix elements with concentration greater than 0.5% have to be determined. A last aspect, although outside the scope of the thesis, is to what extend the targets analyzed are representative for the material to be investigated. There are many errors that may occur during target preparation, such as the introduction of contaminants, or the loss of material or specific elements, or the change the structure of the material.

References

[Ahl 75] M. Ahlberg, G. Johansson and K. Malmqvist, *Nucl. Instr. and Meth.* **131** (1975) 377.

[Ahl 77] M.S. Ahlberg, *Nucl. Instr. and Meth.* **142** (1977) 61.

[Aks 74] R. Akelsson and T.B. Johansson, *Zeit. fur Physik* **266** (1974) 245.

[Alo 86] P. Aloupogiannis, G. Robaye, I. Roelandts, G. Weber, J.M. Delbrouck-Habaru and J.P. quisefit, *Nucl. Instr. and Meth.* **B14** (1986) 297.

[Ami 93] R. Amirikas, D.N. Jamieson and S.P. Dooley, *Nucl. Instr. and Meth.* **B77** (1993) 110.

[Bak 87] C.A. Baker, C.J. Batty and S. Sakamoto, *Nucl. Instr. and Meth.* **A259** (1987) 501.

[Bam 84] W. Bambynek, material presented verbally at the International Conference on X-ray and Inner Shell Processes in Atoms, Molecules and Solids, Univ. of Leipzig (1984), the values and uncertainty estimates are published in [Joh 88].

[Bar 89] R.J. Barlow, *Statistics,* John Wiley & Sons, Chichester, England (1989).

[Bas 59] S. Bashkin, R.R. Carlson and R.A. Douglas, *Phys. Rev.* **114/6** (1959) 1553.

[Ber 90] M.J. Berger, *N.I.S.T. X-ray and Gamma-ray Attenuation Coefficients and Cross Sections Database*, National Institute of Standards and Technology, Gaithersburg, Maryland 20899, U.S.A. (1990).

[Bev 69] P.R. Bevington, *Data Reduction and Error Analysis for the Physical Sciences,* McGraw-Hill, New York (1969).

[Bir 89] J.R. Bird and J.S. Williams, *Ion beams for material analysis,* Academic press Australia (1989).

[Boz 90] M. Bozoian, K.M. Hubbard and M. Nastasi, *Nucl. Instr. and Meth.* **B51** (1990) 311.

[Bra 05] W.H. Bragg and R. Kleeman, *Philos. Mag.* **10** (1905) 318.

[Bra 79] W. Brandt and G. Lapicki, *Phys. Rev.* **A20** (1979) 465.

[Bra 81] W. Brandt and G. Lapicki, *Phys. Rev.* **A23** (1981) 1717.

[Byr 87] A.R. Byrne, C. Camara-Rica, R. Cornelis, J.J.M. de Goeij, G.V. Iyengar, G. Kirkbright, G. Knapp, R.M. Parr and M. Stoeppler, *Fresenius Z. Anal. Chem.* **326** (1987) 723.

[Cam 83] J.L. Campbell, J.A. Cookson and H. Paul, *Nucl. Instr. and Meth.* **212** (1983) 427.

[Cam 84] J.L. Campbell and J.A. Cookson, *Nucl. Instr. and Meth.* **B3** (1984) 185.

[Cam 84a] J.L. Campbell, R.G. Leigh and W.J. Teesdale, *Nucl. Instr. and Meth.* **B5** (1984) 39.

[Cam 85] J.L. Campbell, R.D. Lamb, R.G. Leigh, B.G. Nickel and J.A. Cookson, *Nucl. Instr. and Meth.* **B12** (1985) 402.

[Cam 85a] J.L. Campbell, B.M. Millman, J.A. Maxwell, A. Perujo and W.J. Teesdale, *Nucl. Instr. and Meth.* **B9** (1985) 71.

[Cam 86] J.L. Campbell, W. Maenhaut, E. Bombelka, E. Clayton, K. Malmqvist, J.A. Maxwell, J. Pallon and J. Vandenhaute, *Nucl. Instr. and Meth.* **B14** (1986) 204.

[Cam 86a] J.L. Campbell and P.L. McGhee, *Nucl. Instr. and Meth.* **A248** (1986) 393.

[Cam 88] J.L. Campbell, *Nucl. Instr. and Meth.* **B31** (1988) 518.

[Cam 89] J.L. Campbell and D. DeForge, *X-Ray Spectr.* **18** (1989) 235.

[Cam 90] J.L. Campbell, *Nucl. Instr. and Meth.* **B49** (1990) 115.

[Cam 91] J.L. Campbell and J.-X. Wang, *X-Ray Spectr.* **20** (1991) 191.

[Che 80] M.H. Chen, B. Crasemann and H. Mark, *Phys. Rev.* **A21** (1980) 436.

[Che 81] M.H. Chen, B. Crasemann and H. Mark, *Phys. Rev.* **A24** (1981) 177.

[Che 85] M.H. Chen and B. Crasemann, *Atom. Data Nucl. Data Tables* **33** (1985) 217.

[Che 89] M.H. Chen and B. Crasemann, *Atom. Data Nucl. Data Tables* **41** (1989) 257.

[Chu 78] W.-K. Chu, J.W. Mayer and M.-A. Nicolet, *Backscatering spectrometry,* Academic Press, New York (1978).

[Cla 81] E. Clayton, *Nucl. Instr. and Meth.* **191** (1981) 567.

[Coe 90] G. Coenders, *Internal report E.U.T.,***VDF/NK 90-23** (1990).

[Coh 80] D.D. Cohen, *Nucl. Instr. and Meth.* **178** (1980) 481.

[Coh 82] D.D. Cohen, *Nucl. Instr. and Meth.* **193** (1982) 15.

[Coh 85] D.D. Cohen and M. Harrigan, *Atom. Data Nucl. Data Tables* **33** (1985) 255.

[Coh 86] D.D. Cohen and M. Harrigan, *Atom. Data Nucl. Data Tables* **34** (1986) 393.

[Coh 87] D.D. Cohen and E. Clayton, *Nucl. Instr. and Meth.* **B22** (1987) 59.

[Coh 87a] D.D. Cohen, *Nucl. Instr. and Meth.* **B22** (1987) 55.

[Coh 89] D.D. Cohen, *Atom. Data Nucl. Data Tables* **41** (1989) 287.

[Coh 90] D.D. Cohen, *Nucl. Instr. and Meth.* **B49** (1990) 1.

[Com 35] A.H. Compton and S.K. Allison, *X-rays in Theory and Experiment*, D. Van Nostrand, Princeton, N.Y. (1935).

[Cre 87] D.C. Creagh, *Nucl. Instr. and Meth.* **A255** (1987) 1.

[Cre 91] M.P. Creusen, *Internal report E.U.T.*,**VDF/NK 91-33** (1991).

[Doo 85] L.R. Doolittle, *Nucl. Instr. and Meth.* **B9** (1985) 344.

[Doo 86] L.R. Doolittle, *Nucl. Instr. and Meth.* **B15** (1986) 227.

[Esp 77] P. van Espen, H. Nullens and F. Adams, *Nucl. Instr. and Meth.* **142** (1977) 243.

[Goe 83] J.J.M. de Goeij, L. Kosta, A.R. Byrne and J. Kučera, *Anal. Chim. Acta* **146** (1983) 161.

[Goc 83] M. Goclowski, M. Jaskóla and L. Zemlo, *Nucl. Instr. and Meth.* **204** (1983) 553.

[Gri 93] G.W. Grime and F. Watt, *Nucl. Instr. and Meth.* **B75** (1993) 495.

[Ina 87] Y. Inagaki, K. Shima and H. Maezawa, *Nucl. Instr. and Meth.* **B27** (1987) 353.

[Han 73] J.S. Hansen, J.C. McGeorge, D. Nix, W.D. Schmidt-Ott, I. Unus and R.W. Fink, *Nucl. Instr. and Meth.* **106** (1973) 365.

[Har 62] R.W. Harris, G.C. Phillips and C. Miller Jones, *Nucl. Phys.* **38** (1962) 259.

[He 90] T. He, R.P. Gardner and K. Verghese, *Nucl. Instr. and Meth.* **A299** (1990) 354.

[Hey 63] G. Heymann and R.L. Keizer, *Nucl. Instr. and Meth.* **24** (1963) 125.

[Hol 72] M.J. Hollis, *Nucl. Instr. and Meth.* **103** (1972) 337.

[Jac 53] H.L. Jackson, A.I. Galonsky, F.J. Eppling, R.W. Hill, E. Goldberg and J.R. Cameron, *Phys. Rev.* **89/2** (1953) 365.

[Jak 72] J.M. Jaklevic, F.S. Goulding and D.A. Landis, *IEEE Trans. Nucl. Sci.* **19** (1972) 392.

[Jan 82] J.F. Janni, *Atom. Data Nucl. Data Tables* **27** (1982) 147.

[Joh 76] S.A.E. Johansson and T.B. Johansson, *Nucl. Instr. and Meth.* **137** (1976) 473.

[Joh 88] S.A.E. Johansson and J.L. Campbell, *PIXE: A Novel Technique for Elemental Analysis*, John Wiley & Sons, Chichester (1988).

[Joh 92] S.A.E. Johansson, *Int. J. of PIXE* **2** (1992) 33.

[Kiv 80] H. Kivits, *Thesis*, E.U.T. 1980.

[Kof 91] E.N. Koffeman, *Internal report E.U.T.*,**VDF/NK 91-37** (1991).

[Kor 92] E.W. Korevaar, *Internal report E.U.T.*,**VDF/NK 92-20** (1992).

[Kno 79] G.F. Knoll, *Radiation detection and measurement,* John Wiley and sons, New York (1979).

[Kra 79] M.O. Krause, *J. Phys. Chem. Ref. Data* **8** (1979) 307.

[Lap 87] G. Lapicki, *J. Phys.* **B20** (1987) L633.

[Lau 66] T. Lauritsen and T. Ajzenberg-Selove, *Nucl. Phys.* **78** (1966) 1.

[Ler 77] J. Leroux and T.P. Thinh, *Revised Tables of X-Ray Mass Attenuation Coefficients*, Corp. Scientifique Claisse Inc., Quebec (1977).

[Mae 86] W. Maenhaut and J. Vandenhaute, *Bull. Soc. Chim. Belg.* **95** (1986) 407.

[Mai 90] Th. Maisch, V. Schüle, R. Günzler, P. Oberschachtsiek, M. Weiser, S. Jans, K. Izsak and S. Kalbitzer *Nucl. Instr. and Meth.* **B50** (1990) 1.

[Max 89] J.A. Maxwell, J.L. Campbell and W.J. Teesdale, *Nucl. Instr. and Meth.* **B43** (1989) 218.

[Nig 59] B.P. Nigam, M.K. Sundaresan and T.-Y. Wu, *Phys. Rev.* **115** (1959) 491.

[Orl 90] I. Orlić, J. Makjanić, G.H.J. Tros and R.D. Vis, *Nucl. Instr. and Meth.* **B49** (1990) 166.

[Ott 75] G. Ottaviani, C. Canali and A. Alberigi Quaranta, *IEEE Trans. Nucl. Sci.*, **NS 19, 4** (1975) 9.

[Paj 89] M. Pajek, A.P. Kobzev, R. Sandrik, R.A. Ilkhamov and S.H. Khusmurodov, *Nucl. Instr. and Meth.* **B42** (1989) 346.

[Pau 86] H. Paul and J. Muhr, *Phys. Rep.* **135** (1986) 47.

[Pau 89] H. Paul and J. Sacher, *Atom. Data Nucl. Data Tables* **42** (1989) 105.

[Pau 91] H. Paul, D.Semrad and A. Seilinger, *Nucl. Instr. and Meth.* **B61** (1991) 261

[Per 87] A. Perujo, J.A. Maxwell, W.J. Teesdale and J.L. Campbell, *J. Phys.* **B20** (1987) 4973.

[Pol 69] A.R. Poletti,J.A. Becker and R.E. McDonald, *Phys. Rev.* **182** (1969) 1054.

[Ree 72] S.J.B. Reed and N.G. Ware, *J. Phys.* **E5** (1972) 582.

[Reu 75] W. Reuter, A. Lurio, F. Cardone and J.F. Ziegler, *J. Appl. Phys.* **46** (1975) 3194.

[Rin 93] A. Rindby, *X-Ray Spectr.* **22** (1993) 187.

[Sal 74] S.I. Salem, S.L. Panossian and R.A. Krause, *Atom. Data Nucl. Data Tables* **14** (1974) 91.

[Sco 74] J.H. Scofield, *Phys. Rev.* **A9** (1974) 1041.

[Sco 74a] J.H. Scofield, *Atom. Data Nucl. Data Tables* **14** (1974) 121.

[Sco 74b] J.H. Scofield, *Phys. Rev.* **A10** (1974) 1507.

[Shi 79] K. Shima, *Nucl. Instr. and Meth.* **165** (1979) 21.

[Shi 83] K. Shima, S. Nagai, T. Mikumo and S. Yasumi, *Nucl. Instr. and Meth.* **217** (1983) 515.

[Sin 90] S. Singh, D. Mehta, R.R. Garg, S. Kumar, M.L. Garg, N. Singh, P.C. Mangal, J.H. Hubbell and P.N. Trehan, *Nucl. Instr. and Meth.* **B51** (1990) 5.

[Smi 84] Ž. Šmit, M. Budnar, V. Cindro, V. Ramšak and M. Ravnikar, *Nucl. Instr. and Meth.* **B4** (1984) 114.

[Smi 85] Ž. Šmit, M. Budnar, V. Cindro, M. Ravnikar and V. Ramšak, *Nucl. Instr. and Meth.* **228** (1985) 482.

[Smy 64] R. Smythe, *Rev. Sci. Instr.* **35** (1964) 1197.

[Squ 56] G.L. Squires, C.K. Bockelman and W.W. Buechner, *Phys. Rev.* **104** (1956) 413.

[Sta 86] C. van der Stap, *Thesis,* Vrije Universiteit Amsterdam (1986).

[Sto 70] E. Storm and H.I. Israel, *Atom. Data Nucl. Data Tables* **A7** (1970) 565.

[Thi 79] T.P. Thinh and J. Leroux, *X-Ray Spectr.* **8** (1979) 85.

[Tin 91] P.A.J. Tinnemans, *Internal report E.U.T.,*(1991).

[Thw 83] D.I. Thwaites, *Radiat. Res.* **95** (1983) 495.

[Thw 85] D.I. Thwaites, *Nucl. Instr. and Meth.* **B12** (1985) 84.

[Thw 87] D.I. Thwaites, *Nucl. Instr. and Meth.* **B27** (1987) 293.

[Ude 92] M.A. van Uden, *Internal report E.U.T.,* **VDF/NK 92-21** (1992).

[Uzu 93] N. Uzunov, F. Munnik and M.J.A. de Voigt, *Nucl. Instr. and Meth.* **B82** (1993) 180.

[Ver 92] B.J. Verhaar, *private communication,* Eindhoven Univ. of Tech., (1992).

[Viz 90] G. Vizkelethy, *Nucl. Instr. and Meth.* **B45** (1990) 1.

[Wat 87] U. Wätjen, *Nucl. Instr. and Meth.* **B22** (1987) 29.

[Wil 88] J.P. Willes, *Nucl. Instr. and Meth.* **B35** (1988) 378.

[Wil 91] M.F.C. Willemsen and A.E.T. Kuiper, *Nucl. Instr. and Meth.* **B61** (1991) 213.

[Win 91] Y.J.E. Wintraecken, *Internal report E.U.T.,* **VDF/NK 91-35** (1991).

[Zen 87] X. Zeng and X. Li, *Nucl. Instr. and Meth.* **B22** (1987) 99.

[Zie 85] J.F. Ziegler, J.P. Biersack and U. Littmark, *The Stopping and Range of Ions in Solids, Vol 1*, Pergamon Press, New York (1985).

[Zie 88] J.F. Ziegler and J.M. Manoyan, *Nucl. Instr. and Meth.* **B35** (1988) 215.

A L-lines

In this appendix, the theory for the L-shell production cross-section is presented, together with the extra data for L-lines needed for the data base.

Theoretical description

For higher atomic shells, the formula for the production cross section becomes more complicated since they have more subshells. The L-shell, for example, has three subshells and if a vacancy is created in one subshell, there is a possibility of a non-radiative transfer to a higher subshell. This process is called a Coster-Kronig transition, denoted by its probability f^s_{ij}, with s the main shell and i, j the subshells between which the transition takes place (from i to j). If there is a vacancy created in a subshell, there are three processes by which the vacancy may be filled by an electron from a higher (sub)shell. The first process is the Coster-Kronig transition which is radiationless, the second process results in the emission of an X-ray and the third in the emission of an Auger electron. The probability of all three processes f^L_{ij}, $\omega_{Z,Li}$ and $a_{Z,Li}$ summed must be 1.

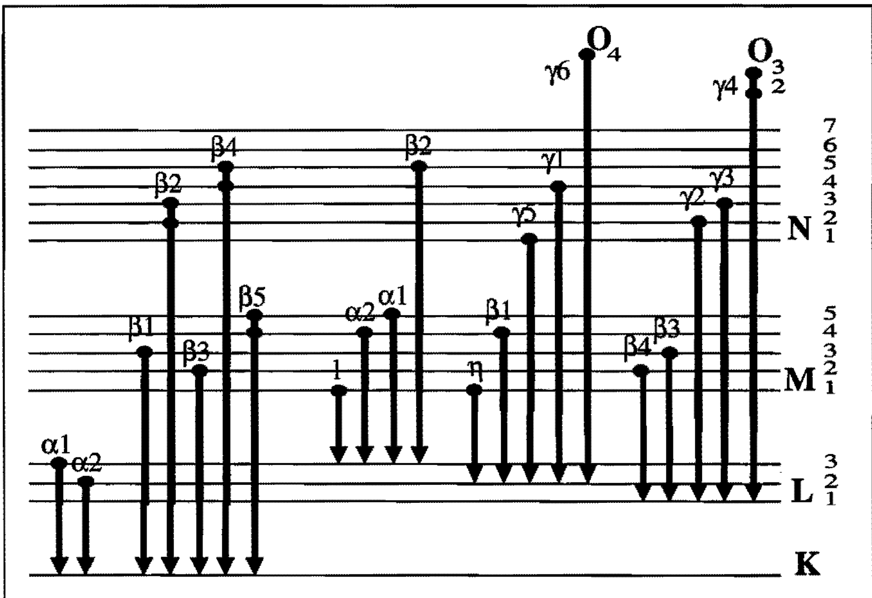

Fig. A.1: Diagram showing the main K- and L-shell transitions. The nomenclature for the transitions is the Siegbahn notation.

For all three subshells of the L-shell, there are several lines X_Z, the main

transitions are presented in Fig. A.1. The production cross section for each of the three subshells is given by:

$$\sigma^{prod}_{Z,X(L1)}(E_P) = \sigma^{ion}_{Z,L1}(E_P)\omega_{Z,L1}b_{Z,X(L1)}. \tag{A.1}$$

$$\sigma^{prod}_{Z,X(L2)}(E_P) = \left\{\sigma^{ion}_{Z,L1}(E_P)f^L_{1,2} + \sigma^{ion}_{Z,L2}(E_P)\right\}\omega_{Z,L2}b_{Z,X(L2)} \tag{A.2}$$

$$\begin{aligned}\sigma^{prod}_{Z,X(L3)}(E_P) &= \left\{\sigma^{ion}_{Z,L1}(E_P)[f^L_{1,2}f^L_{2,3} + f^L_{1,3} + f^L_{1,3}{}']\right.\\ &\quad \left. + \sigma^{ion}_{Z,L2}(E_P)f^L_{2,3} + \sigma^{ion}_{Z,L3}(E_P)\right\}\omega_{Z,L3}b_{Z,X(L3)}\end{aligned} \tag{A.3}$$

Here, $f^L_{1,3}{}'$ is a radiative transition from the L1 to the L3 subshell. In contrast to the non-radiative Coster-Kronig transition, the radiative transitions within the L-shell are negligible, except for the L1 to L3 transition. The values for $\sigma^{ion}_{Z,Li}(E_P)$, $\omega_{Z,Li}$, $b_{Z,X(Li)}$ and $f^L_{i,j}$ are generally not so well known as the values for the K-shell (see also Section 2.3). The M-shell has five subshells and here the situation becomes even more complicated than for the L-shell. Furthermore, there hardly is any data available for $\sigma^{ion}_{Z,Mi}(E_P)$, $\omega_{Z,Mi}$, $b_{Z,X(Mi)}$ and $f^M_{i,j}$. This means that the M-shell X-rays are not useful for quantitative analysis using PIXE.

L-shell ionization cross-section

The L-shell ionization cross section has to be calculated for three subshells separately. Chen and Crasemann have calculated the L-subshell ionization cross sections. The tabulations of Cohen and Harrigan are also available for the L-shell. The data of Chen and Crasemann is fitted by Maxwell *et al.* [Max 89] in the same way as for the K-shell for the atomic numbers ranging from 22 to 92 (see Section 2.3.3). It is difficult to make a choice between the schemes of Chen and Crasemann, and of Cohen and Harrigan because of the complexity of the production cross section for the L-shell X-ray lines (see eqs. A.1, A.2 and A.3). This complexity makes a comparison between the calculated ionization cross section and the experimentally determined production cross section very difficult. This is due to the necessary knowledge of the values for the Coster-Kronig transition, the fluorescence yield and the branching ratio for the calculation. In practice, it is only possible to compare the calculated production cross section with the measured production cross section. It also follows that it is difficult to give an error estimate for the values of the individual quantities in the formula for the L-shell production cross section. A discussion for the total production cross section is given below after all the necessary quantities are described. For the ionization cross section, the fits of Maxwell *et al.* are used when possible as in the case of the K-shell. For other energy and Z ranges, calculations of Cohen and Harrigan are used.

Branching ratio

For the L-shell, many more transitions are possible, so there are more branching ratios. The semi-empirical data base of Salem *et al.* is also available for the L-shell as well as for the K-shell. The estimated uncertainties range from 2 to 8%. Scofield has performed his Hartree-Slater [Sco 74] and Hartree-Fock [Sco 74b] calculations for the L-shell. The Hartree-Fock calculations were only carried out for 21 elements ranging from $Z = 18$ to $Z = 94$. The difference between the two theories is less than the spread in the experimental data. On the basis of the K-shell data, Campbell and Wang [Cam 89] concluded that the Hartree-Fock calculations give the best results. Therefore, they have interpolated the values of [Sco 74b] using a comparison with the Hartree-Slater values that were calculated for $5 \leq Z \leq 104$. There is also a data base available from the analysis program AXIL of unknown origin. In Fig. A.2, a comparison is made between the data bases described above. It is clear from this figure that there are large differences between the data bases of Campbell *et al.* and Salem *et al.* , exceeding the stated uncertainties for the values of Salem. The data base used in the program AXIL seems to be based on the values of Campbell *et al.* , although there are slight differences. The differences for the $L_{\beta 2,15}/L\alpha 1$ ratio for $Z \leq 52$ can be due to the fact that the there are no values for the $L_{\beta 15}$ line available in the AXIL data base. The line intensities are, however, normalized on 1.

At the moment, these values are in use for our data base because the values are nearly complete and normalized. Another advantage is that they give more consistent results since the same values are used for both the program AXIL, to determine the peak areas, as well as for the final calculations of the concentrations.

Fluorescence Yield and Coster-Kronig Transition Rate

For the L-shell, there are three subshells and thus three $\omega_{Z,Li}$ $(i = 1,2,3)$ and five Coster-Kronig transition rates f_{ij}^L. Many publications are concerned with the average L-shell fluorescence yield, which is not a useful quantity for the data base. One complete semi-empirical compilation of both subshell fluorescence yields and Coster-Kronig transition rates is the compilation of Krause [Kra 79] for $12 \leq Z \leq 110$. Unfortunately, the estimated uncertainties are rather large; for $\omega_{Z,Li}$, 10-30% for Z is 12-50 and 3-20% for Z larger than 50 and for f_{ij}^L, 5-20% for all Z. The large uncertainties for low Z values are mainly due to a lack of experimental data. The values of f_{ij}^L change suddenly as a function of Z for the L1- and L2-subshells because of thresholds for various Coster-Kronig transitions. Near these jumps, the uncertainty in f_{ij}^L may be even larger. Chen *et al.* have also done relativistic Dirac Hartree Slater calculations for the L-shell for 25 elements with $18 \leq Z \leq 100$ [Che 81]. Campbell [Cam 88] has made interpolation schemes to obtain values for all Z. At the moment, the data of Krause is in use but it seems recommendable to use the interpolation schemes of Campbell, see discussion below.

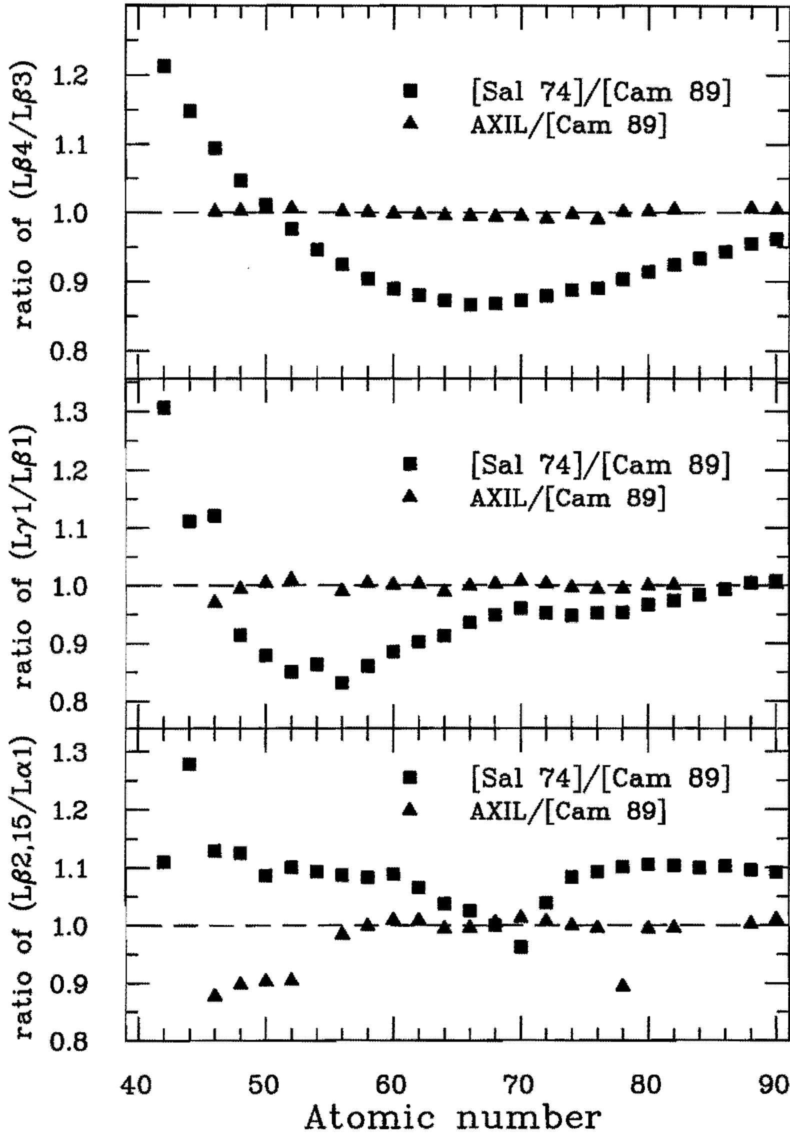

Fig. A.2: Figure of selected line intensity ratios from the data base of Campbell *et al.* [Cam 89] and from AXIL divided by the theoretical Hartree-Fock intensity ratio of Scofield [Sco 74b]. The top graph is for a ratio of L1 lines, the middle graph is for L2 lines and the bottom graph is for L3 lines.

Discussion

In total, there are two complete data bases for the production cross section. Both rely heavily on theoretical calculations mainly due to a lack of good experimental data for all elements. One data base [Coh 86, Coh 87] contains the ionization cross sections of Cohen and Harrigan [Coh 85], the fluorescence yields and Coster-Kronig transition probabilities of Krause [Kra 79] and the branching ratios of Salem *et al.* [Sal 74]. The other one [Cam 88] contains the interpolated ionization cross sections of Chen and Crasemann [Che 85, Max 89], the interpolation schemes for the fluorescence yields and Coster-Kronig transition probabilities [Cam 88, Che 81] and the interpolated branching ratios of Scofield [Cam 88, Sco 74b]. Campbell [Cam 88] has made a comparison of the two data bases with experimental data by studying the intensity ratios of major L X-ray lines for a few selected materials. He has concluded that the scheme of Chen and Crasemann is slightly better than that of Cohen and Harrigan. A comparison of the average L-shell fluorescence yield by Singh *et al.* [Sin 90] has also led to the conclusion that the calculations of Chen *et al.* [Che 81] are in good agreement with experimental data, better than the calculations of Cohen [Coh 87a].

B Calculations for the SF yield

In this appendix, some of the calculations for the SF yield in Section 2.2 are explained in more detail.

The threefold integral Eq. 2.38 can be simplified and one integral can be solved analytically. These calculations are performed in the following points.

1. First a new variable can be introduced:

$$f_A(E_{X_A}, E_{X_B}) = \frac{1}{2}\tau_{A,tot}(E_{X_B})(1 - \frac{1}{r_{A,K}})\omega_{A,K}b_{A,X}c_A\varepsilon_{abs}(E_{X_A}) \quad \text{(B.1)}$$

2. The integral over β can be rewritten. In Eq. 2.38, there are two integrals over β. The first one is written as

$$\int_0^{\pi/2} d\beta \, \frac{\sin\beta}{\cos\beta} \exp\left\{-\frac{C}{\cos\beta}\right\} = \int_1^0 d\cos\beta \, \frac{-1}{\cos\beta} \exp\left\{-\frac{C}{\cos\beta}\right\} \quad \text{(B.2)}$$

with $C = \frac{\mu_t(E_{X_B})}{\rho_S}\rho_S(L-x)$, $(C > 0)$. It now is possible to make the transformation $y = 1/\cos\beta$ and $1/\cos\beta d\cos\beta = -1/y dy$:

$$\int_1^0 d\cos\beta \, \frac{-1}{\cos\beta} \exp\{-\frac{C}{\cos\beta}\} = \int_1^\infty dy \, \frac{1}{y} \exp\{-Cy\} \quad \text{(B.3)}$$

The second integral over β can be treated similarly. The first step is the transformation $\beta' = \pi - \beta$.

$$\int_{\pi/2}^{\pi} d\beta \, \frac{\sin\beta}{\cos(\pi-\beta)} \exp\left\{\frac{-C}{\cos(\pi-\beta)}\right\} = \int_{\pi/2}^{0} -d\beta' \, \frac{\sin(\pi-\beta')}{\cos\beta'} \exp\left\{\frac{-C}{\cos\beta'}\right\}$$
$$= \int_0^{\pi/2} d\beta' \, \frac{\sin\beta'}{\cos\beta'} \exp\left\{\frac{-C}{\cos\beta'}\right\} = \int_1^\infty dy \, \frac{1}{y} \exp\{-Cy\} \quad \text{(B.4)}$$

with $C = \frac{\mu_t(E_{X_B})}{\rho_S}\rho_S(x-L)$, $(C > 0)$.

3. The integration order is to integrate first over the new variable y than over x and finally over L. This order can be changed to first x than L and than y because L, y and x are independent. This step and the above mentioned points change Eq. 2.38 to

$$Y_{SF}(X_A, X_B) =$$
$$f_A(E_{X_A}, E_{X_B}) \int_1^\infty dy \, \frac{1}{y} \int_0^t dL \, \exp\left\{-\frac{\mu_t(E_{X_A})}{\rho_S}\rho_S \frac{L}{\cos\theta}\right\}$$

$$\left(\int_0^L dx\, \frac{dN_B(x)}{dx} \exp\left\{-\frac{\mu_t(E_{X_B})}{\rho_S}\rho_S(L-x)y\right\}\right.$$
$$\left.+\int_L^t dx\, \frac{dN_B(x)}{dx} \exp\left\{-\frac{\mu_t(E_{X_B})}{\rho_S}\rho_S(x-L)y\right\}\right) \tag{B.5}$$

By using the absolute value $|L-x|$ instead of $(L-x)$ and $(x-L)$, the sommation of two integrals over x can be replaced by one integral over the full depth of 0 to t. It then is possible to change the integration order between L and x. The substition of E_P for x can be made using eqs. 2.4 and 2.5. Finally, the integral over L with the absolute value again can be replaced by two integrals and the integration order between y and E_P changed.

$$\begin{aligned}
&Y_{SF}(X_A, X_B)\\
&= f_A(E_{X_A}, E_{X_B}) \int_1^\infty dy\, \frac{1}{y} \int_0^t dL\, \exp\left\{-\frac{\mu_t(E_{X_A})}{\rho_S}\rho_S\frac{L}{\cos\theta}\right\}\\
&\quad \int_0^t dx\, \frac{dN_B(x)}{dx} \exp\left\{-\frac{\mu_t(E_{X_B})}{\rho_S}\rho_S|L-x|y\right\}\\
&= f_A(E_{X_A}, E_{X_B}) \int_1^\infty dy\, \frac{1}{y} \int_0^t dx\, \frac{dN_B(x)}{dx}\\
&\quad \int_0^t dL\, \exp\left\{-\frac{\mu_t(E_{X_A})}{\rho_S}\rho_S\frac{L}{\cos\theta}\right\} \exp\left\{-\frac{\mu_t(E_{X_B})}{\rho_S}\rho_S|L-x|y\right\}\\
&= f_A(E_{X_A}, E_{X_B}) \int_{E_{P,0}}^{E_{P,f}} dE_P\, \frac{dN_B(E_P)}{dE_P} \int_1^\infty dy\, \frac{1}{y}\\
&\quad \left(\int_0^x dL\, \exp\left\{-\frac{\mu_t(E_{X_A})}{\rho_S}\rho_S\frac{L}{\cos\theta}\right\} \exp\left\{-\frac{\mu_t(E_{X_B})}{\rho_S}\rho_S(x-L)y\right\}\right.\\
&\quad + \int_x^t dL\, \exp\left\{-\frac{\mu_t(E_{X_A})}{\rho_S}\rho_S\frac{L}{\cos\theta}\right\}\\
&\quad \left.\exp\left\{-\frac{\mu_t(E_{X_B})}{\rho_S}\rho_S(L-x)y\right\}\right)
\end{aligned} \tag{B.6}$$

with x given by Eq. 2.5 and

$$\frac{dN_B(E_P)}{dE_P} = N_P \frac{N_{Av}}{M_B} c_B \sigma_{B,X}^{prod}(E_P) \frac{1}{S_t(E_P)} \tag{B.7}$$

4. The integral over L in Eq. B.6 can be solved.

$$\begin{aligned}
&\int_0^x dL\, \exp\{(-p+qy)L - qxy\} + \int_x^t dL\, \exp\{(-p-qy)L + qxy\}\\
&= \left.\frac{\exp\{(-p+qy)L-qxy\}}{-p+qy}\right|_0^x + \left.\frac{\exp\{(-p-qy)L+qxy\}}{-p-qy}\right|_x^t\\
&= \frac{\exp\{-px\}}{-p+qy} - \frac{\exp\{-qxy\}}{-p+qy} - \frac{\exp\{-px\}}{-p-qy} + \frac{\exp\{-q(t-x)y-pt\}}{-p-qy}
\end{aligned} \tag{B.8}$$

with

$$p = \frac{\mu_t(E_{X_A})}{\rho_S} \frac{\rho_S}{\cos\theta} \quad \text{and} \quad q = \frac{\mu_t(E_{X_B})}{\rho_S} \rho_S \tag{B.9}$$

5. Eq. B.8 has to be integrated over y. The first and third term in Eq. B.8 can be solved analytically.

$$\int_1^\infty dy \, \frac{1}{y} \frac{\exp\{-px\}}{-p+qy} = \frac{\exp\{-px\}}{p} \{\ln q - \ln|-p+q|\} \tag{B.10}$$

and

$$\int_1^\infty dy \, \frac{-1}{y} \frac{\exp\{-px\}}{-p-qy} = \frac{\exp\{-px\}}{p} \{-\ln q + \ln|p+q|\} \tag{B.11}$$

Putting all points together, we can arrive at a final formula for the SF yield (Eq. 2.39).

The last term in Eq. 2.42 can give problems when it has to be integrated numerically because the function of y, which has to be integrated, contains an asymptote between the integration bounderies 1 and ∞ when $p > q$. A solution to this problem of numerical integration is given by Verhaar [Ver 92]. The first step is to split the integral in a symmetric interval around the asymptote $y = p/q$ and the rest of the original interval. The new boundery is $y = p/q + (p/q - 1) = 2p/q - 1$.

$$\int_1^\infty \frac{\exp(-qxy)}{y(p-qy)} dy = \int_1^{2p/q-1} \frac{\exp(-qxy)}{y(p-qy)} dy + \int_{2p/q-1}^\infty \frac{\exp(-qxy)}{y(p-qy)} dy \tag{B.12}$$

The integral over the second interval can be solved numerically. To solve the integral over the first interval, we subtract an integration over an extra function. The integration over this extra function has to be zero. This can be done by taking a rotation-symmetrical function around the asymptote $y = p/q$. The function is made by taken the zeroth order Taylor expansion of $\exp(-qxy)/y$ around $y = p/q$ which is $q/\exp(-px)$ and multiplying it with $1/(p - qy)$.

$$\int_1^{p/q} \frac{\exp(-px)}{p/q(p-qy)} dy = -\int_{p/q}^{2p/q-1} \frac{\exp(-px)}{p/q(p-qy)} dy \tag{B.13}$$

Taking both integrals together results in an integral that can be solved numerically.

$$\begin{aligned}\int_1^{2p/q-1} \frac{\exp(-qxy)}{y(p-qy)} dy - 0 &= \int_1^{2p/q-1} \frac{\exp(-qxy)}{y(p-qy)} dy - \int_1^{2p/q-1} \frac{\exp(-px)}{p/q(p-qy)} dy \\ = \quad & \int_1^{p/q-1} \left\{ \frac{\exp(-qxy)}{y} - \frac{\exp(-px)}{p/q} \right\} \frac{1}{2(p-qy)} dy \end{aligned} \tag{B.14}$$

It can be seen that this last integration does not contain an asymptote by making a Taylor expansion of $\exp(-qxy)$ around $y = p/q$.

C Derivation of Propagation Factors for the Primary Yield

The propagation factors for the various parameters in the formula of the primary yield are given in Section 3.3. The calculations are carried out using Eq. 3.4. Here a derivation of these results is given.

Eq. 3.4 is based on the following relation:

$$\left(\frac{s_{Y,x}}{Y(x)}\right)(x_0) \approx \frac{Y(x_0+\delta)-Y(x_0-\delta)}{2Y(x_0)\delta/x_0}\frac{s_x(x_0)}{x_0}. \tag{C.1}$$

For the derivations, Eq. 2.15 is used in a simplified form, without the subscripts P for E_P, t for S_t and μ_t and S for T_S :

$$Y = \text{const.} \int \frac{\sigma T}{S} dE. \tag{C.2}$$

First the formula for the cross section (Eq. 3.6) is discussed. In a strict way, Eq. C.1 cannot be used for the cross section because the cross section is integrated over the proton energy E. To be able to use Eq. C.1, we have to assume that $\frac{s_\sigma}{\sigma}$ and $\frac{\delta_\sigma}{\sigma}$ are constant for all proton energies E_P, as stated in Section 3.3.2. Substituting Eq. C.2 in Eq. C.1 with σ as parameter x gives:

$$\frac{s_{Y,\sigma}}{Y(\sigma)} \approx \frac{\text{const.} \int \frac{(\sigma+\delta)T}{S}dE - \text{const.} \int \frac{(\sigma-\delta)T}{S}dE}{2\frac{\delta}{\sigma}\text{const.} \int \frac{\sigma T}{S}dE}\frac{s_\sigma}{\sigma}. \tag{C.3}$$

Eq. C.3 can be rewritten with the same assumption to

$$P(Y(X_Z),\sigma) = \frac{s_{Y,\sigma}}{Y(\sigma)}/\frac{s_\sigma}{\sigma} \approx \frac{2\int \frac{\delta T}{S}dE}{2\int \frac{\delta}{\sigma}\frac{\sigma T}{S}dE} = 1 \tag{C.4}$$

This result is given in Eq. 3.6.

Next, we shall discuss the formula for the propagation factor for the stopping power, Eq. 3.9. Now, x must be replaced by S. $\frac{s_S}{S}$ and $\frac{\delta_S}{S}$ have to be constant for all proton energies E_P, because S is again integrated over E_P. Let $f_S^\pm$ be $1 \pm \delta_S/S$ then $f_S^\pm$ also is independent of E_P and

$$Y(S\pm\delta_S) = Y(Sf_S^\pm) = \text{const.} \int \frac{\sigma T^{(1/f_S^\pm)}}{Sf_S^\pm}dE. \tag{C.5}$$

The transmission T to the power $1/f_S^\pm$ follows from Eq. 2.16, $T = \exp(\text{const.} \int \frac{dE}{S})$. Eq. C.5 can be substituted in Eq. C.1:

$$\frac{s_{Y,S}}{Y(S)} \approx \frac{\text{const.} \int \frac{\sigma}{S}\left\{\frac{T^{(1/f_S^+)}}{f_S^+} - \frac{T^{(1/f_S^-)}}{f_S^-}\right\}dE}{2\frac{\delta_S}{S}\text{const.} \int \frac{\sigma T}{S}dE}\frac{s_S}{S} \tag{C.6}$$

$T^{(1/f_S^{\pm})}$ can be approximated by a first order Taylor expansion round $f_S^{\pm} = 1$ since $\frac{\delta_S}{S}$ is small:

$$T^{(1/f_S^{\pm})} \approx T + (f_S^{\pm} - 1)\left(\frac{-1}{(f_S^{\pm})^2 T^{(1/f_S^{\pm})} \ln T}\right)_{f_S^{\pm}=1} . \tag{C.7}$$

This can be used to rewrite part of Eq. C.6:

$$\left\{\frac{T^{(1/f_S^{+})}}{f_S^{+}} - \frac{T^{(1/f_S^{-})}}{f_S^{-}}\right\} \approx \left(\frac{1}{f_S^{+}} - \frac{1}{f_S^{-}}\right)(T + T\ln T). \tag{C.8}$$

In good approximation it can be written that

$$\left(\frac{1}{f_S^{+}} - \frac{1}{f_S^{-}}\right) = -2\frac{\frac{\delta_S}{S}}{1 - (\frac{\delta_S}{S})^2} \approx -2\frac{\delta_S}{S} \tag{C.9}$$

Substituting Eq. C.9 in Eq. C.8 and Eq. C.8 in Eq. C.6 results in

$$\frac{s_{Y,S}}{Y(S)} \approx -\frac{\int \frac{\sigma}{S} T(1 + \ln T) dE}{\int \frac{\sigma T}{S} dE} \frac{s_S}{S} \tag{C.10}$$

which is the result given in Eq. 3.9.

For the X-ray attenuation coefficient, the derivation of Eq. 3.10 is easier since $\partial Y/\partial \mu_t$ can be calculated analytically. It also is more accurate because μ_t does not depend on E_P.

$$\begin{aligned} \partial Y/\partial \mu_t &= \partial\left(\text{const.} \int \frac{\sigma \exp\{\text{const.}\ \mu_t \int \frac{dE}{S}\}}{S} dE\right) \partial \mu_t \\ &= \text{const.} \int \frac{\sigma T \frac{\ln T}{\mu_t}}{S} dE. \end{aligned} \tag{C.11}$$

This result can be used directly to give the partial error in the yield according to $s_{Y,\mu_t} = (\partial Y/\partial \mu_t) s_{\mu_t}$:

$$\frac{s_{Y,\mu_t}}{Y(\mu_t)} = \frac{\int \frac{\sigma}{S} T \ln T dE}{\int \frac{\sigma T}{S} dE} \frac{s_\mu}{\mu}. \tag{C.12}$$

The propagation factor for the matrix composition can be derived from the calculation of s_S/S and s_μ/μ caused by the error in the matrix concentrations and subsequently using the propagation factor for these errors, as described in Subsection 3.3.3. If there are n matrix elements, there are only $n-1$ independent concentration variables since the sum of the concentrations must be one. For a two element matrix $A_c B_{1-c}$, the following formulas can be used for the errors in the stopping power and in the X-ray attenuation coefficient:

$$s_{S_t}^2 = \sum_{i=A,B} (c_i s_{S_i})^2 + (S_A - S_B)^2 s_c^2 \tag{C.13}$$

$$s_{\mu_t}^2 = \sum_{i=A,B} (c_i s_{\mu_i})^2 + (\mu_A - \mu_B)^2 s_c^2. \tag{C.14}$$

With c_A is c, c_B is $1 - c$ and s_c is the error in the concentration c. For the propagation factor for the matrix composition, only the second term in these formulas has to be used because the first terms reflect errors in the stopping power and the X-ray attenuation coefficient only. The second term in Eq. C.13 will be called $s_{S_t,c}$ and in Eq. C.14 $s_{\mu_t,c}$. The error in the yield can be calculated using equations 3.9, 3.10, C.13 and C.14 and either summing the two terms for the stopping power and the X-ray attenuation coefficient quadratically or linearly. Quadratic summation is as follows:

$$\frac{s_{Y,c}}{Y(X_Z)} = \sqrt{\left\{ \left(\frac{\frac{s_{Y,S_t}}{Y(X_Z)}}{\frac{s_{S_t}}{S_t}} \frac{s_{S_t,c}}{S_t} \right)^2 + \left(\frac{\frac{s_{Y,\mu_t}}{Y(X_Z)}}{\frac{s_{\mu_t}}{\mu_t}} \frac{s_{\mu_t,c}}{\mu_t} \right)^2 \right\}} \tag{C.15}$$

The linear summation is analogous to the quadratic summation and could be used as an alternative in equations C.13, C.14 and C.15, but it can only be used for maximum deviations not for standard deviations. For both types of summation, there exists a problem for Eq. C.13: the stopping power depends on the proton energy. This implies that s_{S_t}/S_t depends on the proton energy even if s_{S_i}/S_i and s_c do not. Another problem is the fact that the two contributions to the error in the yield (Eq. C.15) are not independent because (1) the propagation factors for S and μ are interdependent according to Eq. 3.12 and (2) both terms in Eq. C.15 contain the error s_c. Therefore quadratic summation cannot be used. The linear summation gives similar results as the method of calculating the change in the yield as a function of the change in the matrix composition with Eq. 3.4. In view of these facts, we will use this last method.

Finally, we derive equations 3.13 and 3.14, giving the relation between the propagation factor to the yield and to the calculated concentration due to the uncertainty in the matrix composition. A binary matrix A_cB_{1-c} is used. The parameter c fixes the matrix composition, it must be distinguished from the calculated concentration c_Z. The yield can then be written as

$$Y(X_Z) = c_Z \text{fc.}\,(c), \tag{C.16}$$

with fc. (c) a function of the matrix composition c. Z can be element A or B. This equation can be used to calculate the propagation factor to the yield using Eq. 3.4 for both elements.

$$\begin{aligned} P'(Y(X_A),c) &= \frac{(c+\delta)\text{fc.}\,(c+\delta) - (c-\delta)\text{fc.}\,(c-\delta)}{c\text{fc.}\,(c)2\delta} \\ &= \frac{\text{fc.}\,(c+\delta) - \text{fc.}\,(c-\delta)}{\text{fc.}\,(c)2\delta} + \frac{\text{fc.}\,(c+\delta) + \text{fc.}\,(c-\delta)}{2c\,\text{fc.}\,(c)} \\ P'(Y(X_B),c) &= \frac{(1-c-\delta)\text{fc.}\,(c+\delta) - (1-c+\delta)\text{fc.}\,(c-\delta)}{(1-c)\text{fc.}\,(c)2\delta} \end{aligned} \tag{C.17}$$

$$= \frac{\text{fc.}\,(c+\delta) - \text{fc.}\,(c-\delta)}{\text{fc.}\,(c)2\delta} - \frac{\text{fc.}\,(c+\delta) + \text{fc.}\,(c-\delta)}{2(1-c)\text{fc.}\,(c)} \qquad \text{(C.18)}$$

Next, the propagation factor to the concentration has to be calculated:

$$\begin{aligned} P'(c_Z, c) &= s_{c_Z}/(c_Z s_c) = \frac{\partial c_Z}{\partial c}/c_Z \\ &= -\frac{\partial \text{fc.}\,(c)}{\partial c}/\text{fc.}\,(c) \equiv -P'(\text{fc.}\,(c), c) \end{aligned} \qquad \text{(C.19)}$$

The first term in eqs. C.17 and C.18 is equal to $P'(\text{fc.}\,(c), c)$ according to Eq. 3.4 and the second term is approximately equal to $1/c$ and $1/(1-c)$ respectively. Substituting these results gives eqs. 3.13 and 3.14.

Table of Symbols

A	area perpendicular to the beam direction (cm^2),
A_B	total beam area (cm^2),
A_S	total sample area perpendicular to the beam direction (cm^2),
A_T	intersection of A_S and A_B (cm^2),
$b_{Z,X(K)}$	branching ratio, which is the fraction of the total K-shell X-rays in the line $X_Z(K)$,
c_j	mass fraction of element j in the target (g/g),
$c_Z(A,x)$	mass fraction of element Z in the volume $dAdx$ (g/g),
$E_{P,0}$	initial particle beam energy (keV),
$E_{P,f}$	particle beam energy on leaving the target or 0 (keV),
E_{X_Z}	energy of an X-ray in line X_Z (keV),
$f_A(E_{X_A}, E_{X_B})$	parameter described by Eq. 2.40 (cm^{-1}),
L	depth in the target, parallel to the beam direction, where the secondary X-rays are produced in the SF process (cm),
m'_Z	mass per unit length of element Z in area A_T of the target (g/cm),
m_Z	total mass of element Z in area A_T in the target (g),
M_Z	atomic mass of element Z (g/mol),
N_{Av}	Avogadro constant (mol^{-1}),
$n_P(A,x)$	the number of bombarding particles per unit area (cm^{-2}),
N_P	number of bombarding particles incident on the target,
$n_Z(A,x)$	number of atoms of element Z per unit volume (cm^{-3}),
$\frac{dN_B(E_P)}{dE_P}$	total number of X-rays with energy E_{X_B} produced at proton energy E_P thus at depth x in the target (see Eq. 2.41),

$P(fc.(x), x)$	error propagation factor for the uncertainty in parameter x to the uncertainty in a function of x,
p	$\frac{\mu_t(E_{X_A})}{\rho_S} \frac{\rho_S}{\cos\theta}$,
q	$\frac{\mu_t(E_{X_B})}{\rho_S} \rho_S$,
$r_{A,K}$	absorption edge ratio for the K-shell of element A (see Eq. 2.30),
$R(SF/P)$	ratio of all X-rays produced by SF to the X-rays produced by primary production,
$S_j(E_P)$	stopping power for element j in the target (keV cm^2 /g),
$S_t(E_P, A)$	total stopping power for the target (keV cm^2/g),
t	total target thickness, parallel to the target normal (cm),
$T_{abs}(E_{X_Z})$	transmission probability of X-rays with energy E_{X_Z} through an absorber,
$T_S(E_{X_Z}, A, x)$	transmission probability of X-rays with energy E_{X_Z} through the sample from depth x in the direction of the detector,
$T_{0 \leq L \leq x}(x)$	transmissions of X_B X-rays from layer $(x, x+dx)$ at angle β to layer $(L, L+dL)$ and the transmission of X_A X-rays from layer $(L, L+dL)$ to the detector at an angle θ integrated over all depths L, lying between the sample surface and the depth x, and integrated over all angles β (see Eq. 2.42),
$T_{x \leq L \leq t}(x)$	transmissions of X_B X-rays from layer $(x, x+dx)$ at angle β to layer $(L, L+dL)$ and the transmission of X_A X-rays from layer $(L, L+dL)$ to the detector at an angle θ integrated over all depths L, lying between the depth x and the back side t of the target, and integrated over all angles β (see Eq. 2.43),
x	depth in the target, parallel to the beam direction (cm),
X_Z	X-ray line of element Z, e. g. $K_{\alpha 1}$ or $L_{\beta 3}$,
$Y(X_Z, A, x)$	number of detected X-rays in line X_Z,
$Y_P(X_Z)$	number of detected primary X-rays in line X_Z (produced by protons),
$Y_{SF}(X_A, X_B)$	number of detected X-rays in line X_A produced by X-rays in line X_B,

α	angle between particle beam and target normal,
β	angle of the direction of the primary X-rays in the SF process,
$\varepsilon(E_{X_Z})$	detector efficiency, this is the probability, that the energy of an X-ray is completely absorbed in the detector crystal,
$\varepsilon_{abs}(E_{X_Z})$	$= T_{abs}(E_{X_Z})\varepsilon(E_{X_Z})\frac{\Omega}{4\pi}$,
$\frac{\mu_j(E_{X_Z})}{\rho_j}$	mass absorption coefficient of element j in the target (cm^2/g),
$\mu_t(E_{X_Z}, A)$	total linear X-ray absorption coefficient of the target (cm^{-1}),
$\omega_{Z,K}$	fluorescence yield for the K-shell, this is the probability of a vacancy being filled by an electron from a higher shell under emission of an X-ray,
$\Omega/4\pi$	relative detector solid angle,
$\rho_S(A, x)$	total density of the sample (g/cm^3),
$\sigma_{Z,X}^{prod}(E_P(x))$	cross section for the production of an X-ray (cm^2),
$\sigma_{Z,K}^{ion}(E_P)$	cross section for ionization of the K-shell of element Z (cm^2),
σ_{coh}	coherent absorption coefficient, which describes the coherent or Rayleigh scattering of an X-ray on an atomic electron. During this process their is no energy loss for the X-ray,
σ_{incoh}	incoherent absorption coefficient, which describes the incoherent or Compton scattering of an X-ray on an electron. During this scattering there is an energy loss for the X-ray,
θ	angle between the target normal and the direction of the detector,
τ_{tot}	photo electric absorption coefficient, which describes the interaction whereby the energy of an X-ray is completely absorbed under ejection of an electron from its shell, thus creating a vacancy,
$\tau_{A,K}(E_{X,B})$	photo-electric absorption coefficient for ionization of the K-shell of element A by an X_B X-ray (cm^{-1}),
χ_R^2	reduced Chi-squared $= \frac{1}{N-1}\sum_{i=1}^{N}\left\{(c_{\rm meas} - c_{\rm ref})^2/s_{\rm tot}^2\right\}$.

Summary

In this thesis, the absolute calibration method for thick-target PIXE is evaluated. In PIXE, characteristic X-rays are released by a target under bombardment of accelerated particles, typically protons of a few MeV, and are detected with an X-ray detector. The energy of the X-rays is characteristic for the atom where they were produced and the elemental concentration can be calculated from the number of X-rays. In the absolute calibration method, this calculation is done from first principles using a data base of values for all quantities needed. This method is very flexible and versatile since it does not rely on any standards.

For thick targets, two so-called thick target effects have to be considered: (1) The particles lose energy in the target; they can be completely stopped. (2) Part of the characteristic X-rays can be absorbed in the target before reaching the detector. A secondary process, called Secondary Fluorescence (SF), can occur under specific conditions, viz. when particle-induced X-rays in their turn produce characteristic X-rays of lower Z elements in the target. The theoretical description of both the primary production and the SF production of X-rays is treated in Chapter 2. The underlying conditions and assumptions are given and special attention is paid to the physical interpretation of the equations. A selection from the currently available data for the values of the quantities in the equations has been made and the accuracy of the data is evaluated.

Reliable error estimates for the calculated concentrations have to be obtained to evaluate the absolute calibration method. In Chapter 3, a method of error calculation is described, introducing the error propagation factor. Whereas the error calculation for most quantities is straightforward, there are several quantities for which the error calculation is more complicated. These quantities are the stopping power, the X-ray attenuation coefficient, the proton beam energy, and the matrix composition. It is found that the error propagation factors of the stopping power and the X-ray attenuation coefficient for thick targets are interdependent.

The calculation of the concentration and of its associated uncertainty is implemented in a computer program. Before experimental verification was possible, the PIXE setup had to be modified. The new setup is described in Chapter 4. To allow the measurement of thick targets, several systems have been added to the experimental setup: a rotating vane for the charge measurement during the analysis of thick targets, a new Faraday cup for the charge measurement during the analysis of thin targets and for the calibration of the rotating vane, a Beam-On-Demand system to reduce pile-up and eliminate the need for dead-time correction, and an electron gun to eliminate charge build-up on thick isolating targets. In addition, the values of several experimental quantities needed for the absolute calibration are determined in this chapter, together with their uncertainties. These include the thickness of the absorbers, the detector solid angle, the detector efficiency, and

the proton beam energy.

In Chapter 5, the method of absolute calibration is checked experimentally using a number of standard materials, including a set of metal foils, used single to check the primary yield and used in pairs to check the SF yield, two alloys, and four biological reference materials. The check was limited to K-lines from elements ranging from Na to Sn. The detector has turned out to be a potential source of errors. Particularly, it was found that the solid angle is a function of X-ray energy. Presumably, this is caused by the fact that the dead layer thickness increases at the edges of the crystal, which absorbs the low-energy X-rays before they can enter the active part. Several methods for the calibration of the detector efficiency are discussed.

At present, the calculated total uncertainty is about 8-20% under favourable conditions, possibly lower because several error sources are assumed to be independent that are in fact dependent. Also, individual uncertainties of quantities used for the calculation may be overestimated, e.g. the transmission of low-energy X-rays through a Be absorber and the detector efficiency for high-energy X-rays. On the other hand, under unfavourable conditions, e.g. for complex spectra, the calculated uncertainty may increase substantially and, still, it may be an underestimation. Major contributions to the uncertainty in the concentration are the uncertainties in the X-ray attenuation coefficient, in the X-ray yield, in the detector efficiency including the solid angle, and in the matrix composition. No deviations from the physical model are found within the uncertainties, although there are indications that the SF yield is overcalculated for K-lines of heavier elements ($Z > 40$).

The evaluation of the accuracy has shown that the absolute calibration can be used in practice as a calibration method in TT-PIXE. At present, the calculated uncertainty may be quite large, but it can be reduced by determining the quantities with largest uncertainty more accurately and by removing the sources of overestimation. Sofar, for simple targets, especially thin targets, when matching standards are available, the accuracy for the calibration with standards is better than for absolute calibration. However, the availability of accurately determined standards is often a problem. Absolute calibration is a flexible method for the analysis of different elements in different matrices. In case of inhomogeneous targets and use of a microbeam, the use of the absolute calibration method is virtually inescapable. For this purpose, we have derived a formula for which the composition of a sample may be variable in two surface dimensions.

It should be stressed that, as the accuracy of the physical quantities improves, the determination of the matrix composition of the target becomes relatively more important. The determination can be refined by an iterative approach for the elements with $Z > 10$, e.g. as applied for the alloys in Section 5.5. Lighter elements can be measured with NBS simultaneously with PIXE, as performed in Section 5.7.

Samenvatting

PIXE (Particle Induced X-ray Emission) is een analytische techniek, die al meer dan twintig jaar gebruikt wordt. De karakteristieke röntgenstraling, die een preparaat onder een bombardement van versnelde protonen (met een energie van enkele MeV) uitzendt, wordt met een röntgendetector gemeten. De energie van de röntgenstraling is karakteristiek voor het atoom en uit het aantal gemeten röntgenquanta kan de concentratie van dat element in het preparaat berekend worden. Voor de analyse van dikke preparaten moeten twee extra effecten meegenomen worden: (1) de versnelde protonen verliezen energie in het preparaat; ze kunnen zelfs geheel afgeremd worden, (2) een deel van de geproduceerde röntgenquanta kan in het preparaat geabsorbeerd worden voordat ze de detector kunnen bereiken. In bepaalde gevallen kan een secundair effect optreden, namelijk Secondaire Fluorescentie (SF). In dit geval kunnen geabsorbeerde primaire röntgenquanta op hun beurt weer karakteristieke röntgenstraling produceren.

In dit proefschrift wordt de theorie van de primaire productie en de SF productie van röntgenstraling behandeld. De onderliggende aannamen worden gegeven en getracht wordt een inzicht te geven in de fysische interpretatie van de formules. Onderzocht is in hoeverre een kwantitatieve analyse van preparaten gedaan kan worden, die alleen berust op de berekening van de 'thick-target' effecten, dus zonder gebruik te maken van standaard preparaten. Deze methode hebben wij absolute calibratie genoemd en hiervoor zijn waardes voor alle in de formules voorkomende grootheden nodig. Er is een selectie gemaakt uit de op dit moment beschikbare gegevens en de nauwkeurigheid van deze gegevens is geanalyseerd. Tevens is er een foutenberekening opgezet om te kunnen bepalen hoe onzekerheden in deze gegevens in het eindresultaat doorwerken. De invloed van de onzekerheden van een aantal grootheden, namenlijk de 'stopping power', de röntgen attenuatie coëfficiënt, the protonbundel energie en de matrix samenstelling van het preparaat, op de onzekerheid in de berekende concentratie is nader bediscussieerd. Voor alle overige grootheden is de foutendoorwerking niet gecompliceerd.

Al deze berekeningen zijn toegepast in een programma om uit gemeten röntgen intensiteiten de concentratie van een element te kunnen berekenen tezamen met de bijbehorende fout. Alvorens de analyse toegepast is, is eerst de al bestaande PIXE opstelling gemodificeerd. Er zijn een aantal systemen toegevoegd om de meting van dikke preparaten mogelijk te maken: zoals een electronenkanon voor de bestrijding van ladingsopbouw op dikke isolerende preparaten, een verbeterde Faraday cup voor de ladingsmeting bij dunne preparaten, een 'Rotating Vane' voor de ladingsmeting bij dikke preparaten en een 'Beam On Demand' systeem voor het reduceren van 'Pile-Up' en het elimineren van dode tijd correcties. Tevens zijn een aantal experimentele grootheden en de bijbehorende fouten bepaald, zoals de

protonbundel energie alsook de ruimtehoek en de efficiëntie van de röntgendetector.

De ontwikkelde methode van absolute calibrate is in hoofdstuk 5 getest aan de hand van metingen van een aantal standaard preparaten, zoals een serie metaal folies, enkelvoudig gemeten om de primaire productie te controleren en in paren om de SF productie te controleren, twee legeringen en vier biologische referentie materialen. De controle was beperkt tot K-lijnen van elementen van Na tot Sn. De detector bleek een potentiele bron van fouten omdat het een zeer gecompliceerd systeem is. Metingen hebben uitgewezen dat de ruimtehoek van de detector afhankelijk is van de röntgenenergie, omdat het detectorkristal een dode laag bevat waarvan de dikte groter is aan de randen van het kristal. Deze dode laag absorbeert laag energetische röntgenquanta waardoor het effectieve detector oppervlak kleiner lijkt.

De berekende onzekerheid varieert van 8% tot 20% onder optimale omstandigheden. Op grond van de metingen kan aangenomen worden dat deze onzekerheid te groot is, in specifieke gevallen kan dit verschil zelfs oplopen tot een factor twee. Een mogelijke oorzaak hiervoor is dat de onzekerheden in de gebruikte grootheden te groot zijn ingeschat. Voorbeelden hiervan zijn de transmissie van laag energetische röntgenquanta door de Be absorber en de detector efficiëntie voor hoog energetische röntgenquanta. De totale onzekerheid kan verder worden verkleind door de accuratesse waarmee de gebruikte grootheden in de formules bekend zijn te verbeteren. Op het moment hebben de röntgenpiek oppervalkte, de röntgen absorptie coëfficiënt, de matrix samenstelling en de detector efficiëntie de grootste onzekerheid. Binnen de huidige nauwkeurigheid zijn er geen afwijkingen gevonden van het gebruikte fysische model, alhoewel er indicaties zijn dat de berekening van de SF opbrengst voor K-lijnen van zware elementen ($Z > 40$) een te grootte waarde oplevert.

De evalutie van de metingen heeft aangetoond, dat de absolute calibratie in de praktijk gebruikt kan worden als calibratie methode voor TT-PIXE. Op het ogenblik is de nauwkeurigheid van de calibratie met standaards nog beter dan die van de absolute calibratie indien het simpele preparaten betreft, bij voorkeur dunne, voorvoor een goed gelijkende standaard bestaat. Het verkrijgen van goed gecalibreerde standaarden is echter vaak een probleem. Absolute calibratie is daarentegen een veelzijdige en flexibele methode, waarvan het gebruik praktisch onontkombaar is voor de analyse van inhomogene preparaten met een microbundel.

Naarmate de nauwkeurigheid van de fysische grootheden beter wordt, wordt de bepaling van de matrix samenstelling relatief belangrijker. Deze bepaling kan worden verfijnd door een iteratieve procedure voor de bepaling van de concentraties van de elementen met $Z > 10$, zoals is gedaan voor de legeringen in sectie 5.5. De lichtere matrix elementen kunnen gelijktijdig met PIXE gemeten worden met de analyse techniek NBS, zoals is gebeurt voor de biologische materialen in sectie 5.7.

Dankwoord

Hierbij wil ik van de gelegenheid gebruik maken om alle personen te bedanken, die mij hebben geholpen tijdens de voorbereiding van dit proefschrift. Veelal moesten de experimenten 's avonds of zaterdags gebeuren en mijn erkentelijkheid gaat uit naar hen die steeds bereid waren om buiten kantooruren in het cyclotrongebouw aanwezig te zijn. Een aantal mensen verdient het om met name genoemd te worden: Peter Mutsaers voor zijn hulp bij het opbouwen van de PIXE opstelling en de uitgebreide discussies; Leo de Folter voor zijn niet aflatende technische ondersteuning; Ad Kemper voor zijn bijdrage aan het "Beam-on-Demand" systeem, waarvan hij het electronische deel ontwikkeld heeft; Wim Verseijden voor zijn hulp bij het oplossen van alle problemen die ontstaan bij het gebruik van computers; de cyclotronbedrijfsgroep voor het operationeel houden van het cyclotron en hun hulp bij het verhelpen van storingen, ook als die in hun vrije tijd vielen; voorts de studenten Bram Kruseman, Wilko Verbakel, Guido Coenders, Martin Creusen, Patrick Tinnemans, Yves Wintraecken, Stefan van den Berg, Els Koffeman en Peter Krutzen, voor hun hulp bij de opbouw van de PIXE opstelling en bij het produceren van de eerste betrouwbare metingen. En tenslotte, alle collega's voor de collegiale en gezellige sfeer in het cyclotrongebouw.

Levensloop

23 sep 1961	Geboren te Groningen
mei 1980	Eindexamen Atheneum B
	Scholengemeenschap Adelbert College, Wassenaar
sep 1980 - aug 1986	Studie Natuurkunde,
	Rijksuniversiteit Leiden
mrt 1987 - juni 1988	Vervulling dienstplicht
mrt 1989 - dec 1993	Promotie onderzoek als a.i.o.
	in de vakgroep Deeltjesfysica,
	Faculteit Technische Natuurkunde, TUE

Stellingen

behorende bij het proefschrift

Accuracy Evaluation of Absolute Calibration in Thick-Target PIXE

door Frans Munnik

Eindhoven, 28 juni 1994

-I-

Foutenberekening wordt nog teveel als een puur mathematische excercitie gezien en nog te weinig als methode voor het verkrijgen van fysisch inzicht in het relatieve belang van de, voor het eindresultaat benodigde, grootheden.

- Dit proefschrift, hoofdstuk 3.

-II-

De praktische controle van grensverleggend analytisch onderzoek gelijkt op het kip-en-ei probleem: Zonder geavanceerde gecertificeerde referentiematerialen kan een verbetering in een analytische techniek niet bewezen worden. Aan de andere kant vergen geavanceerde referentiematerialen het bestaan van een analytische techniek, waarmee de referentiematerialen gecertificeerd kunnen worden.

- Dit proefschrift, hoofdstuk 5.

-III-

De methode om de energie van een H_2^+ bundel te bepalen via de detectie van zowel H_2^+ als alfa deeltjes met gebruikmaking van dezelfde detectorcalibratie, zoals toegepast door Scott en Paine, is niet correct.

- D.M. Scott and B.M. Paine, *Nucl. Instr. and Meth.* **218** (1983) 154.

-IV-

De door Aloupogiannis en medewerkers voorgestelde methode om de gemiddelde röntgen produktie werkzame doorsnede voor middelmatig dikke preparaten te benaderen door het middelen van de waarden van de werkzame doorsnede aan de voor- en achterkant van het preparaat met een wegingsfactor 2 voor de waarde van de voorkant, is in de meeste gevallen onjuist.

- P. Aloupogiannis, G. Robaye, I. Roelandts and G. Weber, *Nucl. Instr. and Meth.* **B22** (1987) 72.

-V-

Het gebruik van een referentie uit een artikel zonder het originele artikel op te zoeken heeft een aantal risico's tot gevolg. (i) Een ontwikkeling kan aan een verkeerde auteur worden toegeschreven. (ii) Het kan lijken dat er meer onafhankelijke methoden zijn om een doel te bereiken. (iii) Randvoorwaarden voor het gebruik van een methode kunnen niet meer vermeld worden.

-VI-

Terwijl veel mensen dagelijks televisiejournaals volgen voor het op peil houden van hun algemene kennis over de toestand in de wereld, zou die kennis meer gebaat zijn bij het wekelijks lezen van een nationaal of internationaal tijdschrift.

-VII-

Nog te weinig wordt onderkend, dat het vormen van een touwgroep voor het begaan van een steile helling met sneeuw of ijs slechts schijnveiligheid biedt, terwijl het de objectieve veiligheid ondermijnt.

-VIII-

De meeste ontwerpers van fietspaden rekenen teveel met een kruissnelheid van 15 km per uur en onvoldoende met racefietsers en brommers, die ook van deze paden gebruik moeten maken.

-IX-

Als de huidige trend in bezuinigen bij de universiteiten zich voortzet, zijn er in de toekomst geen gesalarieerde wetenschappelijke onderzoekers meer, doch slechts onderzoekers, die gratis van de onderzoeksfaciliteiten gebruik mogen maken, eventueel met behoud van uitkering of wachtgeld.

-X-

Als aangenomen wordt, dat computerspelletjes een belangrijke rol spelen bij de ontspanning van een promovendus, is het aan te raden om tot aanschaf van joysticks over te gaan; dit om slijtage aan essentiëlere onderdelen van de computer (toetsenbord, muis) te voorkomen.